EINDHOVEN
UNIVERSITY OF
TECHNOLOGY

Eindhoven University of Technology

MASTER

Spin wave emission from point contact spin torque nano-oscillators

Janssens, X.G.H.

Award date:
2007

Link to publication

Disclaimer
This document contains a student thesis (bachelor's or master's), as authored by a student at Eindhoven University of Technology. Student theses are made available in the TU/e repository upon obtaining the required degree. The grade received is not published on the document as presented in the repository. The required complexity or quality of research of student theses may vary by program, and the required minimum study period may vary in duration.

General rights
Copyright and moral rights for the publications made accessible in the public portal are retained by the authors and/or other copyright owners and it is a condition of accessing publications that users recognise and abide by the legal requirements associated with these rights.

- Users may download and print one copy of any publication from the public portal for the purpose of private study or research.
- You may not further distribute the material or use it for any profit-making activity or commercial gain

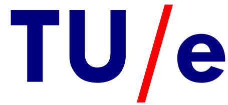

Technische Universiteit
Eindhoven
University of Technology

Spin Wave Emission from Point Contact Spin Torque Nano-Oscillators

X.G.H. Janssens
October 2007

Report of a graduation project carried out at the NEXTNS spintronics group of the Interuniversitary Micro-Electronics Center (IMEC) in Leuven, Belgium, from June 2006 to October 2007.

Promotor : Prof. Dr. Ir. H.J.M. Swagten (TU/e)
Supervisors : Dr. Ir. M. van Kampen (IMEC), Dr. Ir. L. Lagae (IMEC)

Summary

The discovery of the spin torque effect, by which a spin-polarized direct current can induce a stable precession of the free layer of a magnetic spin valve element, has enabled a novel type of oscillator, which can serve as a current-controlled, frequency-agile microwave source with applications in integrated electronics and telecommunications devices. However, the power output obtained from current state-of-the-art spin torque oscillators is typically too low to enable successful integration with current electronics. On the other hand, mode locking of multiple oscillators could enable an increase in emitted power. Spin wave emission has been identified as a possible coupling mechanism for the frequency and phase locking of multiple point contact spin torque nano-oscillators in a common magnetic layer. This work discusses the fabrication and characterization of customized oscillator devices that feature optical access to the extended magnetic layer of a point contact oscillator device. This enables the study of spin wave emission using the optical Brillouin light scattering technique, of which the first results are presented. During the electrical characterization of the low resistive point contact devices, unexpected scaling of the four-probe point contact resistance and magnetoresistance values with point contact size was observed. This behavior is explained by a model that incorporates both current-in-plane and current-perpendicular-to-plane contributions to the magnetoresistance, based on the observations made in finite element modeling of the device, which revealed the presence of a parasitic series resistance due to current spreading effects in the device electrodes. Furthermore, the point contact devices were observed to generate low frequency microwave oscillations upon the application of a direct current. These low frequency phenomena are assumed to be caused by the movement of a magnetic vortex core around the point contact center. Finally, micro-magnetic simulations of spin wave emission induced by the local excitation of a magnetic thin film illustrate how the interplay between device geometry and the dispersive and anisotropic nature of the spin wave propagation can lead to highly anisotropic power radiation within the film.

Table of Contents

Summary iii

Table of Contents iv

1. Introduction 1

1.1. General Introduction 1

1.2. This Work 5

1.3. Guide to this thesis 8

2. Theory 10

2.1. Magnetoresistance 11
2.1.1. Anisotropic Magnetoresistance 11
2.1.2. Giant Magnetoresistance 12
2.1.3. Tunnel Magnetoresistance 14
2.1.4. Junction Area 15

2.2. Spin Torque 17
2.2.1. Spin Angular Momentum Transfer 18
2.2.1.1. Spin Accumulation 18
2.2.1.2. Spin Transfer 19
2.2.2. Spin Transfer Dynamics 22

2.3. Magnetization Dynamics 23
2.3.1. Landau-Lifshitz-Gilbert-Slonczewski Dynamic Equation 23
2.3.1.1. Precession Torque 24
2.3.1.2. Damping Torque 26
2.3.1.3. Spin-Transfer Torque 27
2.3.1.4. The Effective Field 28

2.4. Spin Wave Theory 30
2.4.1. Spin Waves 30
2.4.2. Spin Wave Propagation 31
2.4.2.1. Magnetostatic Backward Volume Wave 33
2.4.2.2. Magnetostatic Forward Volume Wave 35
2.4.2.3. Magnetostatic Surface Wave 36

3. Experimental Techniques 38

3.1. Sputter Deposition 38
3.1.1. The Sputtering Process 38
3.1.2. The Sputtering System 40

3.2. Microstructure Patterning 41
3.2.1. Lithographic Pattern Definition 41
3.2.2. Pattern Transfer 43
3.2.2.1. Lift-Off 43
3.2.2.2. Ion-Milling and Wet Etching 44

3.3. Microstructure Characterization 44

3.3.1. Dektak Surface Profilometry 44
3.3.2. Scanning Electron Microscopy 45
3.3.3. Atomic Force Microscopy 45
3.3.4. Ellipsometry 46

3.4. Measurement Setups 47
3.4.1. Four-Probe Resistance Measurement Setup 47
3.4.2. Magnetoresistance Measurement Setup 49
3.4.3. Microwave Measurement Setup 50
3.4.4. Brillouin Light Scattering Setup 51

4. Device Fabrication 54

4.1. General Process Overview 55

4.2. Detailed Process Workflow 56
4.2.1. Point Contact Definition 58
4.2.2. Electrode Definition 63
4.2.3. Evaluation of the BLS Tip Design 66

4.3. FOX12 Ion-Mill Rate Calibration 68
4.3.1. Standard Calibration Procedure 68
4.3.2. FOX12 Calibration Procedure 69

5. Experimental Results 74

5.1. Point Contact Characterization 75
5.1.1. Size and Morphology 75
5.1.2. Magnetoresistance 79
5.1.2.1. Experimental Observation 79
5.1.2.2. Current Distribution Simulations 81
5.1.2.3. Magnetoresistance Model 88

5.2. Point Contact Microwave Oscillations 95

5.3. Brillouin Light Scattering from Spin Waves 98
5.3.1. Thermally and DC Excited Magnetization Dynamics 99
5.3.2. RF Excited Magnetization Dynamics 100
5.3.3. Spatially Resolved Spin Wave Decay 105

6. Micro-Magnetic Spin Wave Modeling 108

6.1. Introduction 108
6.1.1. OOMMF 109
6.1.2. Local Excitation of a Magnetic Film 110
6.1.3. Spin Wave Propagation 110

6.2. One-Dimensional Simulations 111
6.2.1. Simulation Geometry and Parameters 112
6.2.2. One-Dimensional Thin Film Magnetostatic Modes 114
6.2.3. Spatial Power Decay and Localization Effects 116
6.2.4. Film Thickness 124

6.3. Two-Dimensional Simulations 125

6.4. Conclusions 131

7. Conclusions and Outlook **133**
7.1. Conclusions *133*
7.2. Outlook *135*
8. Acknowledgements **136**
9. References **137**
List of Abbreviations **141**

1. Introduction

1.1. General Introduction

Since the discovery of the electron as the fundamental unit of charge by J. J. Thompson in 1897, its application in a huge variety of electronic devices has revolutionized our world and the way we live. This is especially true since the invention of the transistor in 1947 by William Shockley, John Bardeen and Walter Brattain, which has incubated a multi-billion semiconductor industry, whose products are found in every aspect of our daily lives and with applications in the automotive, domestic, industrial, healthcare and defense environments, to name a few. Another important milestone in the evolution of electronics is the discovery of the quantum mechanical property of electron spin by Ralph Kronig, George Uhlenbeck and Samuel Goudsmit in 1925. Apart from its mass and charge, an electron is now characterized by one of two spin states, i.e. up or down (see Figure 1-1), and an entirely new world of electronic manipulation based on magnetism becomes accessible. Research in the area of electronics which exploits both the electron charge and its spin, called spintronics, is continuing and intensive, due to its potential for conceptually new applications and because of the interesting new physics to be explored.

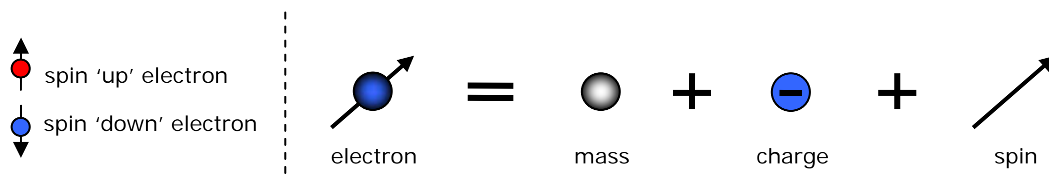

Figure 1-1: (Left) The quantum mechanical spin of an electron is quantized in an ‘up’ and ‘down’ state. (Right) An electron is characterized by its mass, charge and its quantum mechanical spin.

Results of previous state-of-the-art spintronics research have already found their way to numerous applications in the sensor and information storage industry, dominantly through the anisotropic (Thomson [1]), giant (Baibich, Fert [2], Binasch [3], Grünberg [4]) and tunnel (Moodera [5], Juliere [6]) magnetoresistance effects. For example, the giant magnetoresistance effect occurs in a device that consists of two magnetic layers, separated by a third, non-magnetic spacer layer, as indicated in Figure 1-2. A current applied to such a device experiences a low resistance when the layers are magnetized in the same direction, whereas a high resistance results when the magnetizations are oriented anti-parallel to each other. This effect is widely used in data storage solutions, including personal computer hard disk drive read heads, since it can relate the magnetic state of a magnetoresistive element to an electronic voltage.

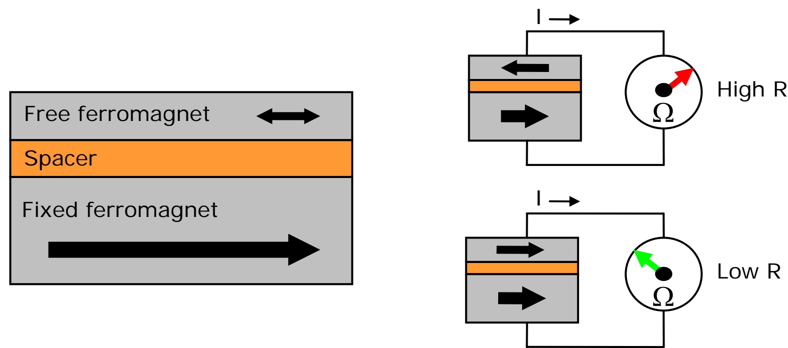

Figure 1-2: The giant magnetoresistance (GMR) effect for a device consisting of two magnetic layers separated by a non-magnetic spacer layer. A current applied to this device experiences a low resistance when the layers are magnetized in the same direction, whereas a high resistance results when the magnetizations are oriented anti-parallel to each other.

The research in spintronics accelerated even more in response to the theoretical predictions of Slonczewski [7] and Berger [8] in 1996 that the electron spin can interact directly with the magnetization of a magnetic element through the spin transfer torque effect. This effect allows a spin-polarized current to exchange spin angular momentum with a magnetic element. Not very long after its theoretical prediction, the spin torque effect was experimentally confirmed through the advancement of nano-scale lithography and fabrication equipment, which allows for the definition and fabrication of very small cross-sectional area devices. This enables the strong confinement of current and associated high current densities required to observe the spin transfer torque effect with the application of a limited bias current.

In accordance with theoretical predictions, a spin torque device can experience both current-induced switching [9][10][11][12][13] and steady-state precession of its free magnetic layer [14][15]. The current-induced switching behavior triggered huge interest from data storage manufacturers, who are directing efforts to the research of current-switched magnetoresistive random access memory (MRAM) as a more efficient and power conscious storage technology compared to current field-switched MRAM prototypes, making current-switched MRAM a viable non-volatile alternative to DRAM and FLASH memory technologies. The interest for this new technology is obviously fed by the ever increasing consumer demand on storage capacity, due to higher resolution rich media content and the increasing need for media archiving and data preservation. For example, various marketing reports indicate that digital storage capacity is expected to experience an eightfold increase by 2012 with an associated doubling of storage industry revenues over the next five years. The spin torque effect allows for a simplification of the present generation of MRAM technology that relies on field switching of magnetoresistive bit elements, rather than on direct spin transfer

torque current-induced switching. Not only does direct switching require less power, spin injection has also been shown to reduce read and write times of the magnetic elements, up to the nanosecond regime. Therefore, whereas the current non-volatile FLASH technology mainly suffers from slow write speeds, MRAM read and write speeds are able to match or even exceed those of DRAM, while further reduction is possible through spin injection. At this moment, an average MRAM bit is still approximately double the size of a DRAM element and no large density modules are commercially available yet. A drawback related to the relatively large element size is that large currents have to be provided by the control transistors to enable spin transfer induced switching. Therefore, the control transistors remain large, until magnetic element sizes shrink further. Note that this implies a power consumption decrease that is inherent to the downscaling process (the spin injection current is proportional to the element sizes). Therefore, current-switched MRAM memory becomes more power efficient for devices below the 65 nm node limit. An additional note to the power decrease is that, unlike DRAM, MRAM does not require a periodic refresh of the memory, decreasing its power consumption even further. Apart from its ability to retain data, even when power is lost, MRAM thus brings with it the promise of decreased power consumption, while offering all of the benefits of other present memory technologies, such as fast read and write speeds. The added benefit of increased data and cycle lifetime (MRAM does not have an effective lifetime, unlike FLASH memory, which degrades over time), makes MRAM a feasible candidate for future non-volatile memory and processor cache.

Apart from current-induced switching, spin torque devices can sustain a steady-state precession of their free magnetic layer which can be translated into an oscillating electrical signal by means of the GMR or TMR effect, with a frequency in the GHz range which depends on both drive current and external field conditions (see Figure 1-3). The spin torque effect thus allows for the design of current-controlled, frequency-agile microwave oscillators, which may find their application in mobile wireless communications, as well as in novel logic and signal processing applications. The frequency-agility and high Q factors that are theoretically obtainable with spin torque nano-oscillators are great assets in the convergence of multi-band wireless technologies on a single chip and offer greater flexibility with respect to the increasing bandwidth scarceness expressed by the increasingly dense bandwidth allocation grids for which licensing competition is fierce. In addition, compared to competing oscillator designs, such as those based on the stable, but low frequency oscillations of a quartz crystal, spin torque oscillators are extremely small, feature reduced cost of manufacturing and can easily be integrated with standard CMOS backend processing. However, a major drawback of the current state-of-the art spin torque nano-oscillators is their marginal power output in RF applications, which ranges from the pW to the nW region. Several solutions to this problem have been

proposed, one of which is the topic of this thesis, and will further be discussed in Section 1.2.

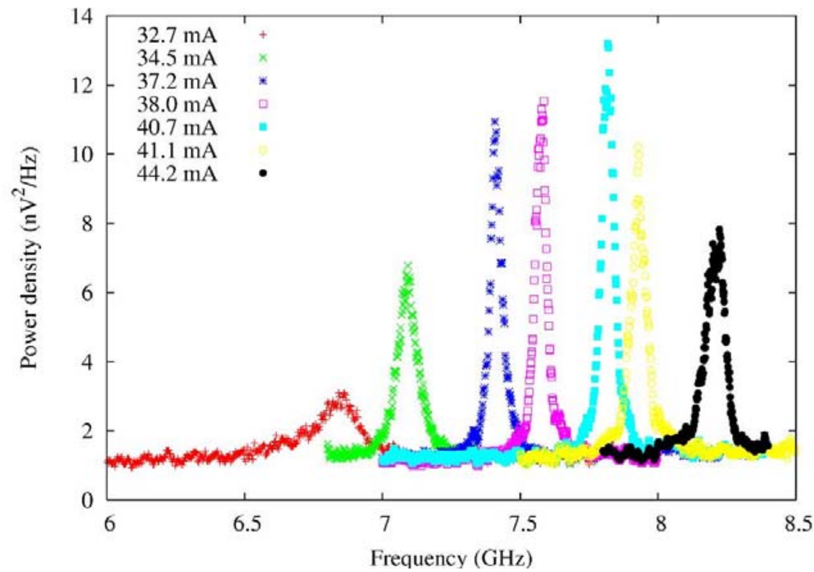

Figure 1-3: The RF emission frequency of a spin torque oscillator can be tuned by varying the bias current supplied to the device. Measurement performed by Q. Mistral (IEF, France).

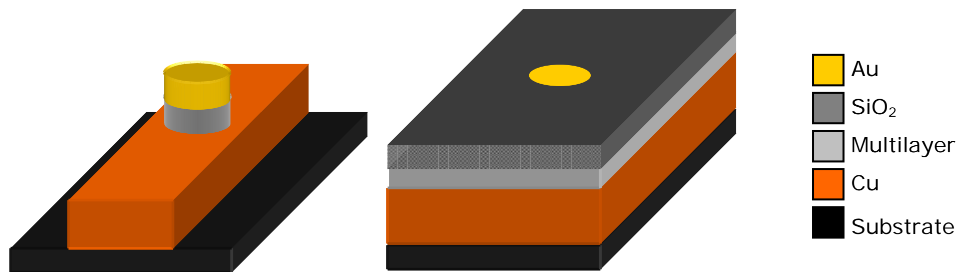

Figure 1-4: (Left) Pillar device geometry. The magnetic multilayer (light gray) is patterned into a small pillar which is contacted by a bottom Cu (orange) and top Au electrode (yellow). (Right) Point contact geometry. Electrical contact with the magnetic multilayer is established through a tiny hole in an insulating material such as SiO_2 (dark gray).

As stated earlier, high current densities are required to provide sufficient transfer of spin angular momentum for the spin-polarized current to be able to interact with a macroscopic magnetic moment. In order to obtain these high current densities (which are of the order of 10^6 to 10^7 A/cm^2) for reasonable bias currents (in the mA range), the current has to be confined to a very small region. Moreover, strong current confinement also aids in the suppression of the Oersted field associated with the drive current, which competes with the spin torque effect due to added damping. Therefore,

spin torque experiments are generally carried out on two distinct types of device geometry, characterized by the way current confinement is achieved. Both geometries are illustrated schematically in Figure 1-4. In the *pillar* geometry, the total magnetic stack is patterned in the form of a nanometer scale pillar, featuring a sufficiently small diameter to furnish the current density necessary for inducing spin torque related phenomena. In the *point contact* geometry, a nanometer scale hole is etched into an insulating layer (e.g. SiO_2), which enables electrical contact to the magnetic layer from on top. Through this hole, the current is also effectively confined to a very small region in the magnetic material under the point contact.

Although quite some experimental data is available for nano-pillar devices, comparatively few research groups and publications have actively focused on point contact geometry spin torque devices, for several reasons. Besides the fact that the nano-pillar geometry features increased compatibility with the technology advancement towards the use of magnetic tunnel junctions instead of spin valves, nano-pillars with sufficiently small diameters can often be described in the macro-spin limit (considering the free layer as a uniform magnetic moment), which enables relatively straightforward magnetization dynamics simulations to be performed for these devices. The point contact geometry, however, is intrinsically more complicated for a number of reasons. First of all, the current confinement in point contacts can take complex forms due to intricate current distribution and spreading effects in the magnetic and conducting layers. Furthermore, the magnetization dynamics in general can no longer be described by simple macro-spin simulations. For example, the magnetization dynamics may become extremely complicated by the possible presence of domain walls in and around the point contact area and by the emission of spin waves in the extended layer. On the other hand, it must be stated that many exciting research opportunities arise in the field of point contact spin torque oscillators, exactly because of these phenomena, which are the topic of this research report.

1.2. This Work

This research considers spin torque nano-oscillators in the point contact geometry. As stated earlier, current state-of-the-art oscillator designs suffer from low RF power emission, which impedes their integration in modern micro-electronic devices. Therefore, two main approaches have been proposed to increase the nano-oscillator power output. The first is the engineering of the magnetic multilayer to obtain higher magnetoresistance changes due to the spin torque action on the free magnetic layer. Therefore, the use of a magnetic tunnel junction instead of the current spin valve giant magnetoresistance device geometry is a feasible approach to increase emitted power. On the other hand, it has been proposed that a power increase could also be obtained by arranging a set of oscillators in such a way that they can magnetically or

electrically synchronize. When the oscillators can be made to both frequency and phase lock, a set of N oscillators has been predicted to generate an output power increase of N^2 [16]. The latter approach will be considered in this thesis, which tries to provide an understanding of the coupling mechanism responsible for mode locking of multiple point contact nano-oscillators.

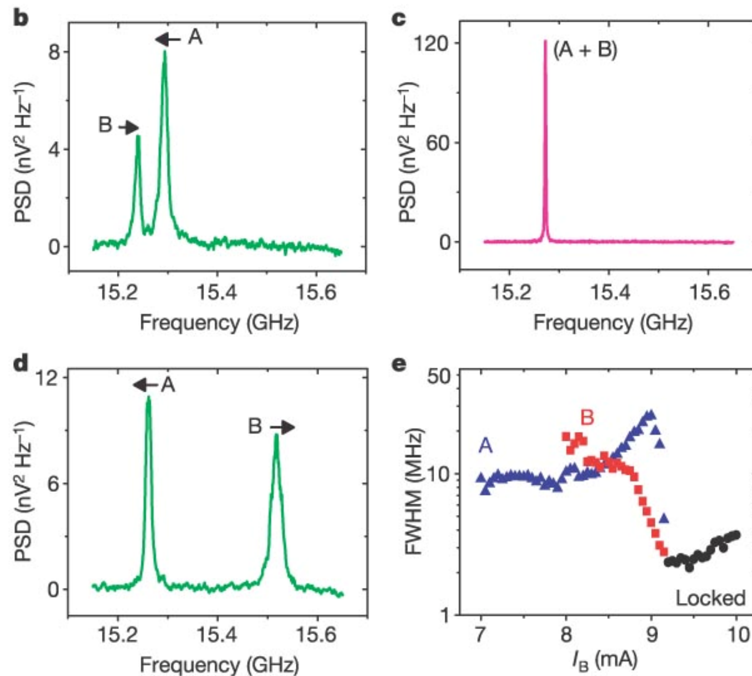

Figure 1-5: Two individual point contact oscillators (A and B) can be made to frequency lock to a common frequency, leading to a substantial increase in emitted power. Panels (b) and (d) show the spectral output from two unsynchronized oscillators. By tuning the bias currents according to (d), the oscillators can be made to lock their frequency (c). The substantial power increase in (c) indicates that the oscillators have also locked their phases. Reprinted by permission from Macmillan Publishers Ltd: Nature, Kaka, S. et al. *Nature* **437**, 389–392 (2005). Copyright 2005.

The interest for the research of the synchronization of nano-oscillators was triggered by a set of recent articles [17][18][19] that discuss the frequency and phase locking of multiple point contact nano-oscillator devices. Specifically, mode locking was observed for two 40 nm diameter point contacts fabricated in a single mesa at a distance of 500 nm apart [18]. Figure 1-5 illustrates how two spin torque oscillators with different frequencies (b) can be made to oscillate in phase when they are tuned to similar frequencies (c, e). The frequency and phase synchronization leads to a considerable increase in output power compared to a single oscillator (note the y-axis scale in c), as is also illustrated in the power maps in Figure 1-6.

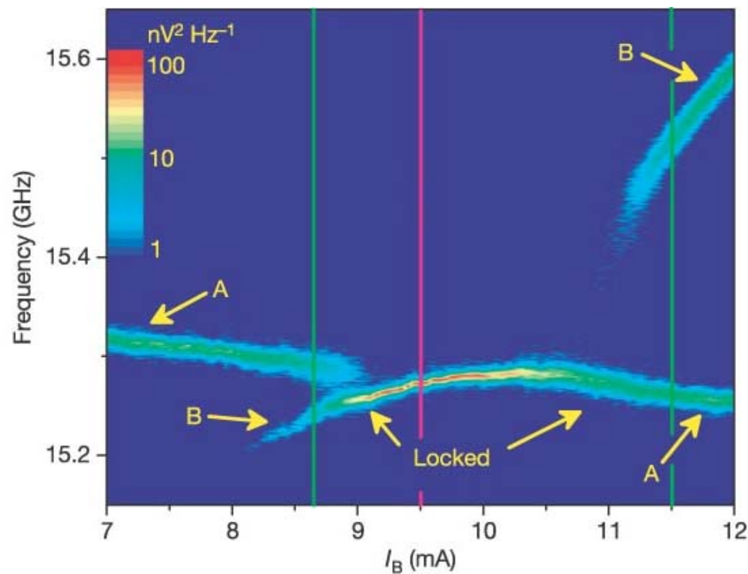

Figure 1-6: Mode locking of two spin torque nano-oscillators (A and B) to a common frequency (around 15.3 GHz), indicated by the substantial increase in emitted power in the locking range. Reprinted by permission from Macmillan Publishers Ltd: Nature, Kaka, S. *et al. Nature* **437**, 389–392 (2005). Copyright 2005.

In the above experiment, the common mesa of the two oscillators was subsequently cut in two by a focused ion beam, after which synchronization between the separate point contacts was no longer possible. This suggests that the coupling between two nano-oscillators may well be due to spin wave emission in the common magnetic layer between multiple oscillators (see Figure 1-7), rather than by magnetic dipole interactions between separate devices. The main goal of this thesis is therefore to design a point contact spin torque nano-oscillator device for which the emission of spin waves into the extended magnetic layer can be investigated.

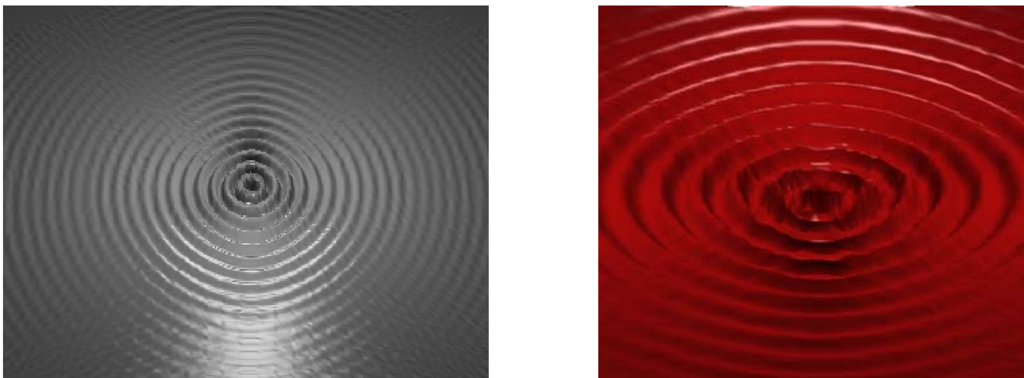

Figure 1-7:Spin wave emission from a nano-scale point contact into the surrounding extended magnetic layer is considered as a possible interaction mechanism for the frequency and phase locking of multiple point contact spin torque nano-oscillators. Images derived from micro-magnetic simulations of Section 6.

1.3. Guide to this thesis

This thesis has aimed to provide a complete and often detailed picture of all aspects involved in attaining its ultimate goal, i.e. the study of spin wave emission in the extended magnetic layer of a point contact nano-oscillator device. As such, this work serves both the experimentalist, who is interested in a detailed description of the process flow that is used to fabricate these point contact devices, and the seasoned physicist, who may be more interested in the physical processes that take place. Therefore, a guide is presented to the reader that points out which sections may be of particular interest in view of the different types of reader.

After the introductory Section 1, Section 2 discusses the physical background of the anisotropic, giant and tunnel magnetoresistance effects in Section 2.1, followed by a qualitative discussion of the spin torque effect based on the understanding of spin accumulation and spin momentum transfer in a magnetic material in Section 2.2. Although the concepts of AMR, GMR and TMR are generally well known to the reader who has some background in magnetism, the concept of spin accumulation and spin torque may be less familiar, which may make Section 2.2 interesting to consider reading. Furthermore, Section 2.3 presents the magnetic dynamic equation of motion with the inclusion of the spin torque effect in the form of a modified Landau-Lifshitz-Gilbert equation with an added Slonczewski spin torque term. The reader who is familiar with the nature of LLG dynamics may consider only reading Sections 2.3.1.3, which considers the modification of the standard LLG equation when spin torque is included and Section 2.3.1.4, which considers the nature of the effective field. Finally, in Section 2.4, the concept of spin waves is introduced and the various magnetostatic modes of propagation in magnetic thin films are discussed. The last section may especially be worth reading, as it provides an insightful introduction to the complex world of spin wave propagation. This will aid the reader in the comprehension of the results of the optical BLS experiments and the spin wave propagation simulations.

Section 3 presents an overview of the various experimental techniques and setups that are used in the fabrication and characterization of spin torque nano-oscillator devices. Sections 3.1 and 3.2 are mainly concerned with the experimental techniques used in the point contact fabrication process that is discussed in Section 4. The reader who is less interested in the specific technical details of the fabrication process can easily skip these sections. However, Sections 3.3 and 3.4 may be interesting for the reader who is unfamiliar with the four-probe magnetoresistance and optical Brillouin light scattering setups, which are shortly introduced there.

As previously stated, Section 4 is a purely technical section concerned with the fabrication process of spin torque nano-oscillators in the point contact geometry, with

various forms of top electrodes suited to the various electrical and optical measurements to be performed. The reader who is less interested in the full fabrication process can go along by taking a quick look at Figure 4-1, which depict the four types of devices that are considered in the rest of this text, along with and Figure 4-4, which shows a device cross section, composition and current flow direction.

In Section 5, the results from the electrical and optical measurements are presented and discussed. Section 5.1 considers the observation of the peculiar behavior of resistance and magnetoresistance values in a four-probe measurement. The observations are qualitatively explained through finite element simulations of the current paths in the low resistive point contact devices. Based on the simulation results, a model is constructed that successfully describes the observed resistance and magnetoresistance values and which provides an idea of the intrinsic point contact magnetoresistance, which cannot be directly obtained from a measurement. In Section 5.2, the fabricated point contact devices are observed to produce microwave oscillations upon the application of a direct current and an out-of-plane magnetic field. However, the observed oscillations do not occur in the common GHz frequency range, but rather at relatively low frequencies in the MHz range. This observation is explained by the spin torque driven gyrotropic movement of a magnetic vortex core around a singularity in the point contact center. Section 5.3 presents what is probably the most important achievement of this thesis. There, the first preliminary results of the optical Brillouin light scattering experiments are considered, which illustrate the emission of spin waves in the extended magnetic layer around a point contact device. Various interesting phenomena as well as rich magnetization dynamics are recovered in these results, which form the topic of ongoing research, since some puzzling questions at present remain to be answered.

Section 6 continues with the discussion of both one- and two-dimensional micro-magnetic simulations that study the excitation and propagation of spin waves in a magnetic thin film. Interestingly, these simulations reveal the possibility for confinement of the magnetization dynamics in a restricted area. This localization, together with the dispersive nature of spin wave propagation, can lead to anisotropic behavior of the spin wave radiation in the considered two-dimensional simulations.

Finally, Section 7 presents the conclusions from this thesis and a future outlook on continued research on the subject of spin wave emission and synchronization of point contact nano-oscillator devices.

2. Theory

Many spintronic devices, including the spin torque nano-oscillator devices that are the subject of this thesis, derive their functionality from the anisotropic, giant or tunnel magnetoresistance effect, which allows such a device to show a variable resistance, depending on the magnetic configuration of its layers. Therefore, the nature and physical background of the AMR, GMR and TMR effects are shortly introduced in Section 2.1.

The spin torque effect, which allows a spin-polarized current to interact with the magnetic moment of a free magnetic layer, can change the configuration of a multilayer stack and induce both switching and RF emission in magnetic nano-pillars and RF emission in point contact devices. For example, in Section 5.2, microwave RF emission from a point contact nano-oscillator device is observed upon application of a direct current. The spin torque effect is introduced in Section 2.2, where it is qualitatively explained using the concepts of spin accumulation and spin angular momentum transfer.

To support the study of spin wave emission from a point contact into an extended magnetic free layer, one- and two-dimensional micro-magnetic simulations will be performed in Section 6. These simulations are governed by the Landau-Lifshitz-Gilbert (LLG) equation that describes the dynamic evolution of a magnetic moment, which is subject to a set of torques, generating from the interaction of the magnetic moment with an effective field. Section 2.3 introduces the LLG equation along with the effective field and discusses the specific torques which govern the dynamics of the magnetic moment. When spin torque is included in the magnetization dynamics, a modified Landau-Lifshitz-Gilbert-Slonczewski (LLGS) dynamic equation of motion results.

Finally, Section 2.4 discusses how the magnetostatic theory for spin wave propagation is derived from the LLG and Maxwell equations in the magnetostatic approximation and how the various mode dispersion relations can be understood from simple considerations of the magnetic interaction energy of q spin wave propagating in a magnetic medium. This section may especially be worth reading, as it provides an insightful introduction to the complex world of spin wave propagation. This will aid the reader in the comprehension of the results of the optical BLS experiments and the spin wave propagation simulations which will be presented in later chapters.

2.1. Magnetoresistance

Magnetic multilayer electronic devices derive their functionality from the interaction of electron spin with the magnetic layers constituting the multilayer. By virtue of the AMR, GMR and TMR effects, a current that is sent through a device experiences a resistance that depends on the magnetic configuration of the (multi)layer. Therefore, when placed in a current-limited network, such a device induces a voltage drop that represents the magnetic configuration of the multilayer. This voltage drop can be measured with conventional electrical equipment and allows the magnetic configuration of the device to be deduced. The following sections shortly introduce the AMR, GMR and TMR effects. The GMR effect is discussed in slightly more detail, since it provides the basis for the spin torque point contact nano-oscillators fabricated in this work.

2.1.1. Anisotropic Magnetoresistance

The first manifestation of magnetoresistance in a single magnetic layer was described in 1857 by Thomson, who discovered the anisotropic magnetoresistance (AMR) effect [1]. By virtue of this effect, the resistance a current experiences when flowing through a bulk or film ferromagnetic material depends on the relative orientations of the current density vector ($\vec{J}$) and the local magnetization ($\vec{M}$). The resistance experienced by a current that flows at an angle Θ_{JM} with the magnetization $\vec{M}$ of the material is described by the Voight-Thomson equation [21],

$$R(\Theta_{JM}) = R_{\perp} + \Delta R \cdot \cos^2(\Theta_{JM}). \tag{2-1}$$

In this equation, $R_{\perp}$ corresponds to the low resistance state, which for most ferromagnetic materials [22] occurs in the perpendicular configuration ($\Theta_{JM} = 90°$). With $R_{||}$ representing the high resistance state, the maximal resistance change obtained between the parallel and perpendicular orientations of current and magnetization is represented by ΔR as

$$\Delta R = R_{||} - R_{\perp}. \tag{2-2}$$

Although the AMR effect is a very interesting phenomenon, it is considered of minor importance in the point contact nano-oscillator devices fabricated in this work, as will be discussed in Section 5.1.2.

2.1.2. Giant Magnetoresistance

The giant magnetoresistance (GMR) effect is based on the spin-dependent conductivity a charge carrier experiences when traveling through a magnetic layer, caused by spin-dependent electron scattering processes occurring in the ferromagnetic material. Since its discovery [2][3], the GMR effect has found numerous applications in spintronic devices such as hard disk read heads and magnetic field sensors. The GMR effect is also of crucial importance in this work, since the point contact nano-oscillators that are discussed in the next sections derive their functionality from this particular effect.

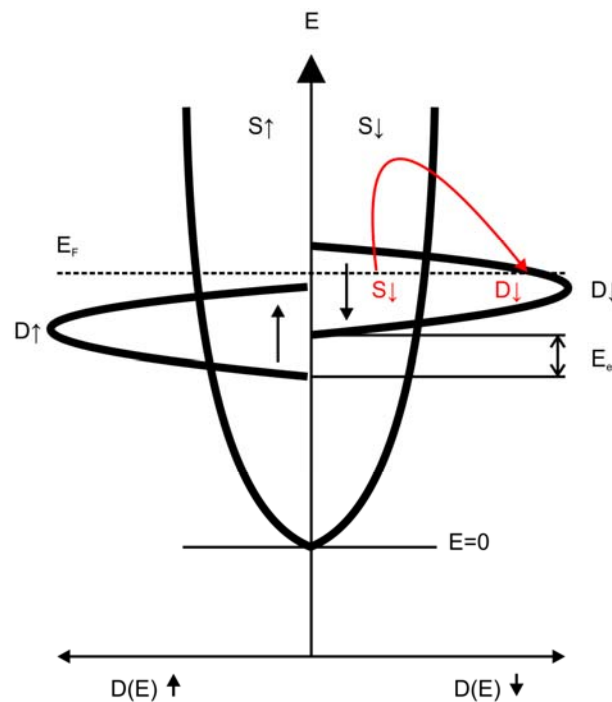

Figure 2-1: Spin-polarized density of states for the conduction s-electrons and the bound d-electrons in a ferromagnetic material. The probability of a scattering event that converts a minority conduction $s_{\downarrow}$ electron at the Fermi level E_F into a minority $d_{\downarrow}$ electron (red arrow) is greater than that of a scattering event that converts a majority conduction $s_{\uparrow}$ electron into a majority d↑ electron, because more states are accessible in the minority $d_{\downarrow}$ electron band. Spin-flip scattering is not considered here.

The physical background of the GMR effect is situated in the spin-polarization of the electron density of states within a ferromagnetic material. This situation occurs in e.g. Ni, which has a $3d^8 4s^2$ outer shells electronic configuration. In the following, majority electrons (↑) are defined as those having their spins parallel to the magnetization of the conducting magnetic material and minority electrons (↓) as those that have their spins anti-parallel. The spin-polarization of the density of states is illustrated in Figure 2-1, which displays the conduction electron $s_{\uparrow\downarrow}$ bands (s electrons are mainly responsible for current conduction, due to their smaller effective mass) and the lower

level $d_{\uparrow\downarrow}$ bands. Due to exchange interactions between the bound d-electrons in a ferromagnetic material, the $d_{\uparrow}$ band is shifted down by the exchange energy E_{ex}, leaving the Fermi level E_F above the (completely filled) $d_{\uparrow}$ band and within the (partially filled) $d_{\downarrow}$ band. Now it is easy to see why conduction electrons from the $s_{\uparrow}$ band undergo less scattering than those of the $s_{\downarrow}$ band. For the $s_{\uparrow}$ electrons, no acceptor-like $d_{\uparrow}$ states are available due to the exchange splitting. However, $s_{\downarrow}$ band electrons will readily scatter into the partially filled $d_{\downarrow}$ band, leading to a lower conductivity for the minority electrons. As a result, the spin-polarized $d_{\uparrow\downarrow}$ electron bands translate into spin-dependent conductivities (due to spin-dependent scattering) for $s_{\uparrow\downarrow}$ conduction electrons having their spins aligned parallel or anti-parallel with the magnetization of the ferromagnetic material.

The GMR effect is typically exploited in the spin valve geometry, i.e. a combination of two ferromagnetic layers, magnetically separated by a conducting, non-magnetic spacer layer, as depicted in Figure 2-2. Usually, the magnetization of one layer (the 'free' layer) in a spin valve is easier to change than that of the other (the 'fixed' layer). This can be accomplished by making the fixed layer thicker than the free layer, thereby increasing its magnetic moment, or by coupling the fixed layer to an (artificial) antiferromagnet. The latter system is known as an exchange-biased spin valve. Figure 2-2 also depicts the two common geometries of current application to the spin valve, i.e. either in the plane of the thin film (current-in-plane geometry, CIP) or perpendicularly to the plane (current-perpendicular-to-plane geometry, CPP).

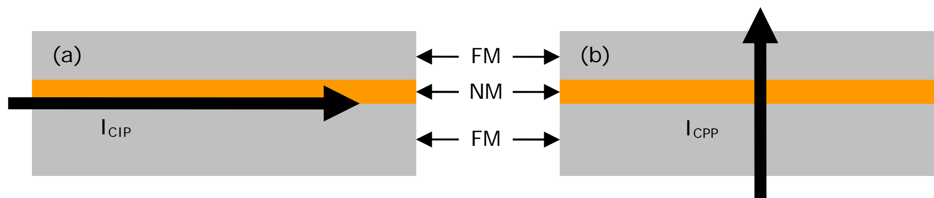

Figure 2-2: A generic spin valve stack consists of a non-magnetic metal layer (NM), sandwiched between two ferromagnetic layers (FM). In the current-in-plane (CIP) geometry (a), the current flows in the plane of the magnetic multilayer, whereas it traverses the multilayer perpendicularly in the current-perpendicular-to-plane (CPP) geometry (b).

A current flowing through a spin valve device will experience a resistance that depends on the relative orientations of the magnetic moments of the layers, according to formula (2.44) from [23]

$$R = R_P + \Delta R \frac{(1-\cos 2\varphi)}{2}. \qquad (2\text{-}3)$$

Here, R_P and R_{AP} are the resistances of the parallel and anti-parallel configurations, 2φ is the angle between the magnetizations of the two ferromagnetic layers and ΔR is the maximum magnetoresistance change, given by

$$\Delta R = R_{AP} - R_P \,. \tag{2-4}$$

A commonly used quantity in the discussion of GMR is the relative magnitude of the GMR effect, expressed in percent, which is defined as

$$MR\ [\%] = \frac{\Delta R}{R_P} \cdot 100 = \frac{R_{AP} - R_P}{R_P} \cdot 100. \tag{2-5}$$

Since the resistance of a device changes with its magnetic configuration, the GMR effect can serve as an effective probe for thin film magnetization dynamics through electrical measurements. Concerning the CPP and CIP geometries, note that, in general, the associated percentages of magnetoresistance change need not be the same, although the magnetoresistance change in magnetic multilayers is usually observed to be largest in the CPP geometry.

At temperatures sufficiently lower than the Curie temperature T_c, spin-flip scattering processes due to spin-magnon interactions extinguish and an electric current flowing in a ferromagnetic conductor can be regarded as composed of two independent flows of majority and minority electrons, as was first stated by Mott [24]. This way, a two-current model is constructed that is characterized by majority and minority spin conductivities $\sigma_\uparrow$ and $\sigma_\downarrow$ or, equivalently, by spin-dependent majority and minority resistances $R_\uparrow$ and $R_\downarrow$. The two-current model of Mott is depicted schematically in Figure 2-3-A and B, for the case of a spin valve. In the parallel configuration of the spin valve layers, the minority current undergoes extensive scattering, while the majority current can travel without much scattering. In the anti-parallel configuration, both spin currents undergo a significant amount of scattering. The equivalent resistance of the parallel network can easily be shown to be larger in the anti-parallel case than in the parallel case, i.e. $R_{AP} > R_P$.

2.1.3. Tunnel Magnetoresistance

A third manifestation of magnetoresistance, tunnel magnetoresistance (TMR), results from the spin-dependent tunneling of conduction electrons in a magnetic tunnel junction (MTJ) device [5][6]. Such a device resembles a spin valve device in that it is composed of two ferromagnetic layers separated by a third, non-magnetic layer. However, in the case of an MTJ device, the conducting spacer layer from the spin valve is replaced by a thin isolating tunnel barrier, such as SiO_2, Al_2O_3 or the recently

more intensively investigated MgO. Rather than spin-dependent scattering, conduction electrons now experience spin-dependent tunneling through the tunnel barrier. Currently, progress is being made in the fabrication of MgO MTJ nano-oscillator devices in the pillar geometry. However, tunnel magnetoresistance will be of no further importance for the point contact devices fabricated in this work, which all build upon the giant magnetoresistance effect generated in the previously introduced spin valve geometry.

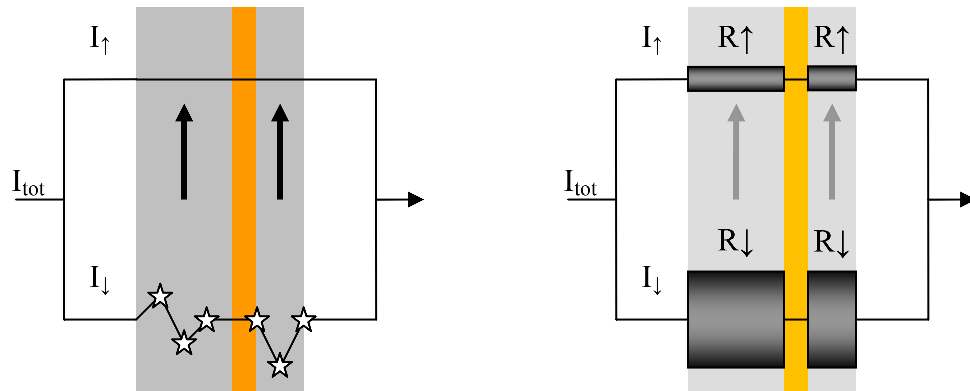

Figure 2-3-A: A spin valve (left) can be represented by a parallel resistor network (right) according to the Mott two-current model. The total current (I_{tot}) is carried by equal numbers of majority and minority charge carriers ($I_{\uparrow}$ and $I_{\downarrow}$), that undergo spin-dependent scattering when they travel through the spin valve magnetic layers. In the parallel configuration, the minority current undergoes extensive spin-dependent scattering, while the majority current can travel with minimal scattering.

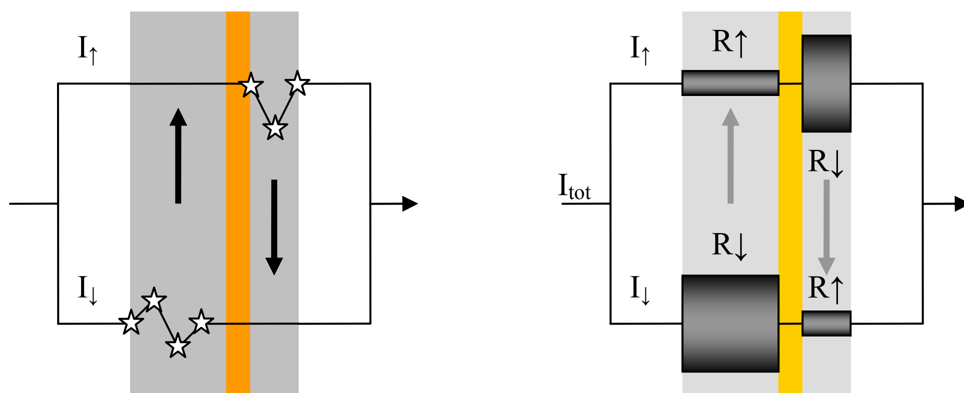

Figure 2-3-B: In the anti-parallel configuration, both spin currents undergo scattering. The equivalent resistance of the parallel network can easily be shown to be larger in the anti-parallel case than in the parallel case, i.e. $R_{AP} > R_{P}$.

2.1.4. Junction Area

Although quite trivial, this section will show that for a uniform current distribution and a constant interface resistivity, the physical MR value (in percent), obtained in a

CPP geometry is independent of the cross-sectional area of the junction interface that generates the MR. This will be an important assumption made in Section 5.1.2, which discusses the construction of a model that tries to explain the observed point contact device magnetoresistance values as a function of size. Figure 2-4 considers two magnetoresistive devices (e.g. point contacts) that differ by a factor 2 in size. A doubling of the point contact size is equivalent to merging two point contacts of the original size. If a single junction with area A has a resistance R_A and displays a magnetoresistance MR_A, a junction of double the size 2A can be regarded as a parallel circuit with resistance $R_A/2$. The corresponding magnetoresistance value MR_{2A} for the parallel circuit is now calculated.

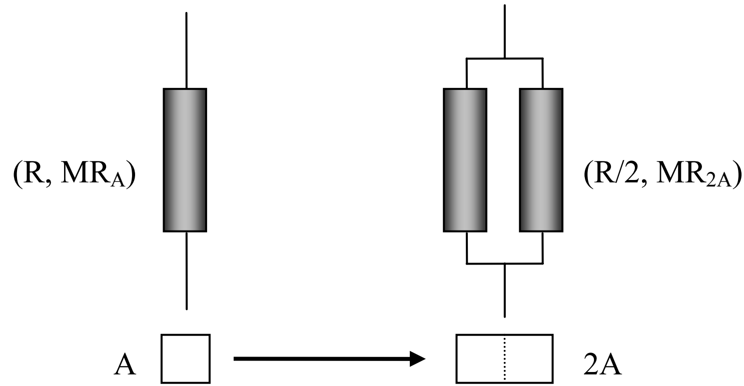

Figure 2-4: Doubling the area of a constant interface resistivity magnetoresistive junction corresponds to the merging of two junctions of half the size. The physical MR values resulting from the considered resistor networks are the same, i.e. $MR_A=MR_{2A}$.

The MR_A value of a magnetoresistive device with junction area A and resistance R_A composed of a base resistance R_0 and a magnetoresistance contribution ΔR_A,

$$R_A = R_0 + \Delta R_A\,, \tag{2-6}$$

is calculated as

$$MR_A \equiv \frac{\Delta R_A}{R_0}\,. \tag{2-7}$$

The resistance resulting from the parallel network of the two devices can be written as

$$R_{2A} = \left(R_A^{-1} + R_A^{-1}\right)^{-1} = \frac{R_A}{2}\,. \tag{2-8}$$

Based on the expression for R_A (2-6), the magnetoresistance change occurring over the parallel network is

$$\Delta R_{2A} = \left(\frac{1}{R_0 + \Delta R_A} + \frac{1}{R_0 + \Delta R_A} \right)^{-1} - \left(\frac{1}{R_0} + \frac{1}{R_0} \right)^{-1}$$

$$= \frac{R_0 + \Delta R_A}{2} - \frac{R_0}{2} = \frac{\Delta R_A}{2} . \qquad (2\text{-}9)$$

With $R_{2A,0} = R_0/2$ the base resistance of the parallel resistor network, the value of the MR effect (in percent) over the parallel network for a point contact of double size then follows as

$$MR_{2A} \equiv \frac{\Delta R_{2A}}{R_{2A,0}} = \frac{\Delta R_A}{2} \cdot \frac{2}{R_0} = \frac{\Delta R_A}{R_0} = MR_A , \qquad (2\text{-}10)$$

In the case of a constant interface resistivity junction, the physical MR value in percent can be concluded to be independent of junction area (the approach can easily be generalized for junctions of arbitrary area). Therefore, in the assessment of the behavior of point contact device resistance as a function of point contact size in Section 5.1, the notion 'RxA product' is used extensively. When the resistance of a constant interface resistivity junction scales inversely with cross-sectional area A, multiplying the device resistance with area yields a constant value, which can be used to characterize a specific type of junction, independent of its size. Together with the MR value, the RxA product forms a set of two (assumed constant) parameters that are characteristic of point contacts of varying size.

2.2. Spin Torque

The spin torque effect [7][8] allows a current of spin-polarized electrons to interact with the moment of a free magnetic layer through the direct exchange of spin angular momentum. The spin torque effect enables some interesting new applications in magnetism. For example, the effect has been shown to be able to switch the direction of magnetization of a magnetic thin film element through the application of a direct current [9][10][11][12][13]. On the other hand, under specific conditions, the spin torque effect can induce a stable precession of the magnetic moment of the element [14][14][15]. Through the GMR or TMR effect, this precession can be translated into an AC voltage and a DC current driven microwave oscillator results, whose frequency can be tuned by controlling the current and external field conditions [14][15]. Present high resolution lithographic techniques allow for the fabrication of spin torque based devices, which require high current confinement (10^7 A/cm^2) for the transfer of spin angular momentum to be effective in influencing the configuration of a magnetic

multilayer. The spin torque effect is considered in further detail in the following sections.

2.2.1. Spin Angular Momentum Transfer

The spin torque effect is a microscopic and purely quantum mechanical effect, based on the conservation of total angular momentum, including that associated with the intrinsic electron spin. In the following, a qualitative picture of the spin torque effect, also called spin-transfer torque effect, is given. A current of spin-polarized electrons will be shown to be able to interact with the moment of a magnetic layer. Therefore, two concepts are introduced. The first is that of spin accumulation due to the spin-dependent GMR-like scattering process occurring at interfaces between a ferromagnet and a normal metal. Secondly, the concept of spin angular momentum transfer between a current and a ferromagnet is introduced, which is driven by the spin accumulation effect.

2.2.1.1. Spin Accumulation

In analogy with the spin-dependent bulk scattering process that was introduced in the discussion of the GMR effect in Section 2.1.2, interfacial spin-dependent scattering occurs at the interfaces between a normal and a ferromagnetic metal. This is depicted in Figure 2-5 (a). At an interface, majority spins are preferentially transmitted from the normal metal into the ferromagnet, leading to a spin-polarization of the electron current traveling to the right. Accordingly, when injected from a ferromagnet into a normal metal, as depicted in Figure 2-5 (b), a spin-polarized current maintains its polarization over a distance expressed by the spin diffusion length l_{sf}, which is of the order of 450 nm for Cu [5].

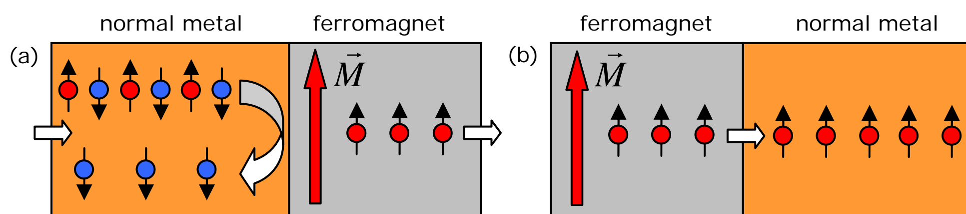

Figure 2-5: (a) Due to spin-dependent interface scattering, majority spins are preferentially transmitted into a ferromagnetic metal, leading to a spin-polarization of the electron current traveling to the right. (b) Accordingly, a spin-polarized current maintains its polarization over a certain distance when injected into a normal metal, expressed by the spin-diffusion length l_{sf}.

When the two structures of Figure 2-5 are joined, a metal-ferromagnet-metal heterostructure results, as indicated in Figure 2-6. Due to the spin-dependent scattering at the first interface, minority electrons will accumulate in the region close to the interface, while the majority electrons proceed through the ferromagnet, experiencing reduced scattering. Therefore, at the right interface, a majority spin accumulation results. This spin accumulation offsets the local equilibrium spin moment density M_S by an amount $\Delta M(z) = M(z) - M_S$.

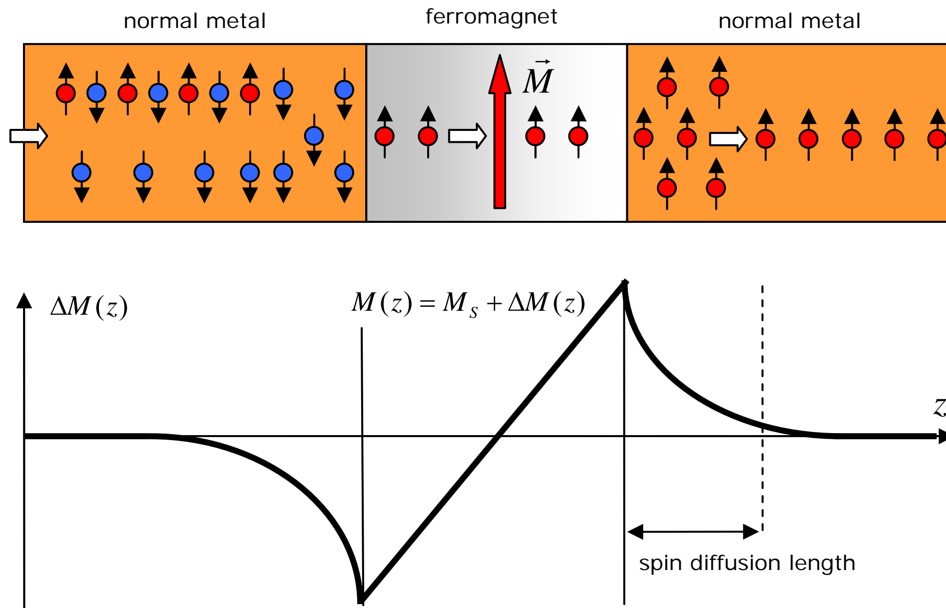

Figure 2-6: Due to the spin-dependent scattering at the first metal-ferromagnet interface, minority electrons will accumulate in the region close to the interface, while the majority electrons travel freely through the ferromagnet. Therefore, at the second interface, a majority spin accumulation results. This spin accumulation offsets the local equilibrium spin moment density M_S by an amount $\Delta M(z) = M(z) - M_S$.

2.2.1.2. *Spin Transfer*

Now the concept of spin accumulation has been introduced, it will be shown how this effect can drive spin transfer, which induces a torque on the moment of a magnetic layer. Therefore, consider the structure displayed in Figure 2-8, which is nothing more than a conventional spin valve, as introduced in Section 2.1.2. One of the layers of this spin valve is assumed to keep its magnetization fixed in a certain direction. This layer is from now on called the 'fixed' layer and its magnetic moment is designated by $\vec{M}_{fixed}$. The magnetic moment of the other, 'free' magnetic layer is more easily influenced and its moment is designated by $\vec{M}_{free}$. The magnetic moment of the free layer can make an arbitrary angle with that of the fixed layer.

For a current flowing from the first normal metal (I) to the free magnetic layer, majority electrons that have their spins in the direction of the free layer magnetization are preferentially transmitted, while the anti-aligned electrons are preferentially reflected. As outlined in the previous section, a spin polarized current results in the second normal metal (II).

Before continuing, note that an arbitrary incoming electron generally does not need to have its spin perfectly aligned or anti-aligned with that of the magnetic moment of the ferromagnetic layer. However, according to quantum mechanics, every spin state can be considered as a coherent superposition of spin up and spin down states, which are characterized by distinct transmission and reflection probabilities (see Figure 2-7). Therefore, for clarity in Figure 2-8, the majority spin component can be considered to be fully transmitted, while the minority component is fully reflected.

$\vec{M}$ θ = A + B

Transmission probability ~ $|A|^2$

Reflection probability ~ $|B|^2$

Figure 2-7: An arbitrary spin state can be decomposed into a coherent superposition of spin up and spin down states, characterized by distinct transmission and reflection probabilities.

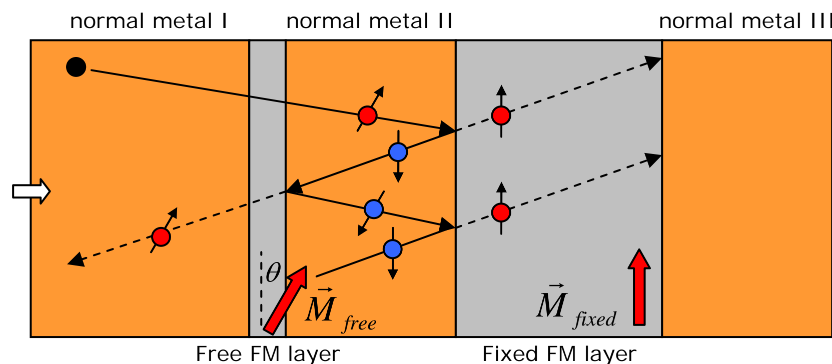

Figure 2-8: Multiple spin-dependent reflection and transmission within a spin valve magnetic multilayer geometry. The applied current corresponds to electrons traveling from the left to the right.

The spin polarized current in the second normal metal (II) then meets the fixed magnetic layer. Again, the majority component of the spin state is assumed to be transmitted, while the minority component is reflected back towards the free magnetic layer. At the interface with the free layer, the free layer majority component is

transmitted to the left, while the minority component is scattered and re-reflected towards the fixed layer. Then the process described above repeats itself.

It is instructive to look at what happens at the interface between the free magnetic layer and the normal metal (II), as illustrated in Figure 2-9. The fixed ferromagnet spin down state is composed of the spin up and spin down states of the free layer. The spin up component is transmitted towards the left, while the spin down component is reflected towards the right. Thus, considering the incoming and outgoing spin at the interface, the free layer must have exerted a torque $\vec{\tau}$ on the spin down state of the fixed layer, since this state is reflected as a spin down state of the free layer. Due to the conservation of total angular momentum, the free layer is subject to a reaction torque, $-\vec{\tau}$. In the small current limit, this reaction torque is annihilated by the damping torque, $\vec{T}_{damping}$. In the high current limit, however, the torque $-\vec{\tau}$ is driven by the increased spin accumulation near the interface so that the damping torque may be overcome and the free layer will respond with a change of its magnetization direction. Generally speaking, the torque induced by the free layer on the incoming moment is proportional to the angle of the free layer magnetization with respect to the fixed layer magnetization. Therefore, the situation depicted here is intrinsically unstable and switching of the free layer moment by the spin torque can be attained. Also note that the spin valve depicted in Figure 2-8 needs to show broken symmetry with respect to the magnetic moments of the free and fixed layer, otherwise no net action due to the spin-transfer torque would occur. Moreover, the thickness of the normal metal (III) spacer layer should be maintained sufficiently small to ensure spin conservation in accordance with the spin diffusion length. Finally, note that the transmitted and reflected spins have no resulting transverse components to the magnetization of the polarizing layer, so essentially the transverse spin component is adsorbed.

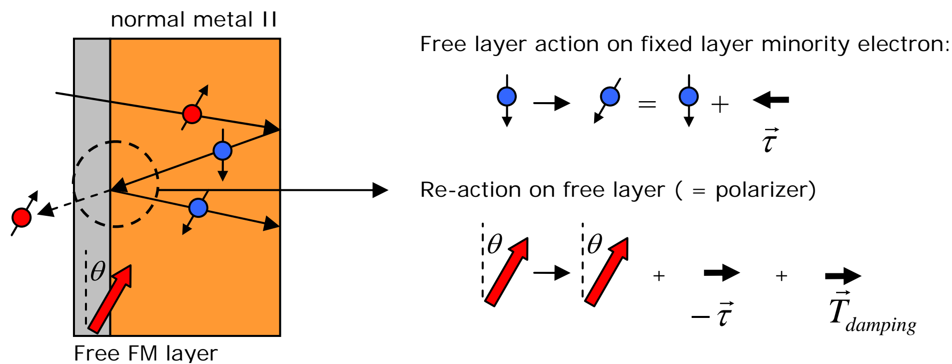

Figure 2-9: Detail of the scattering process at the interface between the free magnetic layer and normal metal II. The free layer exerts a torque on reflected spin.

Apart from the process described above, based on spin dependent scattering of the conduction electrons, the absorption of the transverse component of the spin current can also be deduced from a classical dephasing of the electron spins in the ferromagnetic material. This dephasing is due to the fact that majority and minority electrons have different wave vectors in the ferromagnet. A detailed description of this process can be found in [26].

2.2.2. Spin Transfer Dynamics

The previous section provided a qualitative picture of the spin torque action. For a complete physical picture, the spin torque effect has to be considered in a purely quantum mechanical context, which is beyond the scope of this text. The interested reader is instead referred to some excellent review articles [26][27][28]. According to [29], the spin angular momentum transfer induces a torque on the magnetic moment of a free layer in a spin valve geometry (see Figure 2-10, where $\vec{M}_{free}$ is the magnetization vector of the free layer and $\hat{M}_{fixed}$ a unit vector in the spin-polarization direction of the incoming current) which can be written as

$$\vec{T}_{ST} = -g(\theta)\cdot(\hbar/2e)\cdot\frac{\eta I}{M_s}\cdot\vec{M}_{free}\times\left(\vec{M}_{free}\times\hat{M}_{fixed}\right). \qquad (2\text{-}11)$$

In this formula, M_s is the saturation magnetization, I the total current, e the magnitude of the electron charge, $\hbar$ the reduced Planck constant, g a pre-factor which depends on the angle between the magnetic moments of the polarizing and free layer, and η the spin-polarization factor expressed in terms of the spin up and spin down currents, η = $(I_\uparrow - I_\downarrow)/(I_\uparrow + I_\downarrow)$.

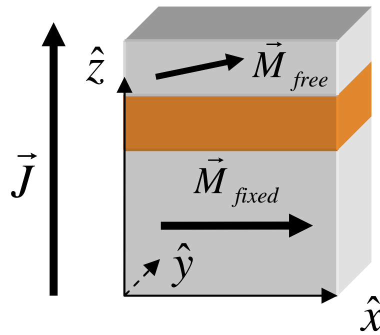

Figure 2-10: Orientation of $\vec{M}_{free}$ (magnetization of the free layer) and $\hat{M}_{fixed}$ (unit vector along the pinned magnetization direction of the fixed layer). The current traverses the spin valve stack perpendicularly to the film plane (CPP geometry).

In case of complete absorption of the transverse spin component of a spin-polarized current, the factor g equals a constant value of 1 and, with $a_j = (\hbar / 2e)\eta I$, the torque can be written as

$$\vec{T}_{ST} = -\frac{a_j}{M_s} \cdot \vec{M}_{free} \times \left(\vec{M}_{free} \times \hat{M}_{fixed} \right). \tag{2-12}$$

This term has to be added to the dynamic equation of motion for the free ferromagnetic layer moment, which will be introduced in Section 2.3. Note from the last equation that the spin torque is proportional to the current and to the degree of spin-polarization of that current. On the other hand, it is inversely proportional to the saturation magnetization of the free magnetic layer.

2.3. Magnetization Dynamics

2.3.1. Landau-Lifshitz-Gilbert-Slonczewski Dynamic Equation

The time rate of change of a macroscopic magnetic moment in an effective magnetic field, without the inclusion of spin torque action, is captured by the Landau-Lifshitz-Gilbert-Slonczewski equation [30][31], which takes the Landau-Lifshitz form

$$\frac{d\vec{M}}{dt} = -|\bar{\gamma}| \cdot \vec{M} \times \vec{H}_{Eff} - \frac{|\bar{\gamma}| \cdot \alpha}{M_s} \cdot \vec{M} \times \left(\vec{M} \times \vec{H}_{Eff} \right), \tag{2-13}$$

which is equivalent with the Gilbert form

$$\frac{d\vec{M}}{dt} = -|\gamma| \cdot \vec{M} \times \vec{H}_{Eff} + \frac{\alpha}{M_s} \cdot \vec{M} \times \frac{d\vec{M}}{dt} \tag{2-14}$$

under the transformation $\gamma = (1 + \alpha^2) \cdot \bar{\gamma}$, with $\vec{M}$ the macroscopic magnetization vector, $\vec{H}_{Eff}$ the effective magnetic field that acts upon the magnetization vector, γ the Gilbert electron gyromagnetic ratio, $\bar{\gamma}$ the Landau electron gyromagnetic ratio, M_s the saturation magnetization and α the dimensionless Gilbert damping parameter. The first term on the right hand side of equation (2-13) or (2-14) expresses precession of the magnetic moment around the direction of the effective magnetic field, while the second term describes a phenomenological damping of the magnetic moment towards the direction of the effective field. The associated precession and damping torques are described in Section 2.3.1.1 and 2.3.1.2. In Section 2.3.1.3, the LLG equation is extended with an extra term due to the spin torque a spin-polarized

current exerts on the magnetic moment. The various contributions to the effective field are discussed in Section 2.3.1.4

2.3.1.1. Precession Torque

The first term on the right hand side of equation (2-13) can be understood from the classical model of an atom, as depicted in Figure 2-11. In this figure, an electron proceeds along a circular orbit around an atomic nucleus. The radius of the orbit is given by r and the electron is further characterized by its mass m_e, charge e^- and velocity $\vec{v}$. From Ampere's law, the magnetic moment $\vec{\mu}_L$ associated with the orbiting electron charge can be calculated as

$$\vec{\mu}_L = I \cdot \vec{A} = -e \cdot f \cdot \vec{A} = -e \cdot \frac{v}{2\pi r} \cdot \pi r^2 \cdot \hat{z} = -\frac{evr}{2} \cdot \hat{z} . \qquad (2\text{-}15)$$

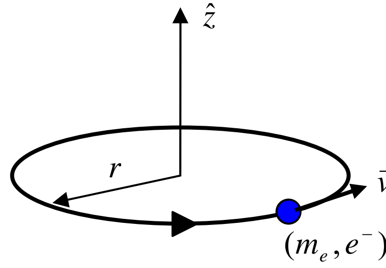

Figure 2-11: Classical representation of an atom: an electron with mass m_e and charge e^- proceeds with velocity $\vec{v}$ along a circular orbit with radius r around the atomic nucleus. The $\hat{z}$-direction is perpendicular to the plane of the circular orbit.

In equation (2-15), I is the current associated with the circular electron movement, e is the magnitude of the electron charge ($e = 1.6 \cdot 10^{-19}$ C), $f = T^{-1}$ with T the period of the circular motion and $\hat{z}$ is a unit vector along the $\hat{z}$-direction as indicated in Figure 2-11. In addition to a magnetic moment, the orbital movement of the electron mass is associated with an angular momentum, expressed through the classical definition

$$\vec{L} = \vec{r} \times m_e \vec{v} = r m_e v \cdot \hat{z} . \qquad (2\text{-}16)$$

Apparently, the orbital angular momentum (2-16) of the electron and its magnetic moment (2-15) are opposite, while the relation between their magnitudes is given by the orbital magnetogyric ratio γ_L, according to

$$\gamma_L \equiv \frac{\mu_z}{L_z} = -\frac{evr}{2} \cdot \frac{1}{r m_e v} = -\frac{e}{2m_e} = -\frac{\mu_B}{\hbar} . \qquad (2\text{-}17)$$

The last equality expresses the orbital gyromagnetic ratio in terms of the Bohr magneton μ_B (μ_B = 9.27400949 × 10^{-24} J·T^{-1}) and reduced Planck constant $\hbar$ ($\hbar$ = 1.054571628 × 10^{-34} J·s). Note that, due to the anti-parallel orientation of the z-components of the magnetic moment and the angular momentum, the orbital magnetogyric ratio γ_L is a negative number. To avoid sign inconsistencies, the gyromagnetic ratio will be entered into the LLG equation as $-|\gamma_L|$.

The derivation of the electron magnetic moment was based on the orbital movement of the electron around the atomic nucleus. In addition to its orbital angular momentum, an electron also possesses an intrinsic spin angular momentum that produces an associated spin magnetic moment. Since the spin angular momentum is known to be twice as effective in the generation of magnetic moment, the spin gyromagnetic ratio requires an additional factor of 2, which is known as the g-factor or Landau factor, so that

$$\gamma_S = -2 \cdot \frac{\mu_B}{\hbar}. \quad (2\text{-}18)$$

In ferromagnetism, it is mainly the spin magnetic moment of uncompensated electrons in d-shells of transition metal atoms that accounts for the strong magnetization observable below the Curie temperature T_c. In radial units, the spin gyromagnetic ratio for a free electron is approximately 176 GHz/T. The conversion from angular frequency to regular frequency results in $\gamma_S \approx 28$ GHz/T.

According to classical mechanics, the torque on a body can be expressed as the time derivative of its angular momentum

$$\vec{\tau} = \frac{d\vec{L}}{dt}, \quad (2\text{-}19)$$

whereas the torque on a (magnetic) dipole in a (magnetic) field is

$$\vec{T}_P \equiv \vec{\tau} = \vec{\mu} \times \vec{H}_{Eff}. \quad (2\text{-}20)$$

This precession torque $\vec{T}_P$ is perpendicular to both the magnetic moment and the effective field and therefore leads to a precession of the magnetic moment around the effective field direction, as shown in Figure 2-12. Using the expression for the gyromagnetic ratio (2-17), the time rate of change of the magnetic moment can now be written as

$$\frac{d\vec{\mu}_i}{dt} = \gamma \cdot \frac{d\vec{L}_i}{dt} = \gamma_i \cdot \vec{\tau} = \gamma_i \cdot \left(\vec{\mu}_i \times \vec{H}_{Eff}\right). \quad (2\text{-}21)$$

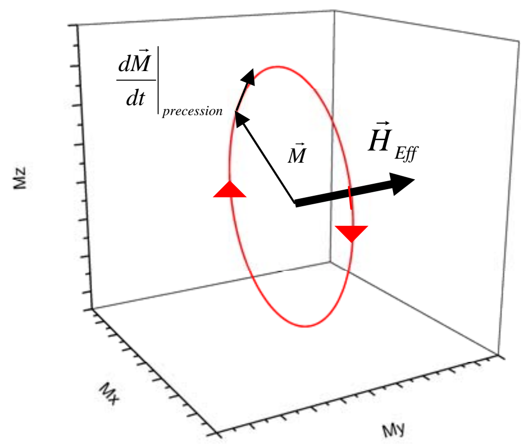

Figure 2-12: Due to the precession torque $\vec{T}_P$, the magnetic moment precesses around the direction of the effective field $\vec{H}_{Eff}$.

The subscript *i* indicates the validity of the equation for both the orbital (L) and spin (S) magnetic moment. In the macro-spin approximation, a large number of individual moments may take part in a coherent precession of the magnetization $\vec{M}$ and the last equation becomes

$$\left.\frac{d\vec{M}}{dt}\right|_{precession} = -|\gamma| \cdot \vec{M} \times \vec{H}_{Eff} \, . \tag{2-22}$$

2.3.1.2. Damping Torque

The precession torque $\vec{T}_P$, described in the previous section, can induce but a stable precession of the magnetic moment around the direction of the effective field. Without dissipation, magnetic energy minimization through alignment of the magnetic moment with the effective field will never occur. Therefore, Gilbert introduced a phenomenological damping torque [30], which tends to align the magnetic moment with the effective field and provides a mechanism for energy minimization through dissipation, as depicted in Figure 2-13. Gilbert damping is often considered viscous dissipation because it is proportional to $d\vec{M}/dt$. The corresponding term to be added to the equation of motion (2-22) reads

$$\left.\frac{d\vec{M}}{dt}\right|_{damping} = +\frac{\alpha}{M_s} \cdot \vec{M} \times \frac{d\vec{M}}{dt} \, . \tag{2-23}$$

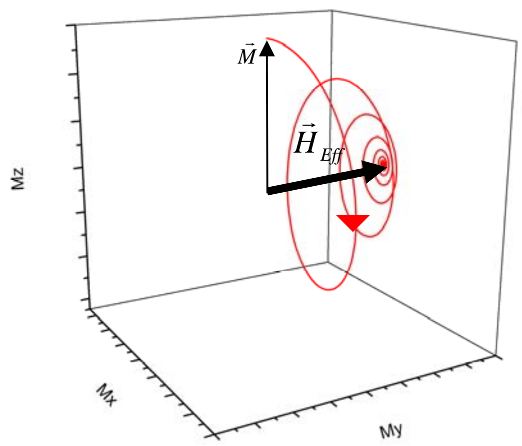

Figure 2-13: The effect of the damping torque is to align the initial magnetic moment $\vec{M}$ with the effective field $\vec{H}_{Eff}$.

2.3.1.3. Spin-Transfer Torque

A spin-polarized current can transfer spin angular momentum between magnetic layers with different directions of their magnetization [7][8]. This effect can be incorporated into the LLG equation of motion through the addition of an extra spin torque term, which can be written in a form similar to that of the Gilbert damping term. According to equation (2-12) of Section 2.2.2, the torque $\vec{T}_{ST}$ exerted on the magnetic moment $\vec{M}$ of a free spin valve layer through the action of a current that was spin-polarized by a fixed ferromagnetic layer whose unit magnetization vector $\vec{M}_{fixed}$ is pinned along the $\hat{x}$-direction (see Figure 2-10), can be written in the form (the parameters M_s and a_j have been introduced in Section 2.2.2)

$$\vec{T}_{ST} = -\frac{a_j}{M_S} \cdot \vec{M}_{free} \times \left(\vec{M}_{free} \times \hat{M}_{fixed} \right). \qquad \text{(2-24)}$$

The corresponding term to be added to the Gilbert form of the LLG equation is

$$\left. \frac{d\vec{M}}{dt} \right|_{ST} = +\frac{|\gamma| \cdot a_j}{M_S} \cdot \vec{M}_{free} \times \left(\vec{M}_{free} \times \hat{M}_{fixed} \right). \qquad \text{(2-25)}$$

When all previously described torques due to precession, damping and spin-transfer are included, the full LLGS equation results as

$$\frac{d\vec{M}}{dt} = -|\gamma| \cdot \vec{M} \times \vec{H}_{eff} + \frac{\alpha}{M_S} \cdot \vec{M} \times \frac{d\vec{M}}{dt} + \frac{|\gamma| \cdot a_j}{M_S} \cdot \vec{M}_{free} \times \left(\vec{M}_{free} \times \hat{M}_{fixed} \right). \qquad \text{(2-26)}$$

Figure 2-14 summarizes the effect of the three different torques discussed above on the movement of a magnetic moment. Note that the spin torque can be considered as a negative contribution to the conventional Gilbert damping. For sufficiently high currents, the spin torque term can balance the damping force, resulting in a stable, sustained precession, or it can induce magnetization reversal for currents above a critical current [32] given by

$$I_C = \left(\frac{2e}{\hbar}\right)\left(\frac{\alpha}{P}\right) V M_S (H + H_K + \frac{M_S}{2}) . \tag{2-27}$$

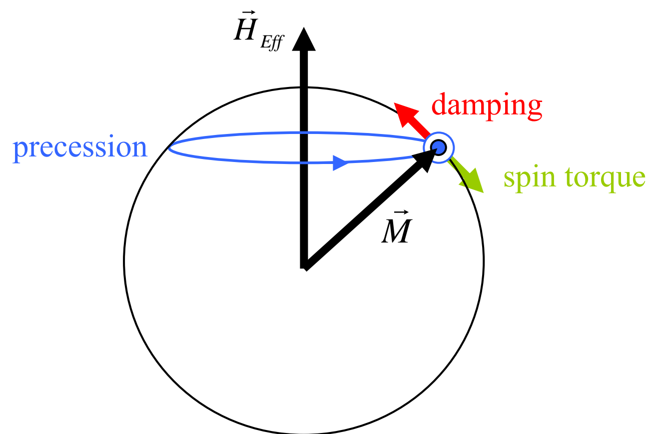

Figure 2-14: The three contributions to the magnetization dynamics define the motion of a magnetic moment in an effective field, subject to precession, damping and spin torque. The spin torque can act as a negative damping contribution and can either enable a stable precession when the damping is perfectly balanced, or lead to magnetization reversal (switching) when the damping torque is overcome.

2.3.1.4. The Effective Field

The LLG(S) equation of motion describes the time evolution of a magnetic moment resulting from the precession, damping and spin-transfer torques that act upon it. In this section, the various contributions to the effective field $\vec{H}_{Eff}$ which occurs in the LLG(S) equation are evaluated. The effective field can be written in the form

$$\vec{H}_{Eff} = \vec{H}_{app} + \vec{H}_{ani} + \vec{H}_{demag} + \vec{H}_{oersted} + \vec{H}_{ex} + \vec{H}_{magnon}(t) . \tag{2-28}$$

Applied field. H_{app} represents an externally applied magnetic field, which can be either static or varying with time and is assumed uniform over the volume of the macroscopic magnetic moment for which the LLG(S) equation is solved. The

magnetization dynamics result from the Zeeman interaction of the magnetic moment with the applied field, which tends to align the moment with the field direction.

Anisotropy field. H_{ani} is any field contribution resulting from the intrinsic magnetic properties of the material. For example, the material can exhibit uniaxial, fourfold or perpendicular variants of crystalline anisotropy. As another example, in a patterned spin valve device, the exchange bias pinned layer can induce a stray field coupling on the free layer. The anisotropic behavior of such systems can be represented by the presence of an effective field contribution which adds to the external field.

Demagnetization field. H_{demag} is any effective field contribution due to shape anisotropy of the magnetic configuration. This shape anisotropy results from free magnetic poles located at the boundaries of a magnetic structure. For example, elongated high aspect ratio structures display a strong axial anisotropy with an easy axis defined along the axial direction.

Oersted field. $H_{oersted}$ is the field contribution resulting from the application of a current distribution in or near a magnetic structure. This contribution can take very complex forms depending on how the current flow is distributed. Note that for current-driven spin torque nano-oscillators, this field may play an important role in the resulting magnetization dynamics.

Exchange field. H_{ex} represents the effective (molecular) field due to exchange interactions. Formally, exchange interaction is a purely quantum mechanical effect based on the Pauli exclusion principle which, in a first order approximation, only acts between nearest neighbor spins of a spin lattice. Therefore, the contribution H_{ex} is not to be regarded as a field in the classical sense. However, according to equation (10-10.3) of [36], the exchange interaction is accounted for in the LLG(S) equation through the addition of an effective field term of the form

$$\vec{H}_{ex} = \frac{2A}{M_s^2} \cdot \nabla^2 \vec{M} = \frac{D}{M_S} \cdot \nabla^2 \vec{M} \ , \qquad (2\text{-}29)$$

with M_s the saturation magnetization, A the exchange constant (in $J \cdot m^{-1}$) and D the exchange stiffness constant (in $J \cdot T^{-1} \cdot m^{-1}$), defined as

$$D \equiv \frac{2A}{M_S} . \qquad (2\text{-}30)$$

For an isolated macroscopic magnetic moment, this term of course has no meaning. However, when moving to micro-magnetic simulations, which consider an array of

coupled spins, exchange interactions have to be incorporated as they are of considerable importance in the evaluation of short range dynamics.

For wavelike magnetization distributions (such as the spin waves to be considered in the next section), equation (2-29) produces a quadratic behavior of the exchange field contribution with wave number q (see equation (2-34) for the definition of q), indicating that exchange interactions become increasingly important for sufficiently small wavelengths. The exchange field is then written as [36]

$$\vec{H}_{ex} = D \cdot q^2 . \tag{2-31}$$

Dipolar field. Finally, H_{magnon} is a dynamic, non-uniform demagnetizing contribution due to the propagation of magnons (spin waves) in a magnetic structure. To account for the dynamic nature of these magnons, the time dependence of this contribution was written explicitly. Whereas the exchange contribution to the effective field was observed to scale with the square of the wave vector of a magnetization wave, the dipolar field contribution can be shown to scale with wave vector q. This provides an important consequence for the spin wave dispersion relations which will be discussed in the next section. At small wavelengths (corresponding to large wave vectors q), the exchange energy will be dominant, leading to a quadratic increase of the spin wave frequency with q. On the other hand, these exchange interactions will be unimportant for long wavelengths (small q) so that in that range the waves are essentially characterized by dipole interactions. Consequently, long wavelength waves will be dominated by dipole-dipole interactions, whereas the exchange coupling will be prominent in small wavelength dynamics.

2.4. Spin Wave Theory

2.4.1. Spin Waves

Spin waves, also known as magnons, are the low lying excitations of a magnetic spin system from its equilibrium ground state [33]. They can be regarded as wavelike, small amplitude deviations of a series of magnetic moments from their equilibrium, minimum energy directions. One important achievement of spin wave theory was the formulation of the Bloch $T^{3/2}$ law that describes the observed reduction of spontaneous magnetization in a ferromagnet when the Curie temperature is approached [34]. Figure 2-15 illustrates a spin wave in an otherwise perfectly ordered system of magnetic moments aligned with the z-axis. The springs represent the exchange interaction between neighboring spins at the microscopic level, which was discussed in Section 2.3.1.4. As stated there, the exchange interaction is the major

interaction to be considered for short wavelength spin waves. For longer wavelength spin waves, dipolar stray fields from neighboring volumes of magnetic moment become dominant in determining the spin wave character. The following sections discuss spin wave propagation for the case of a thin film in more detail.

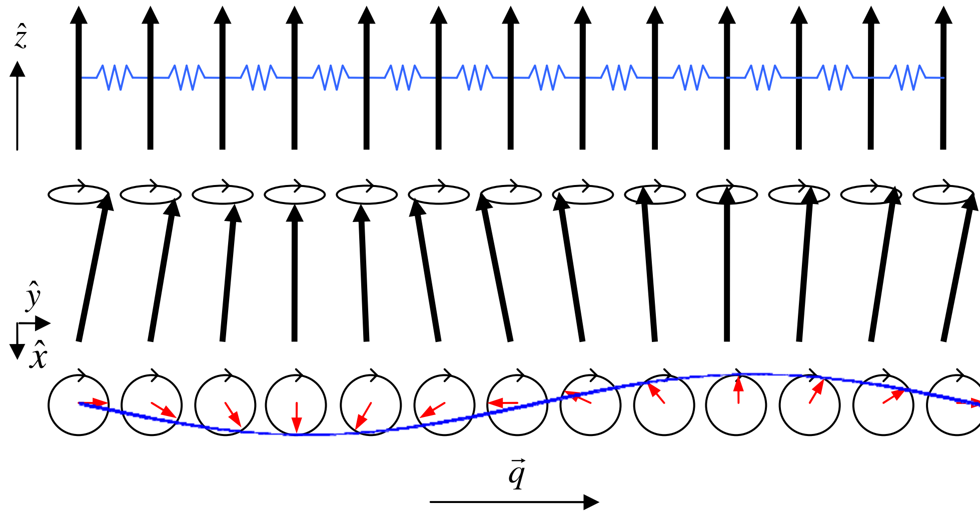

Figure 2-15: Representation of a spin wave running through an exchange coupled spin system. The springs represent the exchange interaction between nearest neighbor spins. In equilibrium, all spins are aligned in the z-direction. The spin wave (blue line) is characterized by deviations of the magnetic moments from their equilibrium position in the x- and y-directions. The spin wave is represented by its wave vector $\vec{q}$.

2.4.2. Spin Wave Propagation

In analogy with conventional plane wave theory, a spin wave is characterized by an amplitude and a wave vector $\vec{q}$, defined as

$$\vec{q} = \frac{2\pi}{\lambda} \cdot \hat{n} . \tag{2-32}$$

Here, λ is the wavelength of the spin wave and $\hat{n}$ is a unit vector that points in the direction of propagation. Figure 2-15 displays the wave vector associated with the spin wave shown there.

For the case of an extended isotropic magnetic thin film, various modes of spin wave propagation are analytically known. A distinction is usually made between the long wavelength, magnetostatic modes which are governed by long range dipolar interactions and the short wavelength, exchange dominated modes. The intermediate

range is covered by spin waves that bear a combination of dipolar and exchange character. These are commonly referred to as the hybrid dipolar-exchange spin waves.

The term ‘magnetostatic’ originates from the fact that for a given wave number, the frequency of the spin wave mode is much smaller than the frequency of the associated electromagnetic mode, so that the magnetostatic approximation (see Appendix A of [35]) can be used for solving the Maxwell equations. Although the magnetostatic mode wavelengths are shorter than their electromagnetic counterparts, they remain sufficiently long so that exchange interactions can be neglected. Therefore, magnetostatic modes are effectively dominated by dipolar interactions.

The magnetostatic mode theory that was first established by Damon and Eshbach [37] distinguishes between three main propagating modes, depending on the relative orientations of the magnon wave vector and the internal field in the thin film. These modes are known as the magnetostatic surface wave (MSSW), the magnetostatic backward volume wave (MSBVW) and the magnetostatic forward volume wave (MSFVW), whose field and wave vector orientations are depicted in Figure 2-16. Note that this figure only shows the ‘pure’ modes for in-plane propagation at perpendicular (MSSW and MSFVW) and parallel (MSBVW) directions with the field. Theoretically, spin wave propagation in an arbitrary direction relative to the field is possible, so that a mode can display a mixed character, although critical angles separate the modes between MSSW and MSBVW behavior [35].

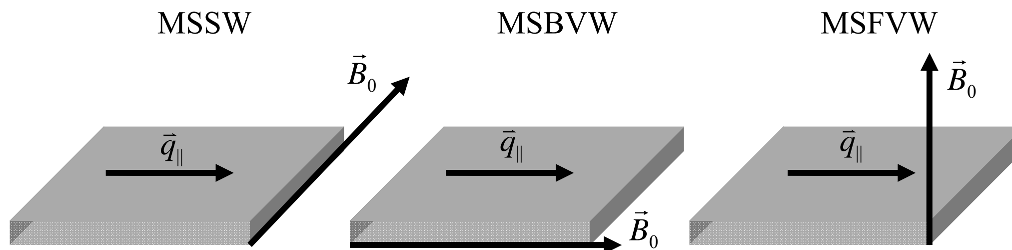

Figure 2-16: MSSW, MSBVW and MSFVW magnetostatic mode geometries of in-plane wave-vector ($\vec{q}_{||}$) and externally applied field ($\vec{B}_0$) for spin wave propagation in an extended magnetic thin film.

The modes introduced above are characterized by distinct dispersion relations that map the relation between mode frequency and wave vector. These dispersion relations can be calculated based on the energy contributions due to the different magnetic interactions at play. The relative energy contributions from the long range dipolar interaction and the short range exchange interaction (which is usually considered to act between nearest neighbors) determine whether a spin wave is dipolar or exchange dominated. Whereas the nature of the exchange interaction predicts a quadratic

dependence of frequency on wave vector (see Section 2.3.1.4 or [36]), the dipolar interaction scales inversely with distance, leading to a linear wave vector dependence. Only for sufficiently small wavelengths, the exchange contribution can no longer be neglected and should be included in the calculation of the modes. An excellent review of the magnetostatic mode theory for in-plane magnetized films, including a derivation of the governing dispersion relations is provided in [35]. These dispersion relations can also be found, in a slightly different form, in [38]. The following sections discuss the nature of the three main magnetostatic modes and introduce the dispersion relations that characterize them. These relations will be applied in the understanding of the optical Brillouin light scattering (BLS) experiments in Section 5.3 and are used to validate the results from the micro-magnetic simulations in Section 6.

2.4.2.1. Magnetostatic Backward Volume Wave

In the MSBVW dipolar mode geometry, the thin film is saturated in the in-plane $\hat{x}$-direction ($\vec{B}_0 = B_0 \cdot \hat{x}$) and spin waves have their in-plane wave vector $\vec{q}_{\|}$ in the $\hat{x}$-direction as well. These spin waves are characterized by deviations of the magnetic moments from the equilibrium $\hat{x}$-direction which can be decomposed in an out-of-plane ($\hat{z}$) and an in-plane ($\hat{y}$) part, as depicted in Figure 2-17.

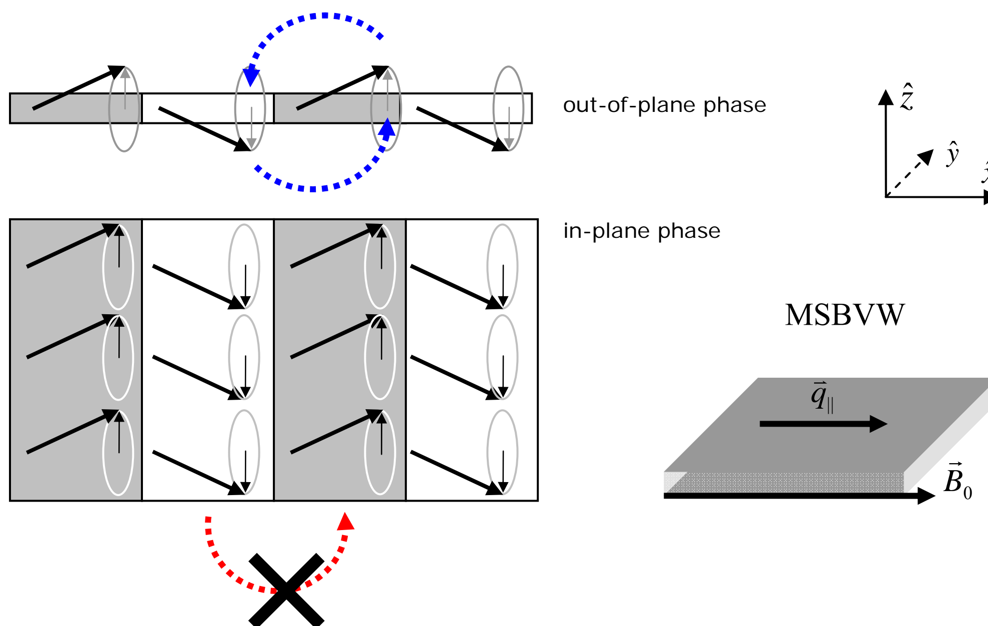

Figure 2-17: In the MSBVW dipolar mode geometry, the deviations of the magnetic moments from their equilibrium x-direction can be decomposed in an out-of-plane and an in-plane phase. In the out-of-plane phase, the dipolar stray fields from neighboring volumes of magnetic moment lead to mode softening, whereas no stray fields are present in the in-plane phase, due to the infinitely extending thin film.

It is illustrative to consider the pure out-of-plane and in-plane phases to gain insight into the MSBVW mode behavior. During the out-of-plane phase, the deviations in the magnetic moment of adjacent thin film volumes oppose each other. Apart from the restoring fields that are present due to demagnetization effects (i.e. thin film in-plane shape anisotropy), the dipole moments experience additional stray fields from neighboring volumes of magnetization that tend to anti-align adjacent units of magnetic moment. Note that, with increasing wavelength, the volumes that are to be considered as magnetic dipoles grow larger as well. However, the average magnetization deviation stays the same, while the dipole interaction strength decreases with distance (i.e. wavelength). Therefore, for larger wavelengths (decreasing $\vec{q}_{\|}$), the energy minimization due to the dipole interaction is less effective. Accordingly, for smaller wavelengths (increasing $\vec{q}_{\|}$) the dipole interaction is stronger and a unit of magnetization experiences a stronger stray field that pushes its magnetization further out-of-plane. This leads to a mode softening with associated frequency decrease, which is expressed through the characteristic negative dispersion that is typically observed for the MSBVW mode. During the in-plane phase, due to flux closure (actually, non-closure, since it is an infinitely extending film), adjacent volumes experience no in-plane stray fields and thus no $\vec{q}_{\|}$-dependent restoring force. The dispersion relation that results for the dipolar MSBVW mode is given by [39] (note that both H and M_s are expressed in A/m here)

$$f_{MSBVW} = \frac{\gamma\mu_0}{2\pi}\sqrt{H_{app}\left(H_{app} + M_s\frac{1-e^{-q_{\|}d}}{q_{\|}d}\right)}. \tag{2-33}$$

In this equation, the reduction of the thin film in-plane shape anisotropy ($\propto M_s$) due to the out-of-plane phase softening is expressed through the $\vec{q}_{\|}$-dependent negative contribution to the in-plane anisotropy $\mu_0 M_s$. Naturally, increasing the film thickness d also decreases the in-plane shape anisotropy due to the increased softening from stray fields associated with larger magnetic moments. In the limit situation of very large $q_{\|}d$, the in-plane shape anisotropy is effectively lifted by the softening action of the spin waves and the spins behave as if they precess freely in a field $\vec{H}_{app}$ with no restoring forces, with a frequency given by

$$f_{MSBVW, q_{\|}d>>1} = \frac{\gamma\mu_0}{2\pi}H_{app}. \tag{2-34}$$

For $\vec{q}_{\|} = 0$, the MSBVW frequency coincides with that of the MSSW mode, which is discussed in Section 2.4.2.3. Note that the negative dispersion continues until the exchange-dominated regime is entered. For large $\vec{q}_{\|}$, the exchange interaction has to

be included in the dispersion relation, which then assumes an additional quadratic dependence in $\vec{q}_{\parallel}$, following from the the Herring-Kittel equation [40] as

$$f_{MSBVW+A} = \frac{\gamma\mu_0}{2\pi}\sqrt{\left(H_{app} + \frac{2A}{M_S}q_{\parallel}^2\right)\left(H_{app} + \frac{2A}{M_S}q_{\parallel}^2 + M_s\frac{1-e^{-q_{\parallel}d}}{q_{\parallel}d}\right)}. \quad (2\text{-}35)$$

2.4.2.2. *Magnetostatic Forward Volume Wave*

In the MSFVW dipolar mode geometry, the thin film is saturated in the out-of-plane $\hat{z}$-direction ($\vec{B}_0 = B_0 \cdot \hat{z}$) and spin waves are characterized by an in-plane wave vector $\vec{q}_{\parallel}$ which is chosen in the positive $\hat{x}$-direction. These spin waves are characterized by deviations of the magnetic moments from the equilibrium $\hat{z}$-direction (provided the thin film is fully saturated out-of-plane) which can be decomposed in an in-plane anti-aligned ($\hat{x}$) and an in-plane shear ($\hat{y}$) phase, as illustrated in Figure 2-18.

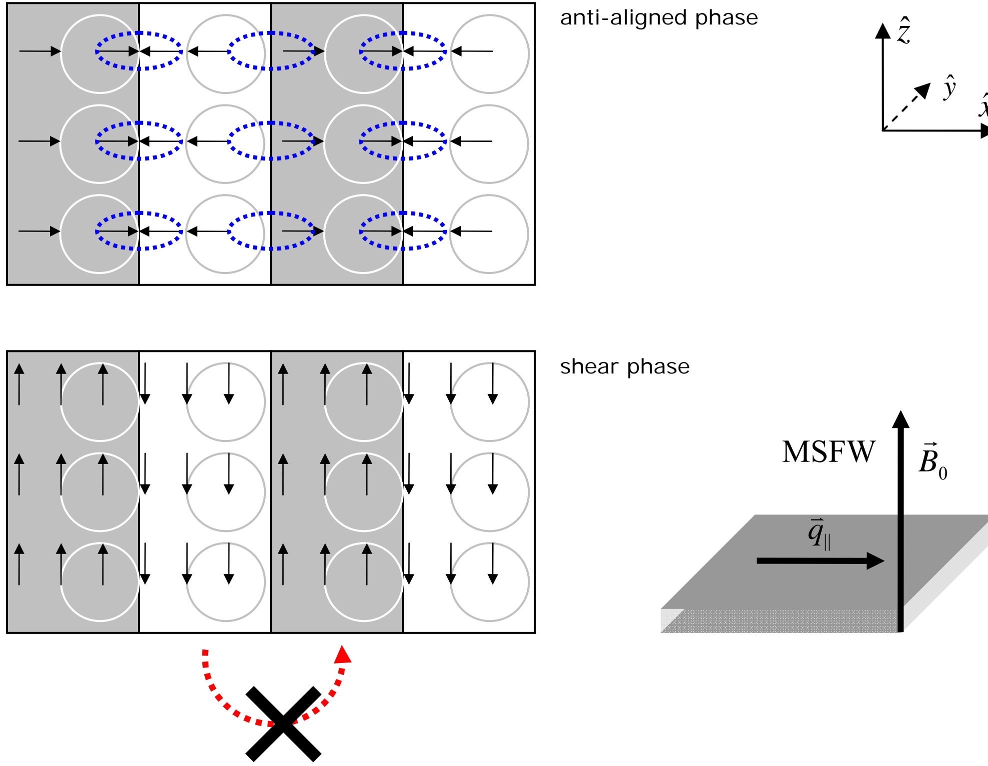

Figure 2-18: In the MSFVW magnetostatic mode geometry, the deviations of the magnetic moments from their equilibrium z-direction can be decomposed in an in-plane anti-aligned and an in-plane shear phase. In the in-plane anti-aligned phase, the dipolar stray fields from neighboring volumes of magnetic moment lead to mode hardening, whereas no stray fields are present in the in-plane shear phase, due to the infinitely extending thin film.

The in-plane shear phase is analogous to the MSBVW in-plane phase discussed in the previous section, in that no resulting stray fields act on the $\hat{y}$-direction dipole deviations from the equilibrium $\hat{z}$-direction. During the in-plane anti-aligned phase, however, a $\vec{q}_{\|}$-dependent stray field acts on adjacent dipoles, which in this case leads to mode stiffening, with the dipoles being pushed back towards their equilibrium out-of-plane orientations. In the limit situation of very large $q_{\|}d$, the only effective anisotropy the system experiences is that due to the out-of-plane bias field, and the MSFVW mode frequency is given by the Kittel formula [41]

$$f_{MSFVW, q_{\|}d>>1} = \frac{\gamma\mu_0}{2\pi}\sqrt{H_{app}\left(H_{app} + M_s\right)}. \tag{2-36}$$

Although the MSFVW mode will not be used explicitly in the remainder of this text, it was introduced here for the sake of completeness and to gain a full understanding of the behavior of the modes, based on the occurring dipolar stray fields.

2.4.2.3. Magnetostatic Surface Wave

In the MSSW dipolar mode geometry, the thin film is saturated in the in-plane $\hat{y}$-direction ($\vec{B}_0 = B_0 \cdot \hat{y}$) and spin waves have their in-plane wave vector $\vec{q}_{\|}$ in the $\hat{x}$-direction. These spin waves are characterized by deviations of the magnetic moments from their equilibrium $\hat{y}$-direction which can be decomposed in an out-of-plane ($\hat{z}$) and an in-plane anti-aligned ($\hat{y}$) phase, as illustrated in Figure 2-19.

The MSSW mode can be regarded as a combination of the MSBVW and MSFVW modes considering the mode softening in the out-of-plane phase and hardening in the in-plane, anti-aligned phase. When only dipolar interactions are considered, the dispersion relation for the MSSW mode (also known as the Damon-Eshbach mode) reads (equation (11) from [20] or [42])

$$f_{MSSW} = f_{DE} = \frac{\gamma\mu_0}{2\pi}\sqrt{H_{app}\left(H_{app} + M_S\right) + \left(\frac{M_S}{2}\right)^2\left(1 - e^{-2q_{\|}d}\right)}. \tag{2-37}$$

The resulting dispersion of the MSSW modes is positive, due to the mode hardening being the most important contribution.

Combining the dipolar and exchange contributions in a single expression for the dipolar-exchange modes, which display a hybrid dipolar and exchange dominated character, results in

$$f_{MSSW+A} = \frac{\gamma\mu_0}{2\pi}\sqrt{\left(H_{Eff} + \frac{2A}{M_S}q_{\|}^2\right)\left(H_{Eff} + \frac{2A}{M_S}q_{\|}^2 + M_S\right) + \left(\frac{M_S}{2}\right)^2\left(1 - e^{-2q_{\|}d}\right)}. \qquad (2\text{-}38)$$

In conclusion, the dispersion relations for the MSBVW, MSFVW and MSSW magnetostatic modes have been introduced and intuitively explained. The resulting mathematical expressions for the dispersion relations will be applied in the sections that consider the micro-magnetic modeling of these modes and in the discussion of the results of the optical BLS experiments.

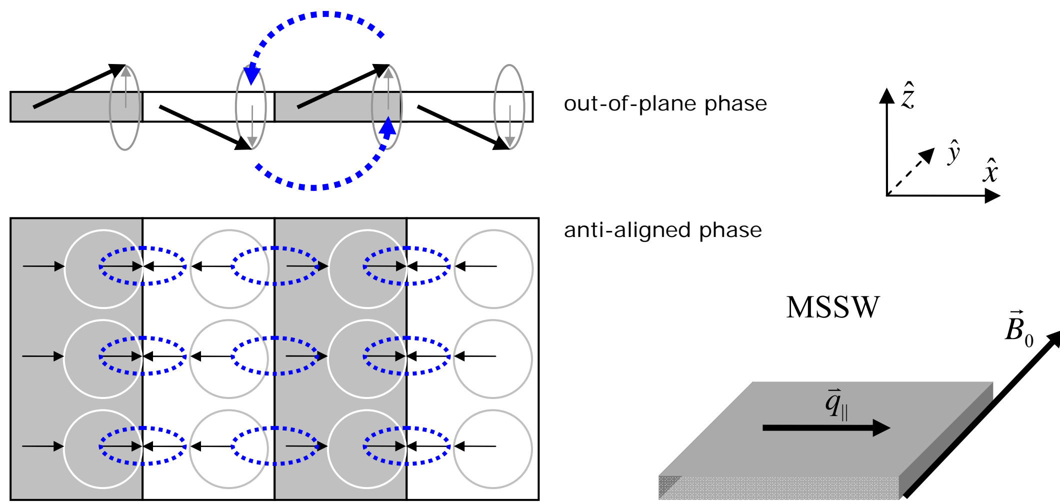

Figure 2-19: In the MSSW dipolar mode geometry, the deviations of the magnetic moments from their equilibrium y-direction can be decomposed in an out-of-plane and an in-plane anti-aligned phase. In the out-of-plane phase, the dipolar stray fields from neighboring volumes of magnetic moment lead to mode softening, whereas in the in-plane anti-aligned phase, the dipolar stray fields from neighboring volumes of magnetic moment induce mode hardening. The resulting dispersion of the MSSW modes is positive, due to the mode hardening being the most important contribution.

3. Experimental Techniques

The various experimental techniques that will find their specific application in the fabrication and characterization of point contact nano-oscillator devices are introduced in this section. First, the deposition process for both metallic and insulating thin films is explained, along with the various techniques available for patterning them. These patterning techniques consist of a combination of either optical or electron-beam lithography with a material removal process such as lift-off, ion-milling or chemical wet etching. Secondly, the measurement setups used to characterize fabricated devices are introduced. Scanning electron microscopy, atomic force microscopy, surface profilometry and ellipsometry are used to study the physical aspects of the fabricated devices, whereas four-probe resistance and magnetoresistance measurements, microwave RF measurements and Brillouin light scattering measurements assist in the assessment of device functionality in Section 5.

3.1. Sputter Deposition

3.1.1. The Sputtering Process

Sputter deposition is a commonly used vacuum technique for the manufacturing of thin films. As opposed to evaporation, sputtering can be performed within a lower quality vacuum and generally features both higher deposition rates and improved material adhesive properties with respect to a substrate. While DC 'diode' sputtering is suited for the deposition of conducting materials, insulating materials such as SiO_2 are deposited using an RF sputtering technique. Additionally, DC or RF 'magnetron' sputtering is an adapted form of the DC or RF sputtering technique in which a magnetic field assists in the sputter action. Figure 3-1 illustrates the general working principle of a DC sputtering system: an inert gas, often argon, is injected into a vacuum system that contains a piece of the material to be deposited, called the *target*. A large voltage between this target (acting as an anode) and ground (the cathode) generates a sustained plasma of positively charged argon ions and negatively charged electrons. The argon ions from the plasma strike against the target and are able to remove, i.e. 'sputter' material from it. The removed atoms or molecules redeposit on any substrate present in the system. The chamber walls, the chimney that directs the sputtered particle stream (not shown in the figure), sample and metallic ring close to the target are grounded. In some systems, application of an additional negative or positive voltage to the substrate holder may shield the substrate from electrons or particular ions from target or plasma. The deposition of neutral atoms is thereby left unaffected. The target and plasma are separated from the substrate by a shutter that opens during deposition. Usually, the target is shortly pre-sputtered before the actual

deposition is started to prevent oxidized or contaminated material to be deposited on the substrate.

From the preceding description of the sputtering process it becomes clear that the DC sputtering technique is incompatible with targets made of an insulating material. Positive charge buildup due to the positive argon ions would shield the target from the other argon ions in the plasma and prevent further sputtering. Therefore, when insulating materials are to be deposited, an alternating voltage is applied between the substrate and target. In the phase where the target is negative, material is sputtered, while in the positive phase, the heavy argon ions are repelled and plasma electrons compensate the positive charge on the target. This technique, generally known as RF sputtering, is commonly used for the deposition of insulating SiO_2 passivation layers.

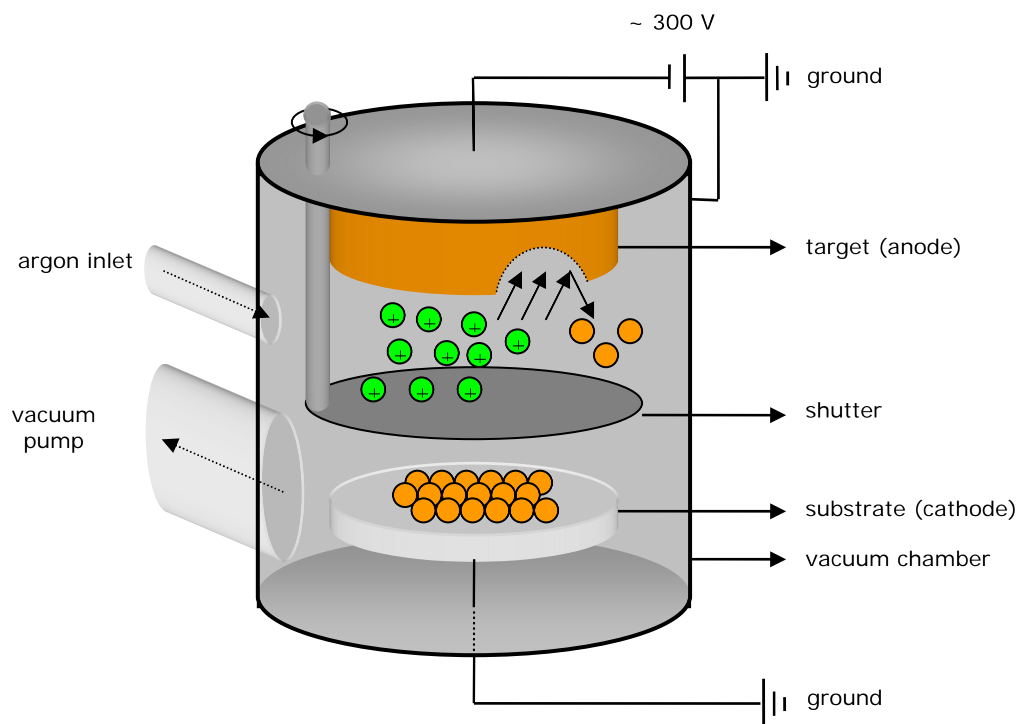

Figure 3-1: Schematic overview of the sputtering process. Within a vacuum chamber, positively charged argon ions strike against a target and release, i.e. ‘sputter’ atoms or molecules of the target material. When the shutter is opened, sputtered material can deposit onto a substrate. Target and substrate bias voltages are also shown.

Both of the sputtering techniques described above can be expanded with ring magnets that are placed below the target as to create a magnetic field trap that confines the plasma to a smaller region in space. In general, greater plasma densities are achieved, and the sputter yield is increased. As a disadvantage, the target material is non-

uniformly eroded (rings occur on the target disc), which effectively decreases the target lifetime. This is depicted in Figure 3-2.

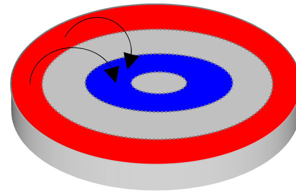

Figure 3-2: In DC or RF magnetron sputtering, ring magnets confine the argon plasma to smaller regions in space, increasing the sputter efficiency. A side effect is the formation of erosion rings in the target, which decreases the target lifetime.

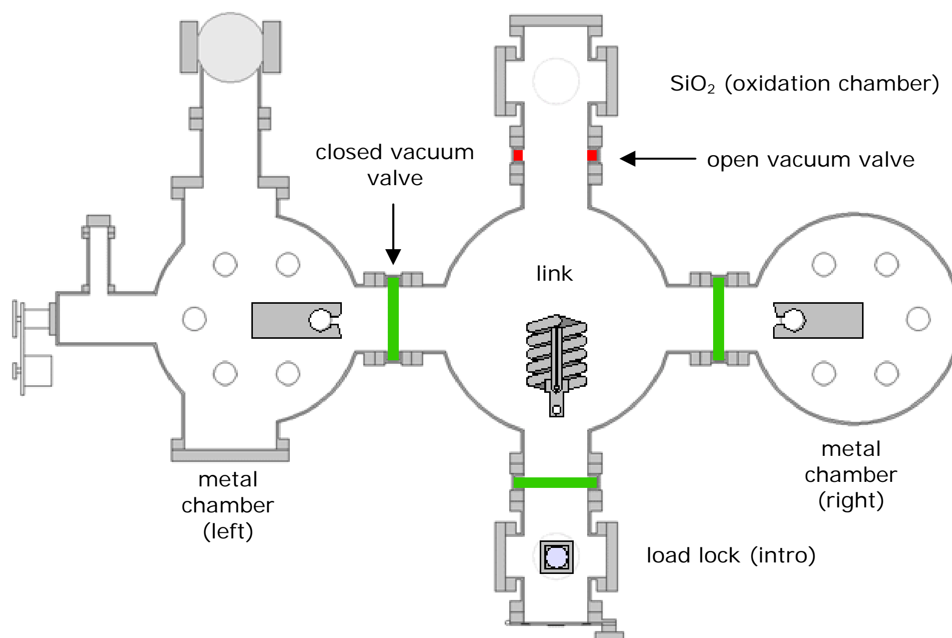

Figure 3-3: Schematic top view of the sputter system, showing the two metal chambers at the left and right, along with the oxidation / oxide sputtering chamber on top. The chambers are mutually connected through a link chamber. The additional chamber at the bottom serves as a load lock for convenient sample entry into the system. The entire system is automated and computer controlled.

3.1.2. The Sputtering System

Figure 3-3 presents a schematic top view of the sputter system used at IMEC for the deposition of thin film layers. The sputter system features three separate sputtering chambers, which are mutually connected through a link chamber. The link chamber is provided with a load lock for convenient sample entry. The system can be configured with a variety of targets, depending on the materials that are required for device

fabrication. At the time of writing, the left chamber featured Cu, Al, Ta, IrMn, Py ($Ni_{80}Fe_{20}$) and $Co_{90}Fe_{10}$, while the right chamber was equipped with Pt, CoFeB, Mg, Ru, GdFe and $Co_{50}Fe_{50}$ targets. The insulating SiO_2 layer is RF sputtered in the top chamber from a pure SiO_2 target, mechanically pressed against a Cu backing. The vacuum pressures in the chambers are monitored by ion gauges. The entire system is automated and computer controlled, so that complicated layer sequences can be sputtered automatically and under remote supervision.

3.2. Microstructure Patterning

The sputtering technique described in the preceding section produces a uniform thin film over the area of a substrate. This section discusses how this thin film is patterned into microstructures that will be further processed towards functional devices. Patterning of micrometer size structures generally involves two main steps: the definition of the structures on a substrate coated with a resist layer is followed by a process that transfers the pattern to the thin film by removing the material around the defined structures. While micrometer size structures can be manufactured with standard optical lithography techniques, nanometer scale features impose more stringent constraints on resolution and alignment precision, necessitating the use of more costly and time-consuming electron-beam lithography. First, the optical lithography and electron-beam lithography techniques are introduced for both a negative and positive resist system. Secondly, the material removal processes for structure patterning are discussed, which include lift-off, ion-milling and chemical wet etching. Specific choices between equivalent techniques for the various fabrication steps are accounted for in the discussion of the full fabrication workflow in Section 4.

3.2.1. Lithographic Pattern Definition

Micrometer size structures are usually defined by optical lithography. In this process, which is depicted in Figure 3-5-A, a photosensitive polymeric resist layer is spin-coated onto a substrate and subsequently illuminated through a mask design, so that the restricted areas that are to form the structures are exposed to light. Upon development of the resist layer, either the illuminated areas (positive resist) or dark areas (negative resist) are cleared from resist. After the mask design has been transferred to the substrate in the form of a resist mask, the patterning of the deposited multilayer stack is accomplished by lift-off, chemical wet etching or ion-milling, which are discussed separately in Section 3.2.2.

As indicated in Figure 3-4-A and B, current confinement to very narrow regions of a magnetic multilayer is realized by contacting the multilayer through a nanometer scale

hole, called a ‘point contact’, etched into an insulating SiO_2 layer. Commercially available optical lithography equipment is able to produce feature sizes with line widths well below 90 nm, while experimental limits up to 45 nm are obtainable. However, high-end, state-of-the-art, high-resolution (deep UV) optical lithography equipment is costly and features only limited flexibility in experimental optimization runs, where contact lithography is preferably used. Therefore, the nanometer scale dimensions of the point contacts exclude standard optical lithography, because of its resolution limits, as a viable option for the repeatable definition of these structures. Moreover, the definition of the nanometer scale electrode tip ends of the structures with optical access to the magnetic layer around the contact (Figure 3-4-B) requires greater alignment precision than can be obtained with manual alignment as used in the optical lithography process. This kind of high precision alignment is a prerequisite for obtaining a working device, since the slightest misalignment of the tips with respect to the underlying point contact will result in a faulty device. Therefore, the nanometer scale point contacts and top electrode tip ends are defined with high-resolution electron-beam lithography instead of conventional optical lithography.

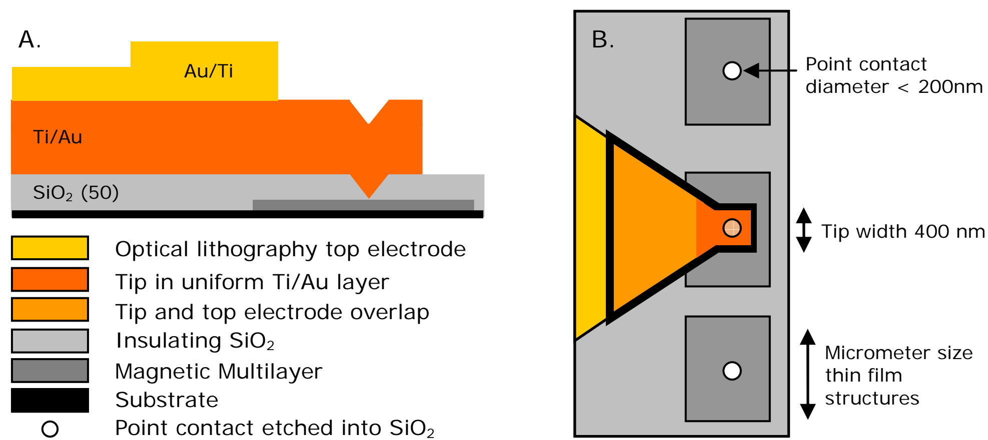

Figure 3-4: The definition of nanometer scale point contacts and their associated electrode tips requires high resolution and precise alignment, which is obtained through the use of e-beam lithographic patterning. The magnetic thin film elements and the main part of the top electrodes are defined with regular optical lithography. Note that a slight overlap exists between the electrode tip and the main part of the top electrode.

With electron-beam lithography, a mask design is transferred to a resist layer through a direct writing technique: the substrate surface is scanned with a focused electron-beam in a pixel-by-pixel manner. For a constant intensity electron-beam, the amount of time a single pixel is illuminated determines the *dose* of the exposure, expressed as the amount of charge delivered per square area [C/cm^2]. Due to the scanning nature of e-beam lithography, pattern definition is a rather slow and costly process, which is

why it is only employed for the definition of the critical features in the design. However, this drawback is made up for by the greater flexibility concerning new mask designs and by the increased resolution and alignment properties compared to the optical lithography technique discussed earlier. Both optical and e-beam lithography have to be combined with a thin film removal process for the multilayer material around the transferred design, which is the topic of the next section.

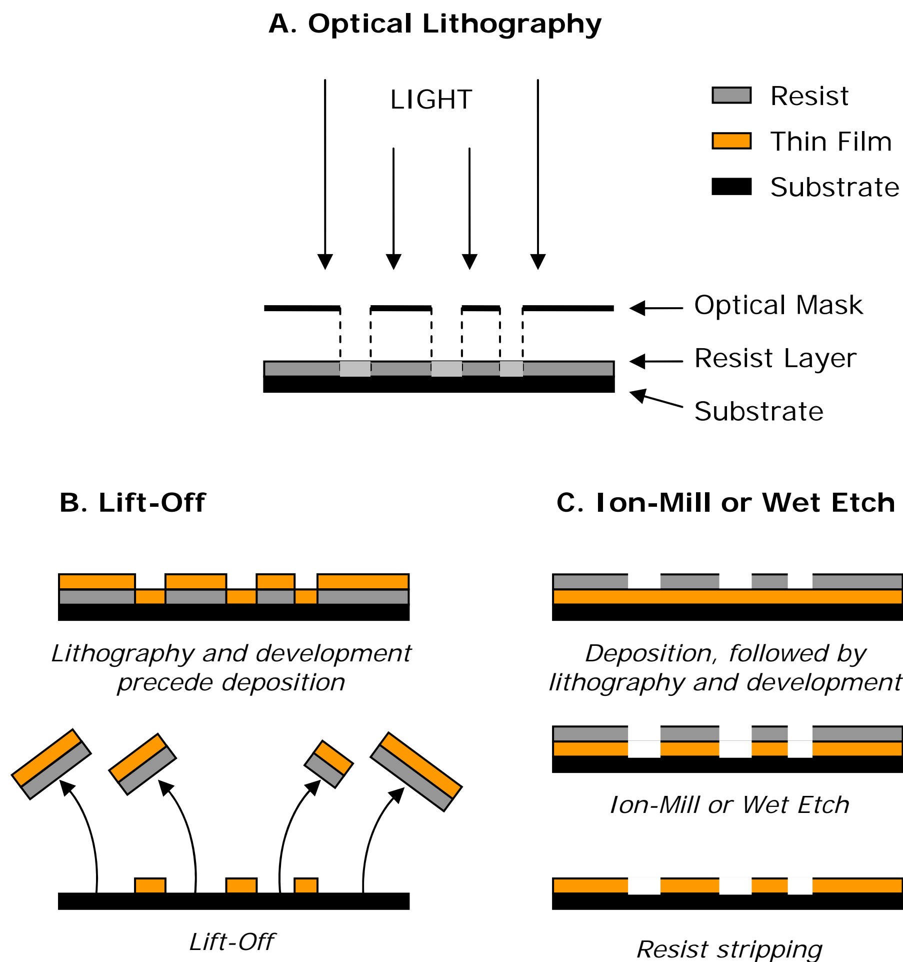

Figure 3-5: Schematic illustration of the lithographic patterning process (A), lift-off (B) and (dry or wet) etching (C). In case of lift-off (B), the thin film is deposited after the pattern has been defined, while in case of ion-milling or wet etching (C), the deposition of the material precedes the lithographic patterning process.

3.2.2. Pattern Transfer

3.2.2.1. Lift-Off

In the lift-off approach to patterning (Figure 3-5-B), a mask design is transferred to a substrate in the form of a resist pattern, before the deposition of the thin film layer. After material has been sputtered uniformly over the substrate, the wafer is immersed

in a substance that dissolves the resist layer underneath parts of the deposited layer. The lift-off process derives its name from the fact that it lifts these parts of material off the sample, while the designed structures are left intact. The result is a substrate that carries a series of rectangular thin film strips that will be further processed towards point contact nano-oscillators. Compared with the ion-milling technique that is to be discussed next, the lift-off process offers the advantage that no depth control is needed: the etch depth is exactly the thickness of the deposited film, i.e. all material is removed. On the other hand, the maximum layer thickness that can sustain lift-off is limited by the thickness of the resist layer and compared with shorter wavelength (e-beam) lithography the resolution is also limited. Moreover, lift-off of thicker films often results in badly defined edges which may pose difficulties in subsequent processing steps.

3.2.2.2. Ion-Milling and Wet Etching

Ion-milling is a non-selective physical process for material removal which is greatly analogous to the sputtering process described in Section 3.1.1. Within a vacuum, energetic xenon ions from a plasma are accelerated towards a target, in this case the substrate itself, and remove material in the developed resist areas. For a constant intensity beam of ions, the milling depth is controlled by the amount of time the sample is being bombarded by the ions. Note that unlike the case of a lift-off approach (Figure 3-5-B), where the lithographic step precedes the deposition of material, the ion-mill approach (Figure 3-5-C) requires the lithographic step to be performed after deposition of the magnetic stack. The same holds for the wet etching procedure that relies on the action of a chemical etching agent to remove sputtered material in the developed areas of the transferred resist pattern.

3.3. Microstructure Characterization

Dektak surface profilometry, scanning electron microscopy (SEM), atomic force microscopy (AFM) and ellipsometry are four techniques commonly used to assess the size, morphology and surface topology of microstructure devices. These techniques will find their use in the characterization of fabricated devices in Section 5 and are therefore shortly introduced in the following sections.

3.3.1. Dektak Surface Profilometry

Dektak surface profilometry is a method for assessing surface roughness or step height across devices on a substrate. A stylus in contact with the substrate scans along a straight line while the vertical stylus movement is being recorded and visualized. The assessment of step heights is performed on a set of specific test structures

especially incorporated in between fabricated devices. When assessing step heights, the values are usually averaged over a set of scanned structures. Depending on the scan speed and step height, the typical vertical resolution in an averaged measurement is 5 nm.

While Dektak surface profilometry provides a relatively fast and accurate method for acquiring information about the surface topology of a sample (albeit only in a single direction), determining the thickness of a generic thin film implies the need for lithographic patterning of the required test structures. Section 3.3.4 discusses an alternate method for acquiring layer thickness information through an optical measurement which does not require layer patterning.

3.3.2. Scanning Electron Microscopy

Scanning electron microscopy (SEM) imaging relies on the collection of secondary (low energy) or backscattered (high energy) electrons resulting from the exposure of a sample to a focused, high energy electron beam. The electrons in this high energy beam are usually generated through thermally assisted field emission from a tungsten or LaB_6 filament and are subsequently accelerated by an electric potential and focused onto the sample by magnetic lenses. The scanning nature of SEM is expressed in the beam being deflected by sets of magnetic coils and enables scanning of a square area. SEM delivers high resolution (1 to 5 nm) images that can be used to assess surface morphology and nanometer scale features present on a device, such as the point contacts that will be etched into an insulating SiO_2 layer.

3.3.3. Atomic Force Microscopy

Atomic force microscopy (AFM) is a scanning-probe technique capable of imaging the surface topology of a substrate with the tip of a micrometer scale cantilever as shown in Figure 3-6. Interaction of the tip with the surface leads to a deflection of the cantilever which can be recorded with the use of laser optics. Possible interaction mechanisms between tip and substrate surface include mechanical contact force, Van der Waals forces, capillary forces, chemical bonding forces, electrostatic forces, magnetic forces (exploited in the MFM variant of AFM) and Casimir forces. Instead of moving the tip to scan the substrate surface, the substrate itself is fitted on a piezo-electric scan stage that moves the sample underneath the tip.

A typical AFM scanner can operate in a number of different modes, such as a static (contact) mode and a dynamic (tapping) mode. In the static mode, the interaction of the cantilever tip with the sample is directly recorded through the absolute movement of the tip induced by the substrate topology. In tapping mode, the cantilever tip is

made to oscillate at or near its eigen-frequency. The force acting on the tip can then be deduced from the change in swing amplitude or frequency. AFM offers some specific advantages over SEM, such as sub-nanometer depth resolution (it is in fact a three-dimensional technique) while it does not require a vacuum. On the other hand, an AFM scan of an extended area proceeds slowly and may suffer from associated (thermal) drift. Moreover, in some instances, hysteresis effects occurring in the piezo-electric scanning stage can induce artifacts in the measurements.

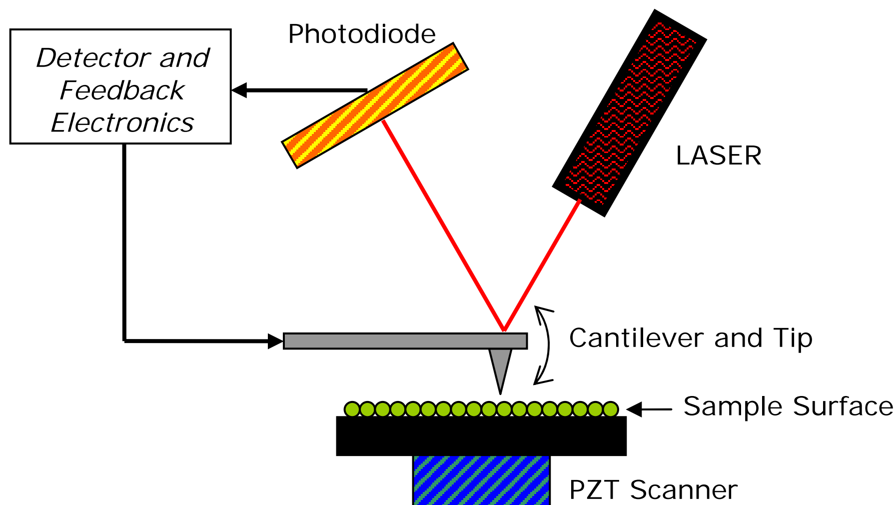

Figure 3-6: Simplified overview of an atomic force microscope. A substrate is fitted on a piezo-electric scanning stage so that a micrometer scale cantilever tip can scan the sample surface. The interaction of the cantilever tip with the surface results in a movement of the cantilever, which is recorded using a laser beam and a photodiode.

3.3.4. Ellipsometry

When linearly polarized light reflects from a thin film surface, its polarization changes and becomes elliptic. The induced ellipticity reflects the optical properties of the material being probed. By measuring the ratio of the reflected intensities of plane polarized incident light along with the occurring phase differences, optical constants (refractive index and extinction coefficient) can be extracted. Moreover, the thickness of the layer can be estimated through an iterative regression fitting procedure of the data according to a model based on assumed values of the physical material parameters. This is usually performed through a Levenberg-Marquardt procedure that adjusts the model parameters until an acceptable fit with the recorded data is achieved, after which the model delivers the quantities of interest, such as film

thickness and refractive index. For accurate fitting, the exact optical properties of the substrate and deposited layers are extracted from detailed libraries of material constants.

An interesting application of ellipsometry is found in the calibration of the sputter rates for SiO_2. Although the thickness of the SiO_2 layer can be calibrated in various other ways (e.g. through a selective buffered HF wet etch that stops on a platinum sub-layer or a lift-off procedure in combination with a lithographic mask), an ellipsometric measurement can provide, in addition to the layer thickness, complementary physical parameters such as the refractive index and index of extinction (together making up the complex refractive index) of the material. When they are compared with known values of completely stoichiometric SiO_2, the obtained values give an indication of the quality of the oxide, making ellipsometry an interesting method to assess both the quality and thickness of uniform layers of SiO_2. For example, an increased refractive index may indicate larger absorption, relating to inferior quality of the SiO_2 layer.

3.4. Measurement Setups

3.4.1. Four-Probe Resistance Measurement Setup

Since lead and contact resistances can contribute considerable error to resistance measurements of low-resistance devices such as point contact nano-oscillators, the resistances of these devices are preferably determined by means of a four-probe technique, rather than by standard two-wire sensing. As its name suggests, the four-probe technique uses four electrical terminals to determine device resistance, in a configuration that eliminates any lead, contact and spreading resistances. This results in a more precise reading of the resistance of the actual device.

Dedicated four-probe measurement equipment is available in the form of a source-meter, providing both a current source and a voltmeter in a single four-terminal device. As indicated in the equivalent circuit for a four-probe resistance measurement as depicted in Figure 3-8, two of the four probes are used to send current through the device under test (DUT), while the remaining two probe the voltage over the device. In this setup, negligible current flows through the voltage probes and leads, effectively reducing their resistance contribution to the total resistance measured. The resistance of the device under test is then determined through Ohm’s law by dividing the measured voltage (from the voltage probes) by the supplied current (from the current probes). The obtained resistance reading represents a more accurate figure of the device resistance compared to that generated by conventional two-wire sensing, which also records lead resistances.

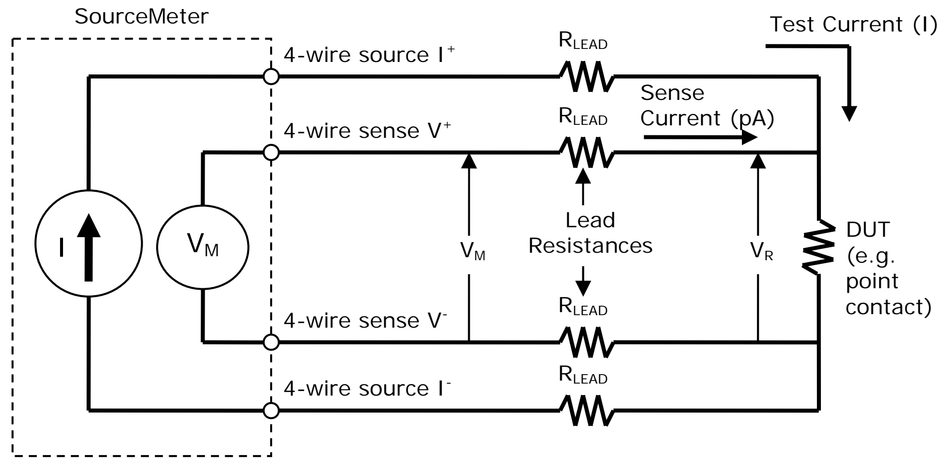

Figure 3-7: In a four-probe resistance measurement, negligible current flows through the leads of the voltage probes, effectively minimizing or eliminating errors on the resistance measurement due to lead, spreading and contact resistance of the probes. I represents the current sourced by the source-meter, V_M the voltage measured across the source-meter and V_R the voltage across the resistive device (e.g. a point contact). Because the sense current is negligible, $V_M = V_R$ and the measured resistance is $V_M/I=V_R/I$.

Contacting of the point contact devices with top electrodes in a cross geometry (see Figure 3-8) is especially well suited for performing four-probe electrical measurements, as it allows for the consistent and easy placement of voltage and current probes on the provided landing pads.

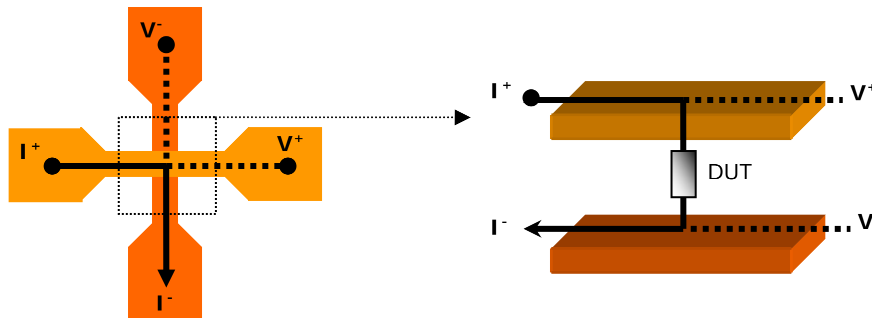

Figure 3-8: Within the four-probe cross contacting geometry, the device (i.e. the point contact) is connected to four electrical terminals. Two of them are used to send current through the device (the thick line indicates the current path), whilst the other two measure the voltage across the device (dashed line). Since negligible current flows through the voltage probes, lead, contact and spreading resistances are effectively eliminated, leading to a more accurate reading of the device resistance as compared to a regular two-probe measurement.

3.4.2. Magnetoresistance Measurement Setup

For the determination of magnetoresistance curves (resistance curves as a function of externally applied field), a sample is fitted between the poles of two electromagnets as indicated in Figure 3-9. The magnitude of the generated magnetic field is controlled by varying the current through the coils with a programmable current source (PCS) which allows for field sweeps between roughly -0.2 T and 0.2 T.

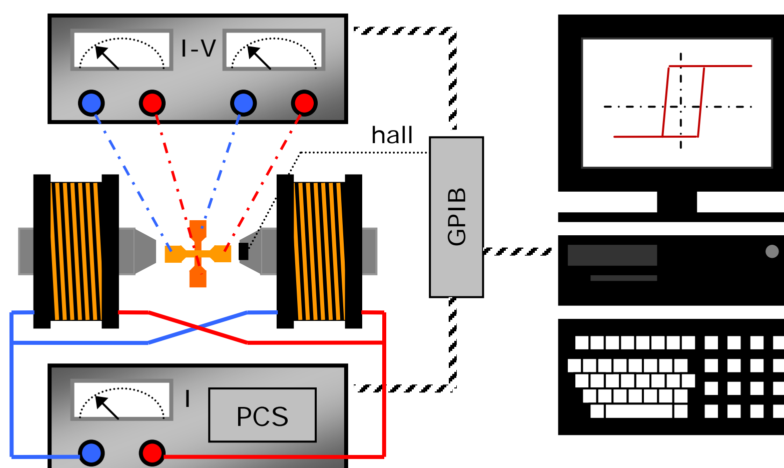

Figure 3-9: Schematic overview of the setup used to determine MxH loops for a magnetic structure. The device is fitted between the poles of two electromagnets, which are driven by a programmable current source (PCS). The magnetic field strength is monitored by a Hall sensor fitted on one of the poles. The device under test is connected to a source-meter to enable four-probe resistance measurements. The process is automated by a PC that controls all the measurement units through a GPIB interface. Parameters such as sweep rate, field offset, settle and integration times can be set within the software environment.

The field is monitored with a hall sensor that is mounted between the poles of the electromagnets. The sample is connected to a source-meter (current source and voltage meter in a single device) by four electrical probes, enabling four-probe resistance measurements as described in Section 3.4.1. All components of the measurement setup are connected to a personal computer through a GPIB interface. Automated sweeps of the external field can be performed from within a software environment that records the change in device resistance. The field ramp rate, measurement settle and integration times as well as field offset calibration parameters can be set in the program. Recorded magnetoresistance curves as a function of externally applied field can be saved to disk for later analysis.

3.4.3. Microwave Measurement Setup

The microwave measurement setup used to assess RF emission from point contact devices shares various electrical and magnetic components with the magnetoresistance setup that was described in the previous section. Devices to be assessed in this setup are designed with 50 Ω impedance-matched coplanar waveguide (CPW) electrodes that allow connection through the placement of dedicated RF pico-probes (instead of the former four-probe connection) on the waveguide strips (see Section 4 for further details). A general overview of this setup is given in Figure 3-10.

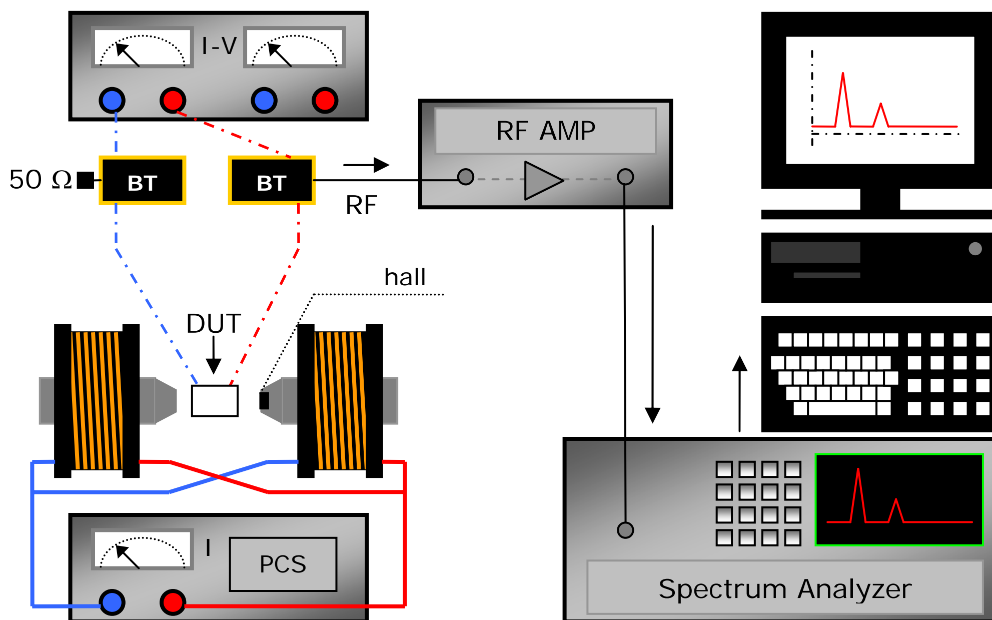

Figure 3-10: Overview of the microwave RF setup used to measure RF emission on point contact nano-oscillator devices. This setup shares many of its components with the four-probe magnetoresistance setup shown in Figure 3-9. The four-probe electrical connections to the DUT are now replaced by pico-probes, contacting the sample through RF CPW top electrodes. Current is sent into the DUT through a bias tee (BT) whose RF side is terminated with a 50 Ω resistor. Current is drawn back into the current source through a second bias tee that separates any RF signal generated by the DUT. The RF signal passes through a double amplification stage before entering the spectrum analyzer. A computer controls all the components and allows for automated measurements for varying current and magnetic field.

Current is injected into the device through a bias tee whose RF connection is terminated with a 50 Ω load. Alternatively, this connection can be used to inject a microwave current into the sample for performing RF-excited experiments. The microwave signal generated by the device under test is extracted from the RF side of a second bias tee, placed in the current path after the device, and runs through a cascaded dual microwave amplification stage before entering the RF spectrum

analyzer. Again, the programmable current source that controls the external field, the source-meter providing DC current to the sample, the hall sensor and the RF spectrum analyzer are handled through a computer interface that allows for the automated measurement of RF spectra as a function of external field and DC input current within user-defined frequency scanning ranges.

3.4.4. Brillouin Light Scattering Setup

Brillouin light scattering (BLS) is an optical spectral technique for probing the magnetization dynamics and spin wave emission in extended magnetic layers, based on the inelastic scattering of photons with magnons (spin waves) as illustrated in Figure 3-11. When monochromatic laser light focused onto a magnetic layer gets inelastically scattered by a magnon, it undergoes a frequency shift which can be related to the wave vector of the probed magnon through the laws of conservation of wave vector and energy. The BLS technique enables the investigation of emission of spin waves with wave vectors corresponding to those of the laser light used to probe the sample (GHz frequency range).

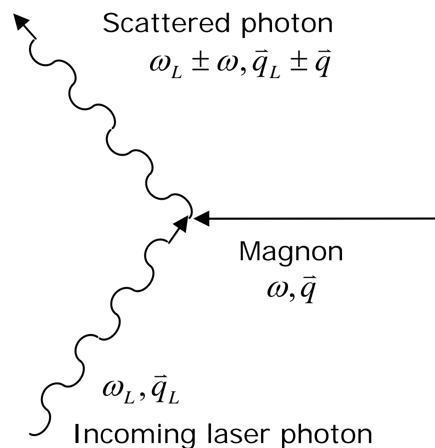

Figure 3-11: The photon-magnon Brillouin light scattering process is exploited in the BLS setup to probe the wave vectors and energies of spin waves in a magnetic layer.

The sample is investigated in a backscattering setup as indicated in Figure 3-12 and Figure 3-13, where a monochromatic laser beam probes the surface and the backscattered light is collected. The frequency spectrum of the backscattered light is then analyzed by guiding it through a multi-pass tandem Fabry-Perrot interferometer. The concept of using two Fabry-Perrot etalons in a Tandem configuration was first proposed by Sandercock [43]. Generally, the transmission spectrum of a single etalon features peaks at well-defined frequencies corresponding to the resonances of the etalon. By using two etalons tuned to transmit specific, but distinct frequency bands

(by using slightly different mirror spacings), unwanted orders in the frequency spectrum are filtered out. The etalons in the interferometer are controlled through piezo-stages that precisely adapt the mirror spacings in order to scan a chosen frequency spectrum. After passing through the interferometer, the light is detected by a single-photon avalanche photomultiplier. The Brillouin light scattering setup is extensively described in [44]. The optical BLS experiments in this thesis were carried out in collaboration with the University of Technology of Kaiserslautern, where a sophisticated scanning BLS setup is available, corresponding to the schematic overview given in Figure 3-12.

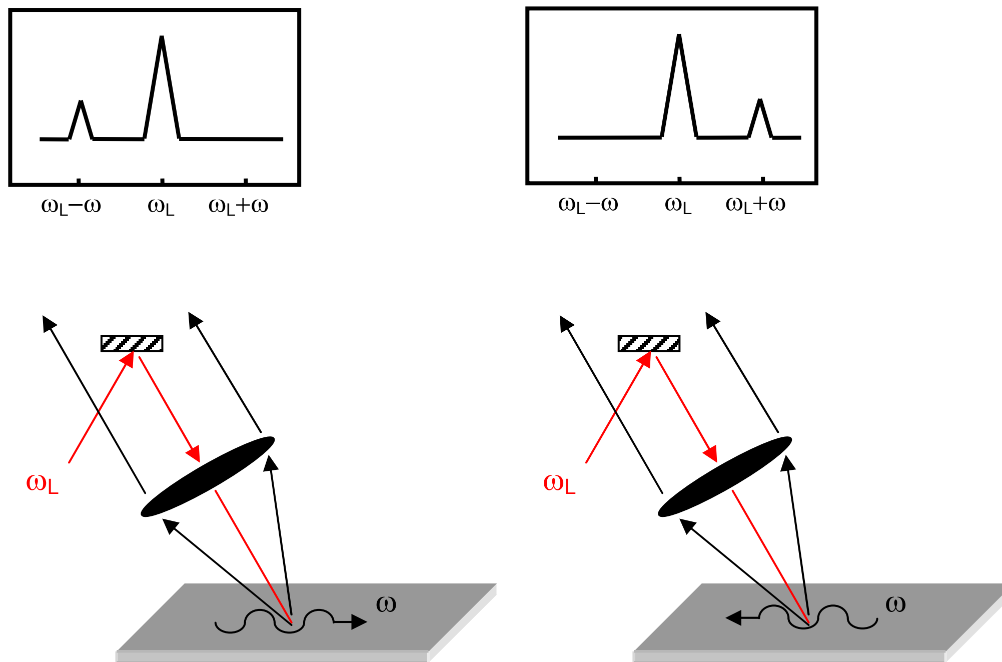

Figure 3-12: The BLS backscattering geometry. Laser light is focused on the surface of a sample, where it is inelastically scattered through interaction with a spin wave. The reflected light is collected through an objective and passed on to a multi-pass tandem Fabry-Perot interferometer where its frequency spectrum is analyzed. Depending on whether a spin wave is created or annihilated, the light can undergo either a frequency decrease (Stokes scattering) or increase (Anti-Stokes scattering).

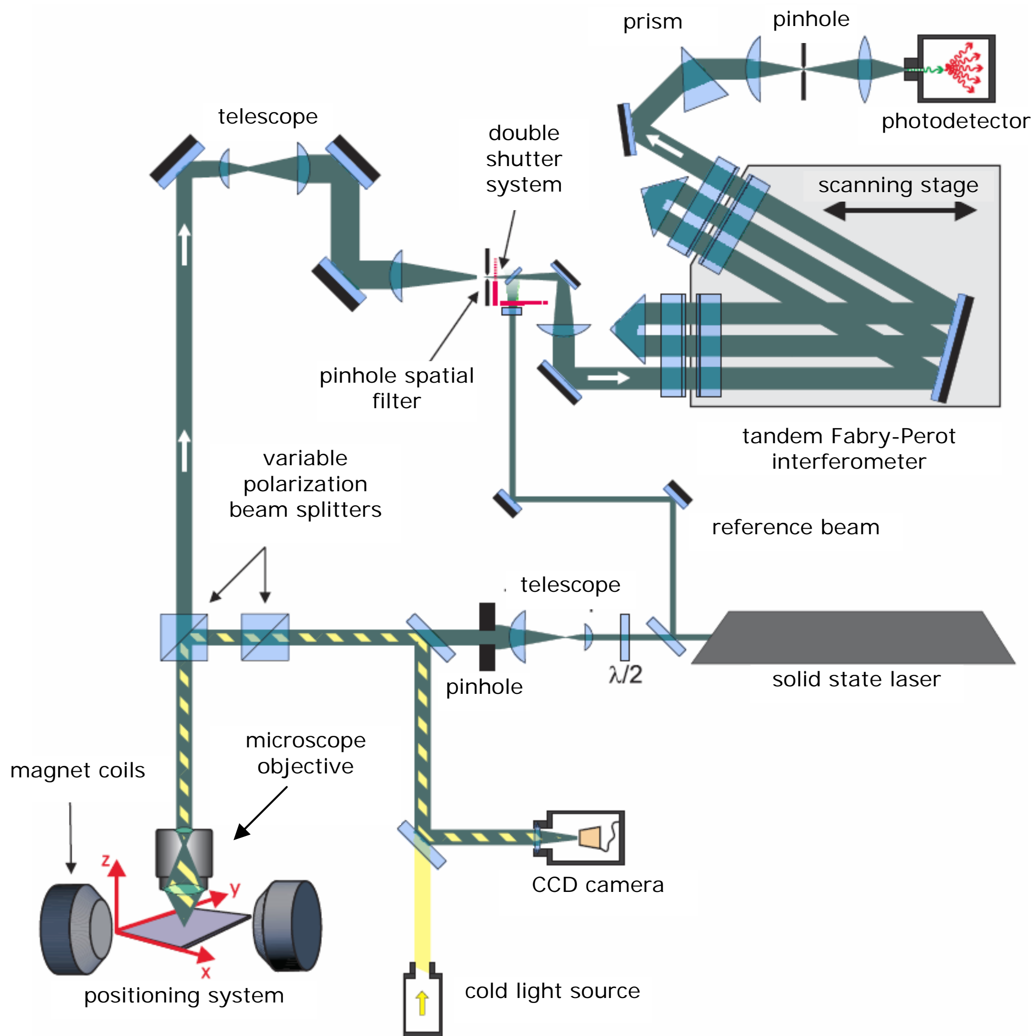

Figure 3-13: Schematic overview of the Brillouin light scattering setup, showing the solid state laser, sample, focusing optics and a six-pass tandem Fabry-Perot interferometer. Figure adapted from [45].

4. Device Fabrication

This section discusses the bottom-up fabrication of point contact nano-oscillator devices, following a step-by-step approach based on the methods outlined in Section 3. First, the various device designs to be fabricated are introduced. Section 4.1 then gives a general overview of the fabrication process, which is explored in even more detail in Section 4.2. The specific calibration procedure for the ion-mill etch rate of cured FOX12 is also presented to the interested reader in Section 4.3.

As stated in Section 1, the nano-oscillator devices under investigation in this thesis are fabricated in the *point contact geometry*: electrical contact to an extended magnetic layer is established through a nanometer scale hole in an insulating SiO_2 layer. The mask design features various test structures that are suited to the different kinds of measurements to be performed in Section 5. These structures differ mainly in the geometry of the top electrodes for contacting the point contact and underlying magnetic layer. The top electrode configurations include four-terminal cross geometry electrodes for precise four-probe resistance measurements (Figure 4-1-A), coplanar waveguide (CPW) impedance-matched RF electrodes for microwave experiments (Figure 4-1-B) and top electrodes that end in a very small tip above the point contacts (Figure 4-1-C), featuring optical access to a large part of the magnetic layer around the point contact, a requirement set by the aim to perform Brillouin light scattering experiments on these devices. Additionally, some symmetric double point contact CPW RF structures are implemented in the design (Figure 4-1-D), enabling future synchronization experiments, either spin torque driven or RF-excited.

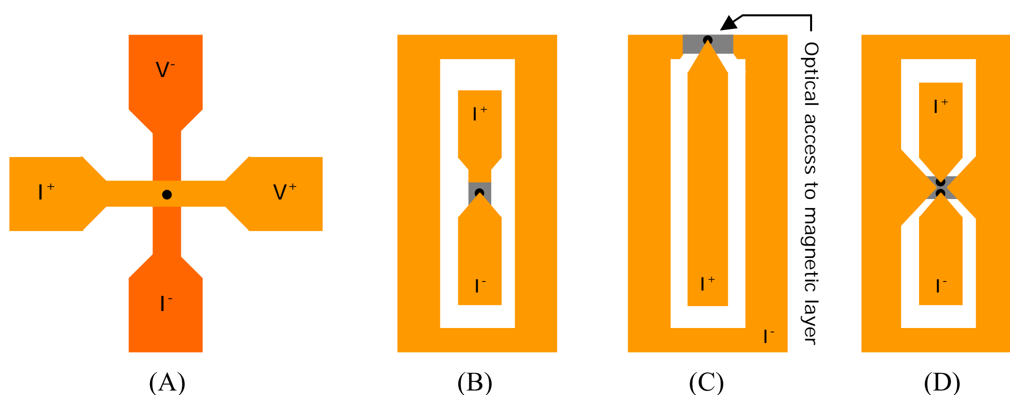

Figure 4-1: Top view of the top electrode geometries for the various test structures for electrical and optical characterization of nanometer scale point contacts. From left to right: four-probe electrodes (A), RF CPW electrodes (B), BLS device with optical access to the magnetic layer around the small electrode tip (C) and a symmetric, double point contact structure for synchronization experiments (D).

4.1. General Process Overview

Figure 4-2 gives a schematic side and top view of a small electrode tip on top of a point contact corresponding to the BLS device depicted in Figure 4-1-C. This detail of a device with optical access to the extended magnetic layer around the point contact will be used to explain the subsequent processing steps in the point contact fabrication workflow that is fully described in this section.

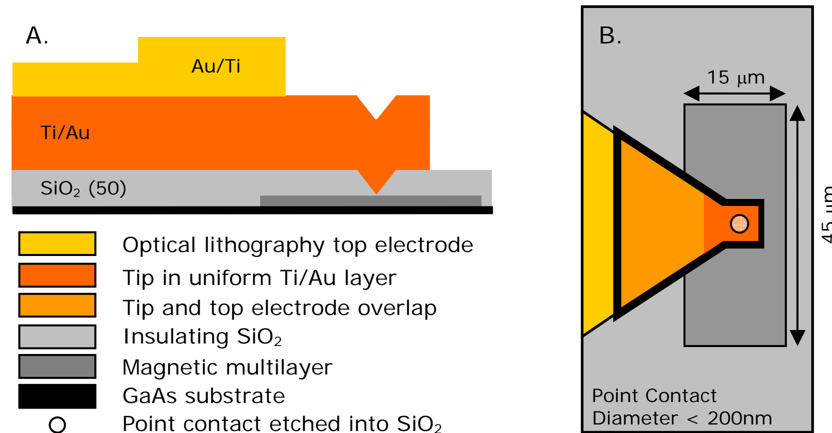

Figure 4-2: Schematic side and top view of a small electrode tip on top of a point contact, corresponding to the BLS device of Figure 4-1-C. Not that the dimensions in the drawing may not be proportional to those of the real device.

The full fabrication process flow is depicted schematically in Figure 4-3-A to I. In summary, a magnetic multilayer is deposited and patterned into rectangular microstructures which are covered with an insulating SiO_2 layer. Point contacts and side contacts (not shown in the images) are etched into the insulating layer, followed by the deposition of a uniform Au layer. The process continues with the definition of metallic top electrodes that provide electrical connections to the device. After the e-beam markers under the uniform Au layer have been cleared, the small tip at the end of the regular electrode is defined through an additional e-beam lithography step. A final ion-mill etching step removes the uniform Au layer between the devices except for the areas where the small tips have been defined. This outlines the general process workflow for the fabrication of point contact nano-oscillator devices. The details of each subsequent step are discussed in the next section, Section 4.2. Note that the process outlined above encompasses all the steps necessary to produce the BLS devices with optical access. In case only four-probe devices or RF devices are needed, the steps that were especially incorporated to obtain very small tips at the end of the regular electrodes can be omitted (steps D, F, G and H).

4.2. Detailed Process Workflow

The following paragraphs discuss the critical points in the point contact nano-oscillator fabrication process as outlined in the previous section. Schematic representations of the main process steps involved are provided in Figure 4-3-A to I, which act as a guide to the reader in following the detailed process workflow from start to end.

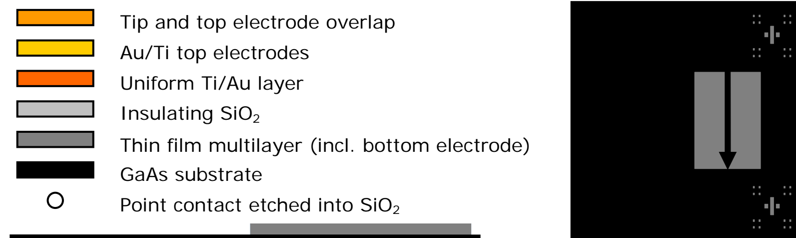

Figure 4-3-A: Sputter-deposition of the magnetic multi-layer onto a GaAs substrate and definition of rectangular microstructures by optical lithography in combination with either lift-off or ion-milling. The legend applies to all subsequent figures. The arrow indicates the exchange bias direction of the spin valve magnetic layer.

Figure 4-3-B: Passivation of the magnetic thin film elements. An intermediate Al(0.4) layer is deposited and plasma-oxidized, resulting in an Al_2O_3 adhesion layer for the subsequently sputtered SiO_2(50.0) layer.

Figure 4-3-C: The nanometer scale point contact is defined with e-beam lithography in a single PMMA resist layer and etched into the underlying SiO_2 layer using a buffered hydrofluoric acid solution (BHF) that selectively etches SiO_2. Etching stops on the underlying spin valve Pt capping layer.

Figure 4-3-D: Sputter-deposition of a uniform Ti(5.0)/Au(120.0) layer, covering the entire substrate.

Figure 4-3-E: The main parts of the top electrodes are defined with optical lithography and lift-off of a sputtered Au(120.0)/Ti(5.0) layer. Only the small BLS tip ends on top of the point contacts remain to be defined in a later stage.

Figure 4-3-F: Before the small tips can be defined with e-beam lithography, the e-beam markers that were deposited in the first step (together with the rectangular magnetic thin film elements) have to be cleared using optical lithography and a chemical Au etch.

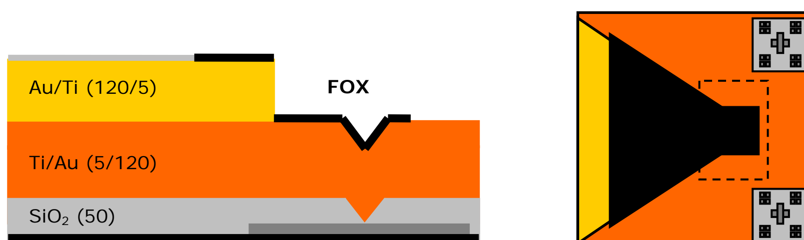

Figure 4-3-G: The small tips are defined in a FOX12 flowable oxide resist layer with e-beam lithography. The tips have a certain amount of overlap with the rest of the electrode that was defined in Figure 4-3-E, ensuring continuous electrical contact.

Figure 4-3-I: The tips in the cured FOX12 are transferred to the uniform Au layer by ion-milling. At the same time, the top electrodes already in place get milled as well. Inserting an additional hard buffer layer on top of the electrodes can provide thicker electrode thicknesses, as indicated by the dashed lines. The maximum thickness of the tip is obtained by stopping the ion-milling exactly when the SiO_2 layer underneath has been reached. Over-milling results in thin tips that are subject to easy destruction by high currents.

Figure 4-3-I: The final structure in side and top view. The small tips make contact with an extended magnetic layer through a nanometer scale point contact hole in the insulating SiO_2 layer. The current is effectively confined to a small area while the surrounding magnetic layer is accessible for optical measurements.

4.2.1. Point Contact Definition

Substrate preparation. The fabrication of point contact nano-oscillator devices starts with the creation of patterned microstructures of magnetic material on a substrate. Semi-insulating GaAs is chosen as a substrate because of its superior RF electrical properties compared with Si (e.g. reduced power leakage into substrate modes). This choice is based on the aim to perform extensive RF measurements on the fabricated devices, with frequencies extending well beyond the 10 GHz range. The substrate is submitted to an ultrasound-assisted acetone/IPA cleaning procedure before entering the vacuum deposition system.

Thin film deposition. A magnetic thin film multilayer is deposited by means of the DC sputtering process explained in Section 3.1 and subsequently patterned into rectangular thin film elements, as indicated in Figure 4-3-A. Note that the point contact nano-oscillator devices fabricated in this work are designed to function in a current perpendicular-to-plane (CPP) geometry as indicated in Figure 4-4. In this

geometry, current injected through a side contact at the left initially flows in the bottom electrode before reaching the top electrode through a small point contact etched in the insulating SiO_2 layer. This way, the current passes quasi-perpendicularly through the magnetic spin valve GMR stack in the area under the point contact. A suitable layer stack to achieve this strongly confined CPP geometry consists of at least four general parts: a metallic bottom electrode, a GMR multilayer, an insulating layer in which the point contact is etched and a metallic top electrode. The resulting layer stack is depicted in Figure 4-5.

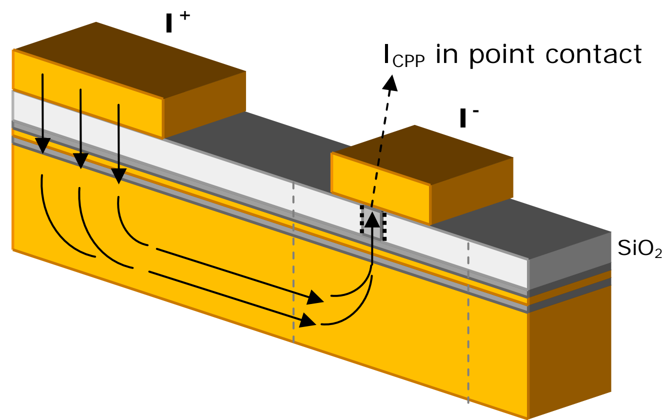

Figure 4-4: In the current-perpendicular-to-plane (CPP) geometry, current injected through a side contact at the left initially flows mainly in the bottom electrode before bending up towards the top electrode where it passes through a very small point contact hole etched in an insulating SiO_2 layer. This way, the current passes quasi-perpendicularly through the magnetic GMR stack in the area right under the point contact. An exploded view of the layer configuration in the area between the dashed lines is given in Figure 4-5.

The point contact spin torque nano-oscillator devices considered here are based on an exchange-biased, bottom-pinned spin valve stack, consisting of a fixed (bottom) and free (top) magnetic layer separated by a Cu spacer layer. Note that the insulating SiO_2 layer and top electrode are not yet deposited at this stage and will instead be introduced separately in a later paragraph. The exact composition of the thin film multilayer stack, including the approximate thicknesses of the individual layers, is now discussed.

The bottom electrode consists of alternating layers of sputtered tantalum and cupper (thickness in nm between brackets): Ta(3.5)/Cu(16.0)/Ta(3.5)/Cu(16.0)/Ta(3.5). The Ta seed layer is inserted to improve the texture of the sputtered cupper layer. Between the bottom electrode and the actual GMR spin valve stack, an additional Py(2.0) layer is inserted, providing a suitable base for growing the IrMn exchange biasing layer. The actual spin valve magnetic multilayer is subsequently deposited: the pinned

$IrMn(6.0)/(Co_{90}Fe_{10})(4.5)$ layer is separated from the free $(Co_{90}Fe_{10})(1.5)/Py(2.0)$ layer by a Cu(3.5) spacer. Finally, Ta(1.5)/Pt(3.0) is deposited, serving as a protective capping layer to prevent the magnetic stack from being damaged by subsequent processing steps and oxidation. The spin valve stack design outlined here is the one that was used in the point contact samples which are electrically characterized in Section 5.

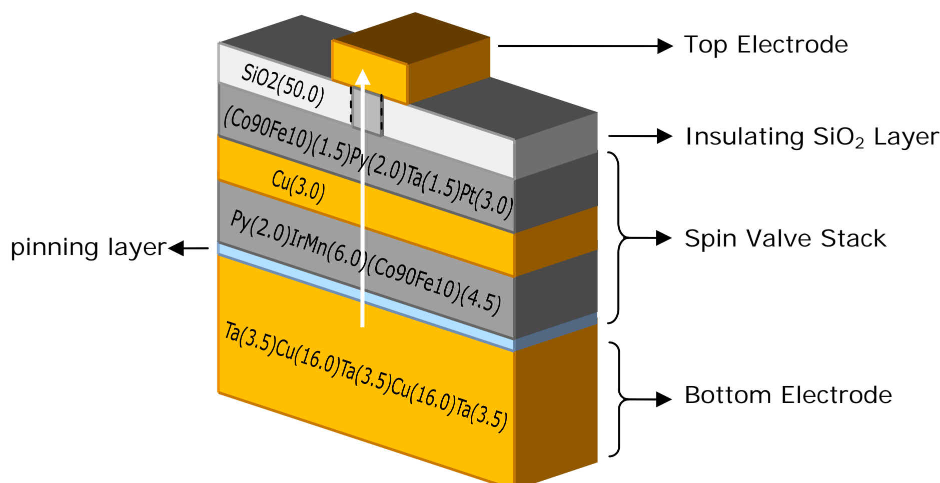

Figure 4-5: Simplified schematic of the CPP GMR thin film multilayer configuration, showing the bottom electrode, spin valve stack consisting of an (exchange bias pinned) fixed and free magnetic layer separated by a Cu spacer layer, insulating SiO_2 layer and top electrode. Note that the relative thickness of the spin valve stack is greatly exaggerated. Directly below the point contact, the current flows quasi-perpendicularly through the GMR multilayer towards the thin film plane, as is indicated by the vertical arrow.

Thin film patterning. Returning to Figure 4-3-A, patterning of the deposited thin film is generally performed by either a subtractive wet or dry etch process or by lift-off, both of which were discussed in Section 3.2.2. Compared to a lift-off procedure, ion-mill patterning of a multilayer stack is more complicated for several reasons. First of all, the required time for milling through the entire multilayer is determined by the ion-mill etch rate of a compound stack of different materials. To calculate the required ion-mill time, the mill rates of the separate materials making up the stack have to be calibrated precisely. An underestimate of the ion-mill time will result in incomplete removal of material between devices, which is unfavorable for (RF) device performance. On the other hand, when the ion-mill time is overestimated, milling will continue into the substrate, leading to an increased vertical step height between substrate surface level and magnetic stack top surface level. Instead of calculating the required milling time from calibrated ion-mill etch rates for the different materials in the multilayer, the required milling time is estimated from an optimization run by assessing the step height between structures and substrate level, together with the

substrate resistance between devices as a function of milling time. Secondly, it is observed that during the first patterning step appreciably larger mill times are required to obtain sufficient electrical isolation between devices than was estimated based on the height of the deposited material stack for which the deposition rates are known. A hypothetical explanation for the observed behavior is the implantation (and possibly also re-deposition) of ion-milled material into (or on) the GaAs substrate, thereby effectively increasing its conductance. Compared to lift-off, therefore, ion-milling always results in steps that are higher than the total magnetic stack height, as indicated in Figure 4-6. This can lead to problems in subsequent processing steps. For example, a relatively thin passivation layer may show discontinuities at the edges of patterned structures that display large step heights, resulting in current leakage paths through the passivation layer. A third drawback related to ion-milling is that, during the bombardment with highly energetic xenon ions, the photosensitive polymeric resist that is used to transfer the pattern to the thin film can get severely cross-linked, thereby reducing its solubility in solvents and complicating its removal before further processing steps. Therefore, ion-milling is performed in discrete time steps to allow for intermediate cooling of the substrate, avoiding cross-linking of the resist layer. Additionally, helium cooling is applied to the substrate holder during the entire milling session, for the same purpose. A fourth drawback of ion-milling is the possible re-deposition of sputtered material along the edges of patterned structures. This effect is absolutely detrimental in the fabrication of high-resistance tunneling devices, where shunting of the current along the sides of structures may deteriorate or completely destroy tunnel device performance.

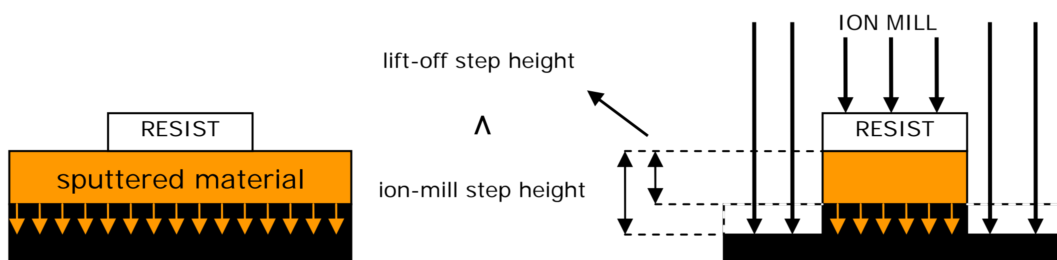

Figure 4-6: When sputtered material gets implanted in an insulating substrate, ion-milling into the substrate may be required to ensure electrical isolation between the different structures that are patterned on that substrate. As a result, compared with the lift-off process, ion-milling generally results in higher steps between the patterned structures and substrate surface level.

Considering that ion-milling generally delivers better structure outlining with clearly defined edges, the first patterning step of the samples discussed here is carried out by the ion-mill etching procedure, although lift-off was also observed to deliver acceptable results. For the magnetic stack described in this section, three two-minute mill steps lead to sufficient isolation between closely spaced points on the wafer.

After ion-milling, the step height between substrate and stack level was determined using Dektak profilometry to be 95±3 nm, whereas only 65 nm was expected based on the stack design outlined above. As discussed above, metallic atom implantation into the GaAs substrate may offer an explanation for the greater observed step height between substrate surface level and top of the magnetic stack than expected. In this case, ion-milling continued into the GaAs substrate for 30±3 nm to ensure complete electrical isolation between the structures.

Passivation. The patterned structures are then passivated with an insulating layer of RF-sputtered SiO_2, as indicated in Figure 4-3-B. In early process runs, bad adhesion of the sputtered SiO_2 onto the underlying Pt capping layer was observed. Inferior adhesion of the SiO_2 layer manifests itself through the formation of circular patches on the underlying patterned thin film elements where the SiO_2 becomes detached from the Pt. Although the SiO_2 film does remain largely continuous, on some occasions total adhesion loss of large parts of the passivation layer was observed at the sides of circular wafers when submitting the entire substrate to an intermediate ultrasound cleaning procedure. Since the metal atoms in a metal oxide are expected to provide stronger bonds with the Pt atoms of the capping layer as compared with SiO_2, the sputtering of SiO_2 is preceded by deposition of a thin Al(0.4) layer. The aluminum layer is subsequently plasma oxidized to form an intermediate Al_2O_3 adhesion layer between the Pt capping and the SiO_2 to be deposited afterwards. This procedure proved to enhance the adhesion of the SiO_2 passivation layer onto the patterned structures, while compatibility with the buffered HF wet etching process used to etch the nanometer scale point contacts into the SiO_2/Al_2O_3 layer is maintained [46].

Point contact definition. After passivation of the magnetic thin film elements with insulating SiO_2, both the micrometer scale side contacts and the nanometer scale point contacts are defined in a single e-beam lithography step using a PMMA resist layer. The side contacts carry current towards or from the bottom electrode of the spin valve stack, while the point contacts assist in the creation of quasi-CPP current paths in the magnetic film exactly under the point contact area. Figure 4-3-C only illustrates the definition of the nanometer scale point contacts; the rectangular, micrometer-size side contacts are omitted in this drawing. To obtain feature sizes consistent with the designed e-beam overlay mask, the e-beam doses applied in the point contact writing process were optimized. The e-beam dose is a measure for the amount of exposure the PMMA resist receives from the electron-beam, which is usually controlled by varying the time a certain part of the design is exposed to a constant intensity electron beam. Large doses result in features sizes that are exaggerated with respect to the design through the proximity effect, while small doses lead to incomplete exposure of the resist layer, resulting in smaller feature sizes or incomplete patterning. The exposed parts of the PMMA layer are dissolved in a developing agent consisting of a 1:1

mixture of MIBK and IPA, followed by a development stop in either IPA or n-Propanol (1-propanol). The developed areas define the point contacts, side contacts, and some additional larger structures that are incorporated in the design to determine the SiO_2 layer thickness using profiling techniques such as Dektak profilometry. Immediately after the development of the PMMA resist layer, prior to moving on to the SiO_2 wet etch, a short oxygen plasma scavenge step is applied to remove eventual PMMA residuals on the bottom and along the edges of the developed areas. Next, the current gateways are etched into the SiO_2 layer using a buffered hydrofluoric (BHF) wet etch solution. While precise control of this etch step is less important for the larger structures, it is critical for the small point contacts whose dimensions have to be accurately determined on the nanometer scale. The isotropic BHF wet etch process is controlled by parameters such as the SiO_2 layer thickness, BHF concentration, etch rate and dip time. The dip time is the time the BHF is allowed to react with the SiO_2 that is located in the areas were the PMMA layer has been developed after e-beam exposure. BHF selectively etches SiO_2 and its action vertically stops on the Pt capping layer underneath the passivation layer. A prematurely stopped etching process results in partial etching of the SiO_2 layer, so that the point contacts are not or incompletely opened. On the other hand, an over-etch results in point contacts with sizes much larger than the ones drawn in the e-beam mask. Although the wet etch stops vertically when the etching agent reaches the Pt capping layer, it may still continue laterally, due to the isotropic character of the BHF wet etch process. It is clear that both effects are undesirable and may impede the reproducibility of this process step. In order to clearly define this fabrication step, one must have specific control of the SiO_2 layer thickness, the BHF dip time and to some extent the SiO_2 quality, as this may influence the reaction with BHF (i.e. the etch rate). For example, etch rates may differ for contaminated or non-stoichiometric SiO_2. Therefore, the quality and thickness of the sputter-deposited SiO_2 is continuously monitored through ellipsometry measurements. As already mentioned in the previous paragraph, the SiO_2 passivation process is preceded by the formation of a thin Al_2O_3 adhesion layer between the Pt capping layer of the spin valve and the actual SiO_2. The BHF wet etch process discussed in this paragraph is compatible with this approach, as BHF is known to etch Al_2O_3 [46], so that the Pt capping layer is successfully reached by employing a BHF wet etch for point contact definition.

4.2.2. Electrode Definition

The following paragraphs describe the fabrication of the top electrodes, including the small tips on the BLS structures.

BLS tips preparation layer. First, a Ti(5.0)/Au(120.0) layer is sputter-deposited uniformly over the substrate as indicated in Figure 4-3-D. The only function of this

layer is to enable the manufacturing of the small BLS tips at the end of the regular top electrodes. The Ti(5.0) layer provides improved adhesion of the Au layer onto the underlying SiO_2. Although thicker adhesion layers such as Ti(10.0) and Ti(30.0) are more commonly employed as they provide even better bonding of the Au layer to the SiO_2 passivation layer, the thickness of the Ti layer is purposely maintained at a minimum here. This is due to the lower ion-mill etch rate of Ti compared to that of Au and the etch time limit imposed by the FOX12 resist process in the definition of the small tips (see further).

Top electrode definition. Rather than instantly moving on to the definition of the small tips with e-beam lithography, first, the top electrodes are defined in a second Au(120.0)/Ti(5.0) layer that is sputter-deposited on top of the uniform Ti(5.0)/Au(120.0) layer already in place. The top electrodes are defined using conventional optical lithography and lift-off as illustrated in Figure 4-3-E. Note that optical alignment of the top electrodes is performed through the uniform Ti(5.0)/Au(120.0) layer. This poses no problem since the markers incorporated into the spin valve layer provide sufficient contrast for optical alignment purposes, even after they have been covered by the uniform Ti(5.0)/Au(120.0) layer. The purpose of the top Ti(5.0) layer is to provide an buffer ion-milling as to maintain maximum electrode thickness, which will be considered when the final ion-mill step is discussed.

E-beam marker clearing. At this point, the process has delivered a substrate carrying spin valve microstructures covered with an insulating SiO_2 layer which are reached with conducting material through side and point contacts. Everything is covered with a uniform Ti(5.0)/Au(120.0) layer and the top electrodes have been defined in the Au(120.0)/Ti(5.0) layer, except for the small tips of the BLS structures. These tips will be defined using a FOX12 e-beam lithography step and ion-mill etching into the uniform Ti(5.0)/Au(120.0) layer, whose purpose now becomes clear. Because the BLS tips are only slightly oversized with respect to the point contacts they have to cover, exact location of these tips above the point contacts that were previously etched into the SiO_2 layer is a prerequisite for obtaining a functional device, imposing strict alignment requirements on the e-beam definition of these tips. Note that the e-beam markers required for high-precision automated alignment by the e-beam system have been covered by a uniform Ti(5.0)/Au(120.0) layer. Of course, a 50 nm thick SiO_2 layer is also present, but this layer is transparent to the e-beam alignment process. In order to provide sufficient contrast for alignment, the clearing of a set of e-beam markers which were covered by the uniform Ti(5.0)/Au(120.0) layer is required, which is depicted in Figure 4-3-F. This is performed through an additional optical lithography step that defines squares on top of the e-beam markers. The Au in these square areas is then removed using a chemical Au wet etching process using a 11.29 g

NaI, 64 g I_2 and 800 ml H_2O solution. The etch time is determined experimentally so that sufficient contrast is generated between the e-beam markers and the remaining gold. The marker clearance step is illustrated in detail in Figure 4-7.

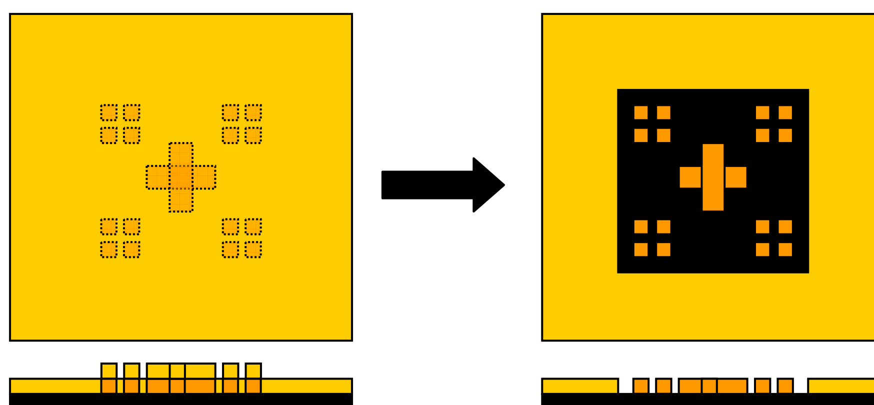

Figure 4-7: The e-beam markers that were covered by the uniform Ti(5.0)/Au(120.0) layer have to be cleared to enable e-beam alignment and definition of the small BLS tips. The clearing is performed by defining squares on top of the e-beam marker crosses with conventional optical lithography, followed by chemical etching of the Au until sufficient contrast is obtained.

BLS tips definition. After the e-beam markers have been cleared, the process continues with the definition of the small BLS tips for the devices with optical access. The 400 nm wide tips require precise definition and accurate alignment over the point contacts underneath and are therefore defined by an e-beam process using FOX12 flowable oxide negative resist. Upon exposure with energetic electrons, the FOX12 resist hardens into SiO_2 that acts as a hard mask (illustrated by the black area in Figure 4-3-G) for the subsequent ion-milling of the tip pattern into the underlying uniform Ti(5.0)/Au(120.0) layer. The thickness and etch rate of the cured FOX12 determine the ion-mill time available before complete removal of the hard mask. The hard mask should provide sufficient ion mill time to remove the uniform layer in between structures, while at the same time maximum thickness of the tips should be maintained. The required ion-mill time for a spin-coated 80±5 nm FOX12 layer can be calculated based on an ion-mill rate calibration for cured FOX12. This rate was determined to be 15±2 nm/min, based on an ion-mill rate of 35 nm/min for Au (see Section 4.3). Based on this mill rate, total removal of the FOX12 layer results for a mill time between 4,4 and 6,5 minutes. The corresponding maximum pure Au layer thickness that can be milled in this time lies between 154 and 227 nm. This thickness determines the maximum height of the tips at the location where they make contact with the point contact. However, due to the insertion of a Ti adhesion layer (whose mill rate was determined to be much lower than that of Au at approximately 3 nm/min) between the SiO_2 passivation and Au layer, the thickness of the uniform Au

layer for the combination with a 5.0 nm Ti layer is reduced to 120 nm. While a thicker Ti adhesion layer improves the adhesion of the Au to the SiO_2 passivation layer, the maximum thickness limit on the Au part of the uniform layer would be reduced considerably because of the associated reduction in remaining time available for milling the Au part of the tips when a considerable amount of Ti is present. To maintain maximum thickness of the Au layer, the Ti adhesion layer is kept minimal at 5.0 nm. The insertion of a 5.0 nm Ti adhesion layer was observed to visibly enhance adhesion properties, preventing the Au to be easily scratched off when electrical connections to the devices were made through measurement probes, while it only marginally affected the thickness limit on the Au part of the layer (and thus, the total layer thickness).

The time required to mill entirely through the uniform layer was estimated based on the obtained etch rates for Ti, Au and cured FOX12 and verified experimentally by testing the (absence of) electrical conductivity between separate structures. The tips are milled in three steps of two minutes, while helium cooling is applied at the back of the substrate at all times. This is depicted in Figure 4-3-H.

Final device. The resulting device structure after the final ion-mill step is presented in Figure 4-3-I. The top electrode beginning at the left shows some overlap with the small BLS electrode tip that contacts the point contact. Note that the e-beam markers have disappeared during the last ion-mill step. The careful reader may wonder whether the steps for defining the BLS tips and the main part of the top electrodes may be reversed. While this is in principle possible, the procedure adapted above does not suffer from residual cured FOX12 that may impede the electrical contact in the overlapping area between the small tips and the rest of the electrodes.

4.2.3. Evaluation of the BLS Tip Design

For the structures featuring optical access to the extended magnetic layer in the close vicinity of the lithographically defined point contact, the realization of very small tips at the ends of the top electrode strip lines is required. These tip are maintained as small as possible to allow the focused laser spot in a Brillouin light scattering setup (approximately 300 nm in diameter) to probe the free magnetic layer in the close vicinity of the point contact, which would be impossible if the area of interest was covered by a regular size metallic electrode. Moreover, exact location of these tips above the point contacts is a prerequisite for obtaining a functional device. Finally, in synchronization experiments, where both point contacts and contacting tips have to be very closely spaced, limits in the lithographic process may be encountered. The following paragraphs evaluate the tip design as it is currently implemented in the BLS and synchronization point contact devices (see Figure 4-1-c and -d).

As was discussed in Section 4.2.2, the final part of the top contacting electrode (i.e. the ‘BLS tip’) is fabricated using an e-beam lithography step, followed by ion-milling of the uniform Au layer around the tip. The SEM images in Figure 4-8 show that fabrication of very small tips has been realized and that closely spaced tip designs are equally feasible, enabling independent contacting of discrete point contacts in close proximity to each other which will allow for future synchronization experiments.

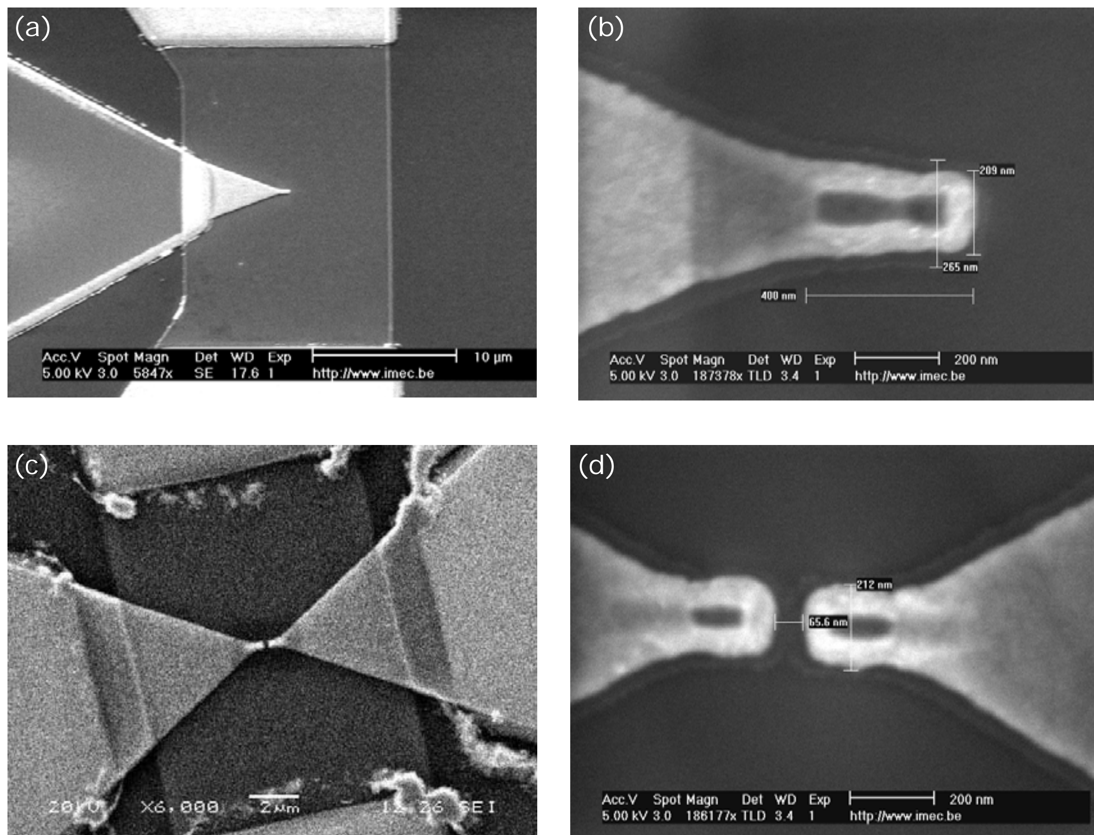

Figure 4-8: SEM images of the small tip ends of the top electrodes on structures with optical access to the magnetic layer around the point contact(s). The dark horizontal lines on the tips in (b) and (d) may indicate residual FOX12 or a transferred gradient due to the FOX12 profile after development. The edges around the structures are supposedly related to redeposition of Au. Two closely spaced tips are shown in (c) and (d), with a 65 nm gap between the tip ends.

As can be observed, the tip widths obtained from the SEM images indicate that the tips are at present only approximately 210 nm in width compared to the lateral dimension of 400 nm the design aimed for. This makes successful alignment of the tips very critical, considering that point contacts of up to 200 nm in diameter are to be connected. Moreover, the smaller the tips become, the more prone they get to destruction by large currents. Broadening of the tips may be accomplished by either increasing the e-beam dose used to write these tips or by slightly resizing their design

to a larger width. The latter is favorable for maintaining proper spacing of the tips in the synchronization structures. In Figure 4-8, edges are noticeable around the milled tips, which are thought to be due to re-deposition of milled material (Au). Also, a dark ridge is observed at the center line of the tips, which may indicate residual cured FOX12 or a transferred gradient in the contacting material profile due to the FOX12 profile after development.

To obtain a functional device, it is important that the tip be located exactly above the point contact. This can be verified through a simple electrical measurement which assesses whether the device conducts current. During the electrical characterization of the BLS structures, it became clear that only a limited current could be directed through the tips before the devices were damaged. When the currents were increased beyond approximately 25 mA, device resistance first increased before the point contact devices broke down systematically around 30 mA. Since corresponding four-probe and RF devices with equal point contact size generally are able to guide a larger amount of current (up to 45 mA), the main factor in the breakdown process is suspected to be the design of the tip, rather than damage to the point contact itself, although this has not been explicitly verified. Clearly, the relatively low breakdown current limit makes it difficult to induce high frequency spin torque driven oscillations in the sample, since currently, the tips seem to break down for currents near the critical current required to start high frequency, direct current induced oscillations. However, RF AC current excited dynamics could still be recorded, as will be discussed in Section 5.2.

4.3. FOX12 Ion-Mill Rate Calibration

This section discusses the ion mill rate calibration procedure for the cured Dow Corning Flowable Oxide 12 (FOX12), which is used as a hard mask for the BLS tip pattern transfer to the uniform Ti(5.0)/Au(120.0) layer. This rate eventually determines the maximum thickness of the uniform Ti/Au layer from which the BLS tips are fabricated. The calibration procedure is provided here as a technical fabcrication detail, since it deviates from the standard calibration techniques that can be used for most materials. Section 4.3.1 introduces the standard ion mill rate calibration procedure that can be applied to most materials. Section 4.3.2 discusses how the ion mill rate of cured FOX12 can be obtained, based on the ion mill rate of Au as obtained from the standard procedure.

4.3.1. Standard Calibration Procedure

The standard technique for determining the ion mill rate of a material is discussed here. A thick layer of the material is deposited onto a substrate, followed by the

definition of a resist pattern using optical lithography. Any mask can be used that contains structures which can afterwards be assessed with Dektak surface profilometry. After an ion mill step of duration t_0, the resist is stripped and the step heights $D(t=t_0)$ that occur over the patterned structures are assessed using Dektak surface profilometry. The ion mill etch rate R is then calculated as the ratio of the layer thickness that has been etched away and the time t_0,

$$R = \frac{D(t = t_0)}{t_0}. \qquad (4\text{-}1)$$

Using thicker material layers, longer mill times and averaging on the Dektak measurement data improves accuracy. Note that the total mill time is somehow limited due to resist cross-linking that may occur for longer mill times. When the resist gets 'burned' it may become difficult to remove and the Dektak readings become unreliable.

4.3.2. FOX12 Calibration Procedure

The standard calibration technique described in the previous section is not applicable to the determination of the ion mill etch rate of cured FOX12. Since ion milling is in principle a non-selective etch process (the energetic plasma ions sputter away whatever material they impinge on), a uniform layer of material is required to perform an ion mill rate calibration. Because FOX12 resist hardens into a SiO_2-like hard mask upon e-beam exposure, in order to obtain a uniform layer of cured FOX12, the entire substrate should be scanned with the focused e-beam spot, which is not feasible due to the slow scanning nature of the e-beam exposure. Therefore, an alternative (indirect) approach is proposed.

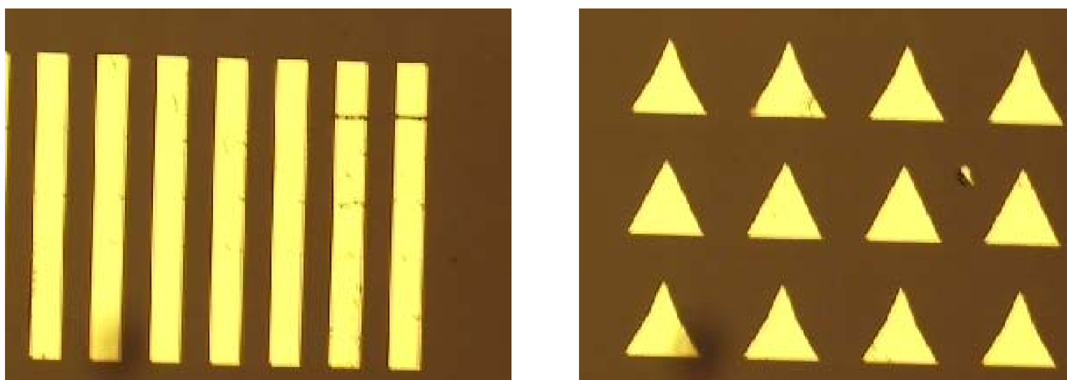

Figure 4-9: The strips (A) and triangles (B) from which the step heights are obtained using Dektak surface profilometry.

A relatively thick uniform material layer (e.g. Au) is deposited on a substrate, which is then spin-coated with a FOX12 resist layer. Using e-beam lithography, a design containing rectangular strips of 50x100 μm^2 and triangles of comparable size (see Figure 4-9 A and B) is transferred onto the substrate in the form of a cured FOX12 hard mask.

After exposure and development, the initial thickness F_0 of the cured FOX12 hard mask is obtained by Dektak surface profilometry, performed on the strips and triangles. Subsequently, the substrate is subjected to a series of ion mill steps. Between every mill step, the substrate is taken out of the ion mill system and the height difference between the top of the cured FOX12 layer and the substrate Au level, D(t) (see Figure 4-10), is recorded using Dektak surface profilometry.

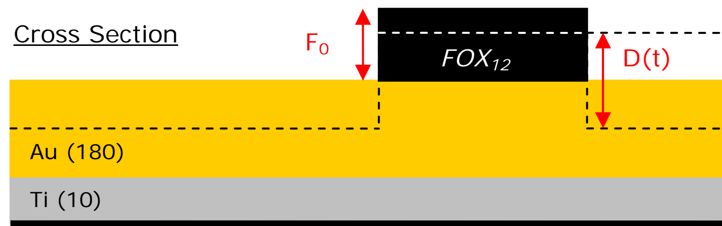

Figure 4-10: Cross-sectional view of a cured FOX12 hard mask feature on top of a uniform Au layer and the effect of an ion-mill step.

From Figure 4-10, it becomes clear how the FOX12 etch rate can be deduced from the step heights D(t) recorded as a function of time. During every subsequent ion mill step, both cured FOX12 and Au are etched. The initial FOX12 thickness F_0 will thus be reduced by an amount $R_{FOX12}\cdot t$, with R_{FOX12} the etch rate of the cured FOX12 and t the ion mill time. At the same time, an amount $R_{Au}\cdot t$ is milled away in the Au layer, where R_{Au} is the mill rate of Au, which can be obtained with the standard calibration procedure described in Section 4.3.1. The resulting step height can now be written as

$$D(t) = F_0 - R_{FOX12}\cdot t + R_{Au}\cdot t\,. \tag{4-2}$$

Rearranging this expression gives

$$D(t) - R_{Au}\cdot t = F_0 - R_{FOX12}\cdot t\,. \tag{4-3}$$

Since D(t) is provided by the Dektak measurements and $R_{Au}\cdot t$ can be calculated from the standard Au mill rate calibration, the left hand side of this equation is directly obtainable from a measurement of the step heights as a function of time. The obtained values should follow the linear trend given by the right hand side (where F_0 is also

known from the initial Dektak measurement). The FOX12 etch rate, R_{FOX12}, can then be determined as the negative slope of the linear function in the right hand side.

Now, the actual value of the FOX12 ion mill etch rate is determined. The substrate used is the full spin valve stack described in Section 4.2.1, but with a relatively thick uniform Ti(10.0)/Au(180.0) top layer. The thickness of the FOX12 resist after exposure and development is determined by an initial Dektak measurement, yielding an average value of F_0 = 75 nm. Using the standard calibration procedure, the ion mill rate of Au is determined to be 35 nm/min. The substrate is then subjected to seven one-minute ion mill steps. After each step, the average step height is recorded. The left hand side of equation (4-3) can then be calculated and the result is plotted in Figure 4-11.

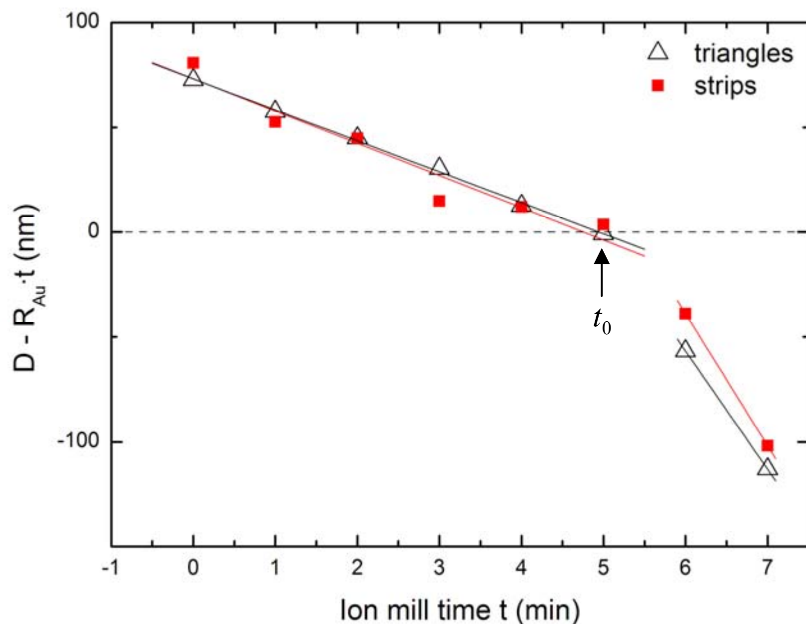

Figure 4-11: The left hand side of equation (4-3) is plotted as a function of mill time. A linear fit generates the mill rate for cured FOX12. After 5.1 minutes (t_0), the slope abruptly changes, indicating that the 180 nm Au layer has been milled away completely. Thereafter, the slope is related to the mill rate of the Ti layer under the Au.

From this figure, the ion mill etch rate of cured FOX12 is determined as the negative slope of a linear fit through the first 5 measurement points. This yields an average 15 nm/min for the strips and triangles. Interestingly, after 5.1 minutes, the slope abruptly changes to an increased negative value. This behavior is attributed to the fact that either the FOX12 has been removed completely or that an interface to another material under the 180 nm Au layer has been reached. Note that in the first case, provided the Au layer is thick enough so that ion milling continues into an uniform Au layer, at the intercept with the x-axis ($t = t_0$), the curve would resume a slope given

by the mill rate of Au. This can be seen from equation (4-3), since setting the left side to zero for $t = t_0$ yields both of the statements

$$D(t_0) = R_{Au} \cdot t_0, \tag{4-4}$$

and

$$R_{FOX} = \frac{F_0}{t_0}. \tag{4-5}$$

The first statement indicates that at the crossing point, the step height is exactly the amount of Au that has been milled away up to that time, which is to be expected, since at that precise time, all FOX12 has been removed. The second statement is the analogue of equation (4-1), since in the time t_0 the entire FOX12 layer is exactly removed. From that moment on, the patterned structure and the surrounding layer get ion milled at the same rate and the step height remains constant. This implies that the left hand side of equation (4-3) will indeed further scale linearly with time, with a slope given by the mill rate of Au (replace FOX12 by Au in equation (4-3)).

However, the slope observed in Figure 4-11 after $t = t_0$ (54 nm/min) clearly does not correspond to the mill rate of Au which was determined to be only 35 nm/min. Therefore, the second explanation for the abrupt slope change, the encounter of a material interface, is thought to be applicable here. Indeed, based on the R_{Au} = 35 nm/min mill rate, t_0 = 5.1 minutes corresponds exactly to the time necessary to mill away the entire 180 nm Au layer, after which ion milling continues into the underlying Ti(10.0) layer.

In this case, the procedure outlined above can be repeated, with the understanding that the roles of FOX12 and Au are now fulfilled by Au and Ti. The governing equation becomes

$$D'(t') = F_0^{'} - R_{Au} \cdot t' + R_{Ti} \cdot t', \tag{4-6}$$

with the prime indicating a time after $t = t_0$. Rearranging this expression gives (keep in mind that now the mill rate of the top instead of the bottom layer is known, leading to the plus sign)

$$D'(t') + R_{Au} \cdot t' = F_0^{'}{}' + R_{Ti} \cdot t'. \tag{4-7}$$

Casting this into a similar form as equation (4-3), so that it can be applied to Figure 4-11, yields

$$D'(t') - R_{Au} \cdot t' = F_0'' + R_{Ti} \cdot t' - 2R_{Au} \cdot t' = F_0'' + (R_{Ti} - 2R_{Au}) \cdot t' . \tag{4-8}$$

The slope is now given by R_{Ti} - $2R_{Au}$. Note that, since the time t_0 (coincidentally) also corresponds to the time necessary to mill away the entire FOX12 layer, only the last two points are considered in the linear fit, leading to a value of 10.4 nm/min for the ion mill rate of Ti. The value obtained here is expected to be only approximately accurate, since only two points were considered for the linear fit. Moreover, since the Ti layer is only 10 nm thick, the last point may have encountered another transition to the thin film layer under Ti. A regular calibration of the ion mill rate for Ti resulted in a value of 7.8 nm/min.

5. Experimental Results

In the previous section, the point contact nano-oscillator fabrication process was discussed in detail. This process resulted in the realization of various test structures suited to the different electrical and optical measurements that are the topic of this section. The associated experimental setups have been introduced in Section 3.

First, the physical appearance of the nanometer scale point contacts is characterized in Section 5.1.1, employing techniques such as SEM (scanning electron microscopy), AFM (atomic force microscopy) and four-probe resistance measurements. The resulting data provide detailed information about the morphology of the point contact holes etched into the insulating SiO_2 layer and enable deeper insight into the experimental techniques used to fabricate them. A central question in this discussion concerns the sizes of the resulting critical features, i.e. both the point contacts and the small BLS tips for the devices with optical access. The point contacts will be specifically addressed in Section 5.1.1, while the discussion of the BLS tips was grouped with the discussion of the fabrication process in Section 4.2.3.

After studying their physical appearance, the functional behavior of the point contact devices is assessed through four-probe (magneto)resistance measurements in Section 5.1.2. When relating device resistance and magnetoresistance with point contact size, unexpected results are observed. Finite element simulations shed some light on these observations by examining the current distributions in the device electrodes. Based on the conclusions from the simulations, a model is constructed that successfully reproduces the observed magnetoresistance values.

Section 5.2 discusses observed microwave RF emission upon application of a direct current to a point contact device fabricated in this work. The observation of low frequency phenomena in the emission spectrum is assumed to be due to the gyrotropic movement of a magnetic vortex core in the free magnetic layer under the point contact area. The emission spectrum is shown to vary with applied current and external magnetic field, expressing the frequency-agility of the point contact oscillator device.

Finally, Section 5.3 provides some preliminary results from the optical Brillouin light scattering experiments performed on devices featuring optical access to the extended free layer around the point contact. The aim of these measurements is to study spin wave emission from the point contact into the extended free magnetic layer, since these spin waves may provide a coupling mechanism for the frequency and phase locking of multiple nano-oscillators.

5.1. *Point Contact Characterization*

Because spin torque phenomena such as current-induced switching and RF oscillation of the moment of a free magnetic layer rely heavily on current confinement to very small regions, it is important to know the exact dimensions of the point contact holes etched into the insulating SiO_2 layer (see Figure 5-1). The structural assets of fabricated point contact devices are explored in Section 5.1.1, using imaging techniques such as SEM and AFM. This enables the discussion of the relation of electrical device properties with cross-sectional point contact size in Section 5.1.2.

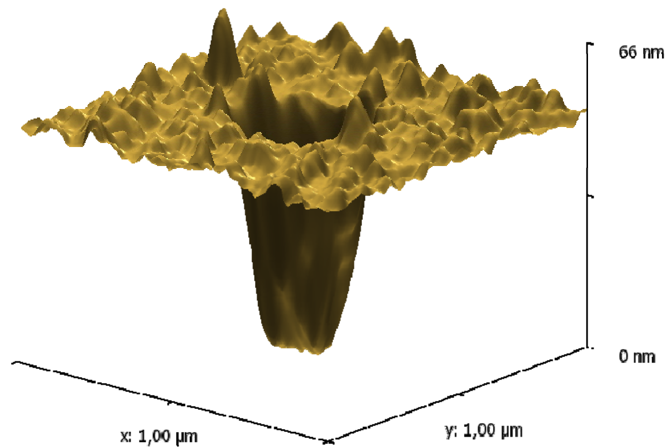

Figure 5-1: Three-dimensional view of a point contact etched into an insulating SiO_2 layer, as obtained from an AFM scan.

5.1.1. Size and Morphology

During the fabrication process, the point contacts are etched into an insulating SiO_2 layer using a BHF chemical agent. The thickness of the SiO_2 layer, the mask design and e-beam dose used to write the dots in the resist layer, the concentration of the BHF etching agent and the etch time determine the etching process and resulting point contact size. This size may deviate from that in the design when the process parameters mentioned above are not well controlled. For example, the BHF wet etch selectively etches SiO_2 and vertically stops on the underlying Pt layer that caps the spin valve stack. However, due to its isotropic character, the etch process may still continue laterally, leading to an increase in diameter of the etched point contacts when the etch time is chosen too long. On the other hand, etching for an insufficient amount of time will not or only partially expose the conducting layer under the SiO_2, resulting in an impaired device. Etch times can be estimated based upon the bulk etch rates of SiO_2, but are in practice determined empirically through an optimization step which determines the required etch time to produce point contacts that conduct current up to the smallest feature sizes.

While the lateral dimensions of the point contacts can be extracted from either SEM or AFM images, the latter technique features the added benefit of depth resolution which provides useful information on the exact surface morphology in and around the point contact, e.g. concerning the slopes of the point contact edges. Note that if a relation between device resistance and point contact size could be established, a simple resistance measurement would yield a third (indirect) method for determining the size of a point contact.

Figure 5-2 shows an AFM scan of the smallest point contact available, designed with 100 nm lateral diameter, along with a depth profile along a slice through its center. Determining the point contact diameter can be done by consistently determining the width of the profile at e.g. 10% or 90% of the surface level. As a first approximation, the 10% AFM level is expected to represent the real point contact diameter best, since it largely excludes the side wall slopes (indicating that SiO_2 is incompletely etched at those places) which are observed in both top and side view.

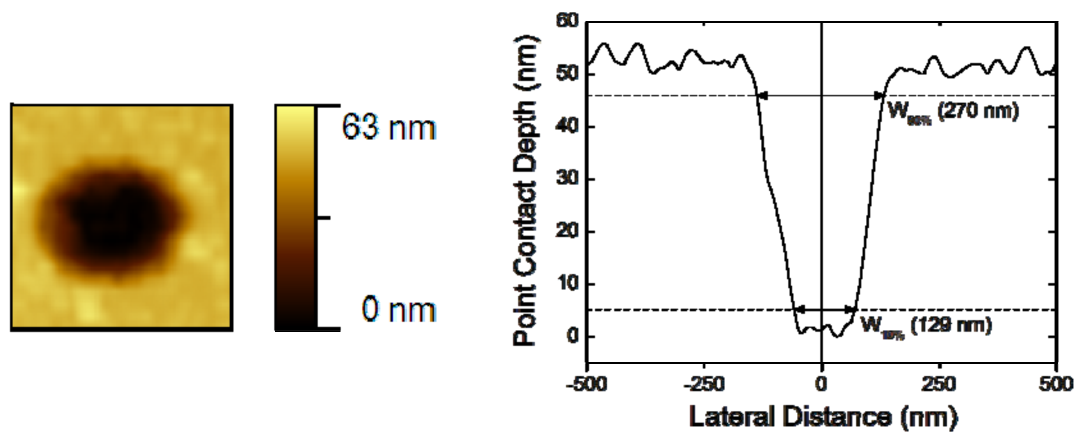

Figure 5-2: (Left) Typical AFM scan of a point contact etched into an insulating SiO_2 layer (corresponding to a top view of the point contact). (Right) Lateral depth profile of the smallest point contact (100 nm in the design) indicating the 10% and 90% widths, which are respectively under- and overestimating the widths obtained from SEM (see also Figure 5-4 and Figure 5-5). The 10% height value is considered most accurate, since it does not take into account the side walls were SiO_2 may not have been removed completely.

In general, care has to be taken when imaging high aspect ratio structures or structures with steep vertical profiles (actually, there exist special AFM probes for performing high aspect ratio scans), since the layout of the AFM tip may convolute with the images and depth profiles. This is explained with the help of Figure 5-3, which gives a schematic overview of the geometry of the AFM tip used to scan the point contacts. This tip has a tetrahedral form with surfaces at 18.30° and 18.40° angles with respect to the cantilever normal in front view and 9.21° and 30.84° in side view.

Considering the 30.84° side view tip angle, for a 50 nm deep structure, the tip surface would hit the point contact edge 50 nm·tan(30.84°) ≈ 30 nm before the tip actually reaches the edge. Expanding this reasoning, the angle range from 9.21° to 30.84° corresponds to offsets on the lateral widths ranging from approximately 8 nm to 30 nm. It can be concluded that for a perfectly rectangular etch profile (completely vertical edge) the total point contact width extracted at the bottom of the lateral profile shown in Figure 5-2 is underestimated by at least 16 nm in the best case and 60 nm in the worst case, depending on which side of the tip is used to scan the structures.

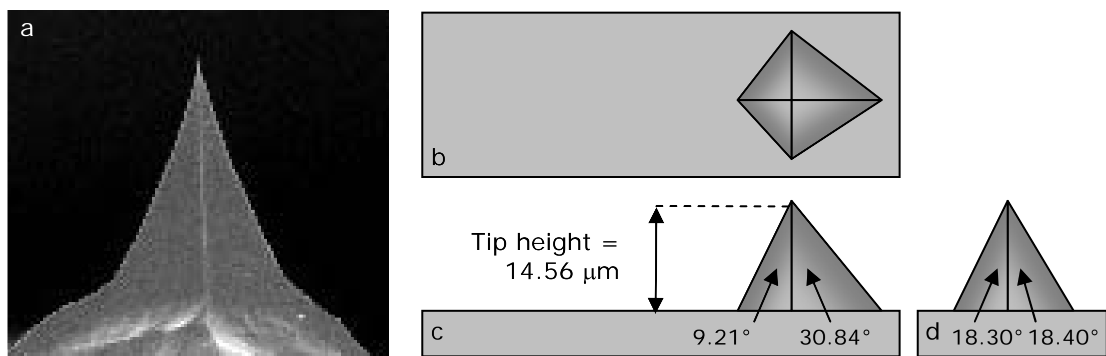

Figure 5-3: (a) SEM image of the AFM tip used to determine point contact sizes. The schematic (b) top, (c) side and (d) front views of the AFM tip indicate the angles the tip surfaces make with respect to the cantilever normal.

Of course, a 100 nm wide point contact etched 50 nm deep into a SiO_2 layer should not be considered a real high aspect ratio structure and, additionally, the edges of the point contact are not expected to be perfectly vertical, so the error induced by the tip geometry is expected to be further minimized. For steep side walls (or equivalently, broad tips) the observed slope is that of the tip surface. In all other cases, the physical slope of the edge is recovered. When scanning with the 18.30° tip side, there will only be an effect when the side wall slope is steeper than the complement of the tip angle, i.e. 71.70°. Note that the slope observed in Figure 5-2 amounts to only 33.6°, so that the observed slopes can be considered to be a valid representation of the physical point contact edges.

Figure 5-4 shows an SEM scan of a point contact designed with a diameter of 100 nm. The actual point contact diameter, extracted at the outer sides of the white spot, is determined to be 232 nm. Note that since part of the edge may correspond to the point contact sidewalls where SiO_2 has been removed incompletely, this value is expected to be an overestimate.

Figure 5-5 groups the results of the point contact size measurements carried out on the same sample with the various methods discussed above. The figure plots the obtained

widths as a function of the width expected from the design. For SEM, $AFM_{10\%}$ and $AFM_{90\%}$ the dependence is quite linear, although the offsets to the design function (errors on the diameter) vary for the various methods. The $AFM_{10\%}$ widths are at this moment believed to match the physical point contact sizes most closely, with an average offset of 41 nm to the design function.

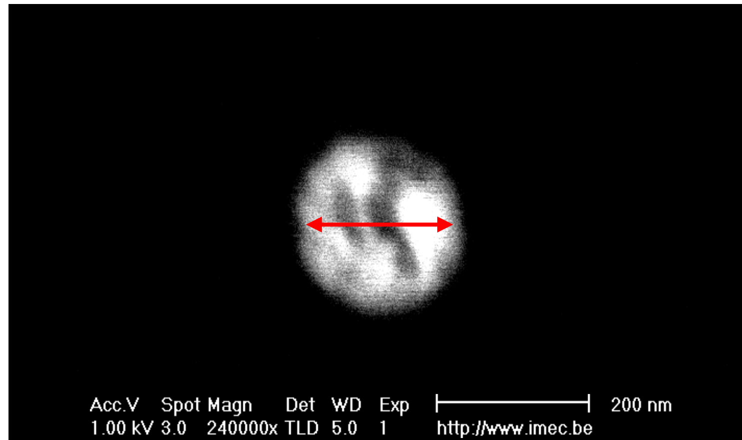

Figure 5-4: SEM image of the smallest point contact (100 nm in the design). The diameter extracted at the outer edges of the white spot reads 232 nm. Since a part of the edge may correspond to the point contact side walls where the SiO_2 may not have been removed completely, this value is expected to be an overestimate.

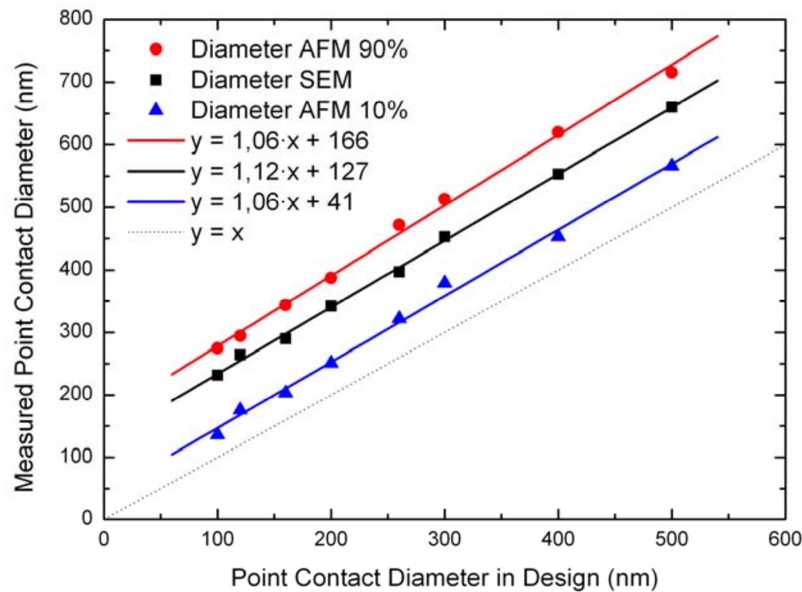

Figure 5-5: Comparison of point contact diameters extracted from SEM and AFM. For the AFM measurements, widths can be extracted at the 10% or 90% surface levels as illustrated in Figure 5-2. Linear fit parameters indicate that the point contact sizes follow the designed size almost linearly, with various offsets, either related to the etch process or to the method of width extraction. The physical diameter is expected to be most accurately represented by the $AFM_{10\%}$ widths.

In conclusion, taking into account the remarks made above about the possible inaccuracy of the AFM measurements due to tip geometry effects, the inability to determine the diameter accurately from the SEM images because of the uncertainty about the side wall slope and the minimized error on the $AFM_{10\%}$ measurements, the point contact sizes obtained from AFM measurements extracted at the 10% level are assumed to approximate the physical diameters of the point contacts most accurately. Therefore, these values will be used in any further calculations involving the point contact diameter. An important remark will be made on this in Section 5.1.2.3. There, based on a model fit, the point contact diameters obtained from SEM are believed to be more accurate.

5.1.2. Magnetoresistance

As stated in the previous section, a simple DC resistance measurement would yield a third, albeit indirect method for determining the size of a point contact in case the relation between point contact size and device resistance was established. Therefore, a set of samples was prepared featuring point contact devices with designed diameters of 100, 120, 160, 200, 260, 300, 400 and 500 nm, finished with four-terminal top electrodes in a cross geometry. This enables precise four-probe resistance measurements to be performed on these devices which can be linked to the physical point contact sizes obtained from AFM scans, as outlined in the previous section.

5.1.2.1. Experimental Observation

In a four-probe resistance measurement, the point contact device resistance is expected to originate purely from the point contact itself, since any contributions resulting from lead, spreading or galvanic contact resistances (or any other serial resistance for that matter) are supposed to be eliminated. Therefore, if a constant and uniform interface resistivity is assumed, the measured four-probe resistance is expected to scale inversely with point contact area. Alternatively, the point contact resistance times area (RxA) product is expected to remain constant. Moreover, although the resistance of the point contact itself may change with area, the value of the physical magnetoresistance effect MR (in percent) should not, as was shown in Section 2.1.4. Therefore, the measured MR figures are expected to be invariant with point contact area. Figure 5-6 displays the RxA and magnetoresistance values obtained from four-probe measurements of point contacts with different sizes, extracted from $AFM_{10\%}$ scans. Figure 5-7 displays a typical MR curve obtained from a four-probe measurement, indicating free layer switching around zero field and fixed layer switching around 40 mT. In contrast with the expectations outlined above, the resistance clearly does not scale inversely with point contact area, nor does the percentage MR reveal a constant value.

As will be shown in Section 5.1.2.3, the observed slope of the RxA curve in Figure 5-6 expresses the presence of a series resistance, which follows the slope variations. Although a positive slope is clearly present in the figure, deducing a precise linear trend from the measurement data is not straightforward, taking into account the measurement errors on both point contact diameter and resistance. Linking the observation of increasing RxA with decreasing MR' (the prime expresses that the value is obtained from a measurement), the hypothesis is put forward that in the total device resistance, there is a contribution that does not display magnetoresistive behavior. This would lead to a decrease of the MR figures which are calculated based on the total device resistance, including any additional series resistance.

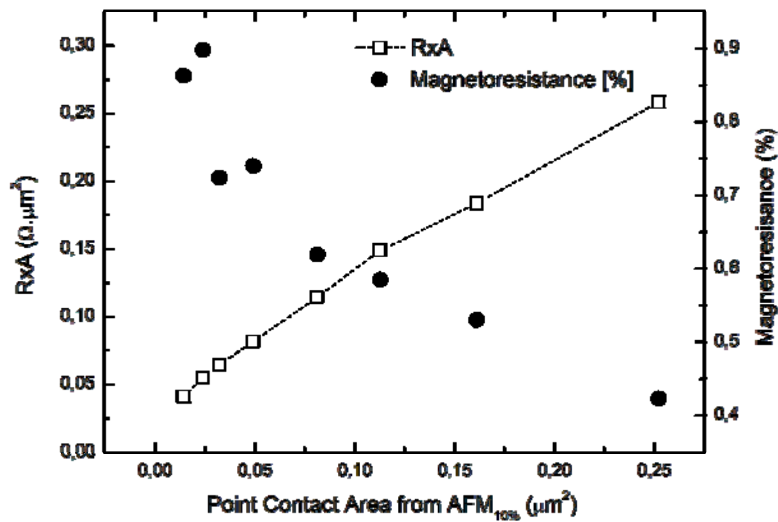

Figure 5-6: RxA (squares, left axis) and magnetoresistance (dots, right axis) values as a function of point contact size extracted from $AFM_{10\%}$ scans. The connecting line acts as a guide to the eye. Neither the RxA product, nor the MR value displays constant behavior.

The unexpected behavior of the observed resistance and magnetoresistance values as a function of point contact size urges a closer inspection of the four-probe point contact measurement strategy. As will become clear, intricate current distribution effects in the point contact device contacting electrodes may obscure a correct reading of the actual point contact resistance, demanding a careful interpretation of point contact resistance and magnetoresistance measurements when these are to be linked to point contact size.

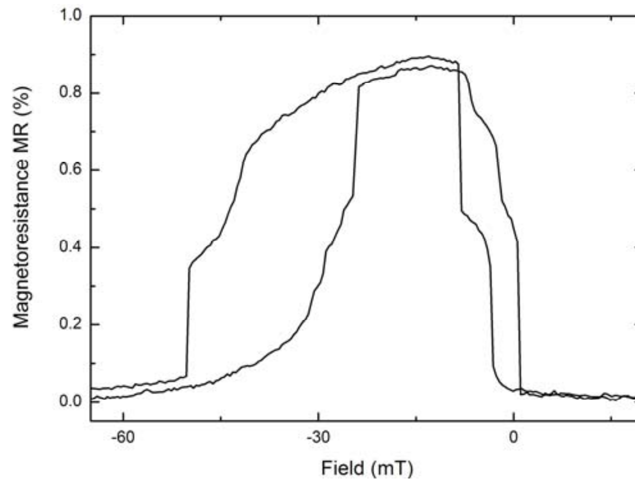

Figure 5-7: Magnetoresistance curve corresponding to the second smallest point contact size of Figure 5-6 (highest MR value). Switching of fixed and free spin valve layer is observed around -37.5 mT and -3.6 mT (due to coupling with the pinned layer). This spin valve was not annealed.

5.1.2.2. Current Distribution Simulations

To gain a better understanding of the point contact resistance and magnetoresistance figures obtained in the four-probe measurements, finite element simulations were performed that map the electrical potential across the electrodes in a four-probe cross geometry (see Figure 5-8). The electrodes are represented by rectangular conductive strips which are connected through a resistor at their respective midpoints, mimicking the presence of a point contact. The resistivity of the 10x5 μm^2 electrodes is fixed at $2 \cdot 10^{-8}$ $\Omega \cdot m$, representing the bulk value of Cu. The point contact RxA product is assumed to be constant, i.e. the intrinsic point contact resistance is assumed to scale inversely with cross section area. Therefore, any effects responsible for the unexpected behavior of resistance and MR figures are assumed to be due to the electrodes. The resistance of the point contact resistor is estimated based on experimental observations of device resistances for small point contact sizes and is fixed at 4 Ω for a 80x80 nm^2 point contact, corresponding to an RxA product of 25.6 $m\Omega \cdot \mu m^2$. The complete geometry is dicretized using a 500x500 nm^2 cells grid that densifies to 80x80 nm^2 cells in a 3x5 μm^2 central area around the point contact resistor. Increasing the point contact size corresponds to adding resistors in parallel to the initial one. For example, adding a single 4 Ω resistor corresponds to a doubling of the point contact area. Geometrically, the resistors are added at grid points as to produce a point contact shape that is as symmetric and compact as possible, as indicated in Figure 5-9.

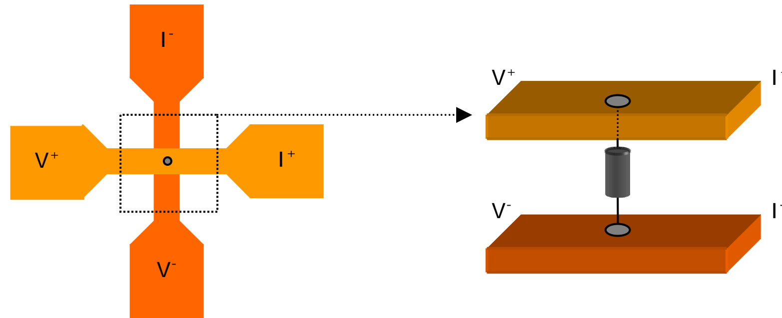

Figure 5-8: The electrodes of the four-probe measurement geometry (left) are modeled by rectangular strips, connected at their centers with a resistor, mimicking the presence of a point contact junction (right). Increasing the point contact size is equivalent with adding resistors in parallel to the one shown (assuming a constant RxA product for the point contact).

The complete resistor network discretization grid for the electrodes connected through a single point contact resistor is shown in Figure 5-10. Within this resistor network, every cell within the bottom and top strip is linked to its four nearest neighbors, while the strips themselves are cross-linked at their centers by a variable number of resistors, depending on the point contact size A. Using Kirchoff's laws, the current flowing through each resistor and the associated voltage drop can be computed. Considering the boundary conditions adapted in this approach, the current is injected with a uniform current density at the I^- side of the top strip. For computing the voltage difference V^+-V^-, the voltages are averaged over the appropriate strip edges.

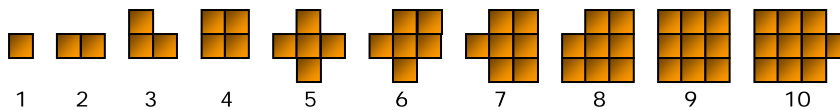

Figure 5-9: Increasing the point contact area is equivalent with adding point contact resistors in grid cells according to the sequence depicted above, which keeps the point contact geometry as symmetric and compact as possible. The center of each cell corresponds to a node in the resistor network used to discretize the contact strips (see also Figure 5-10).

The simulations first explore the qualitative behavior of the current distributions within the electrode strips. Secondly, the effect of electrode thickness (60 nm and 120 nm) and electrode width (4 μm, 5 μm and 6 μm) is explored. Finally, the effect of decreasing the point contact RxA value by a factor two is discussed. Due to computational limitations, the dimensions of the simulated problem were not intended to match those of fabricated devices exactly. It is expected, however, that for a similar aspect ratio (point contacts much smaller than width of the strips), the simulation results can be qualitatively generalized to different dimensions. The intention of these

simulations is therefore to gain a qualitative understanding of the behavior of the measured point contact resistance and MR figures. For a completely quantitative description, all parameters of the measurement and device should be considered, including the exact conductivity of the electrode material and the exact placement of the probes on the landing pads, which is always subject to slight variation.

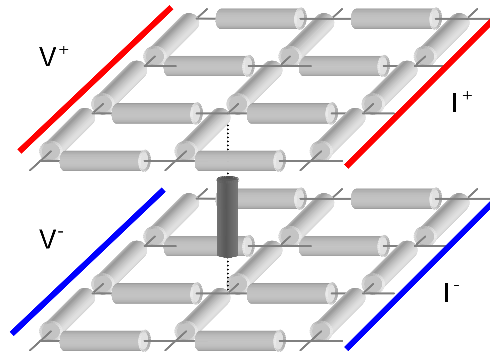

Figure 5-10: Part of the resistor-network discretization grids of the four-probe top and bottom strips. The point contact is modeled by a single resistor, cross-linking the strips together at their respective mid-points. Voltage and current polarities are indicated, corresponding to the simulation results displayed in Figure 5-11 and Figure 5-12.

Current Distribution in a 4 Ω - 80x80 nm² Point Contact

Figure 5-11 illustrates simulated equi-potential contours within the bottom strip electrode in a 9x5 μm^2 area around a 80x80 nm^2 point contact with nominal resistance of 4 Ω (See Figure 5-12 for the associated current distribution). In this figure, a unity current (heating and spin torque effects are not considered here) flows out of the point contact, located at the center, towards the right, where it is collected by the negative current probe. This is indicated by the strong gradient in the equi-potential profiles towards the right. However, note that there is also a non-zero gradient in the other directions, most notably in the negative x-direction. This corresponds to a current initially flowing away from the point contact towards the left side of the strip and then bending back to the current sink terminal at the right side. Since a voltage drop occurs when moving from the point contact to the left, the voltage measured by the voltage probe placed at the left edge does not correspond to the voltage in the close vicinity of the point contact. This results in an incorrect reading of the intrinsic point contact resistance by the voltage probes in a four-probe measurement, i.e. the actual voltage over the point contact is augmented with an additional voltage drop due to current distribution effects in the bottom electrode.

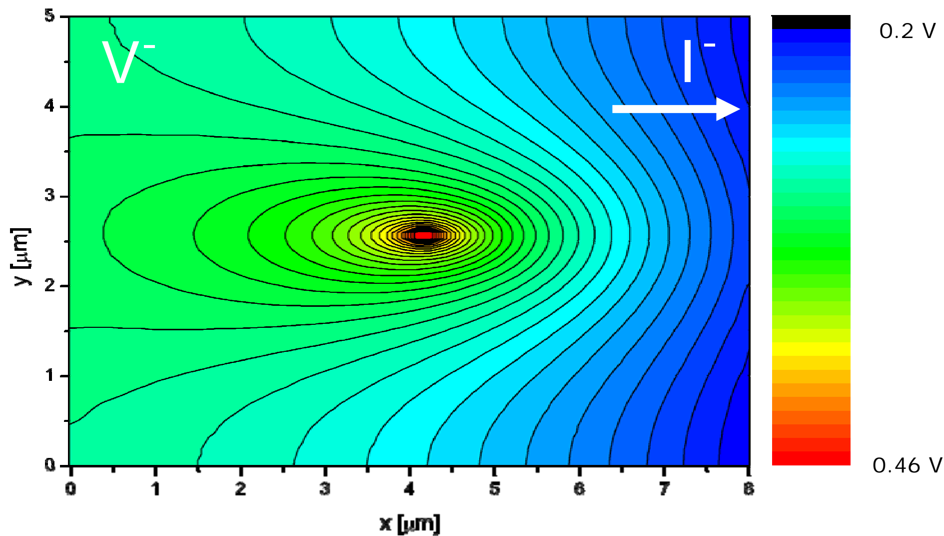

Figure 5-11: Simulated equi-potential profiles in the bottom electrode of a four-probe device within a 9x5 μm^2 area around the point contact. The point contact itself covers a 80x80 nm^2 area and has a resistance of 4 Ω. In this picture, a unity current (heating and spin torque effects are not considered here) flows out of the point contact located at the center towards the right, where it is collected by the negative current probe. This is indicated by the strong gradient in the equi-potential profiles towards the right. Because a voltage drop is accumulated from the center towards the left edge, the voltage measured by the voltage probe at the left does not correspond to the voltage in the close vicinity of the point contact itself. This results in an incorrect reading of the intrinsic point contact resistance by the voltage probes in a four-probe measurement.

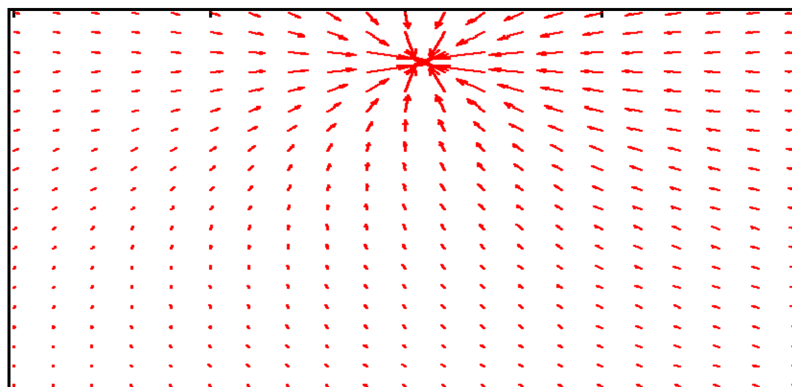

Figure 5-12: Current distribution around the point contact in the top electrode, corresponding to the simulated equi-potential profiles displayed in Figure 5-11. An overshoot of the current to the left can be observed, before the current flows into the point contact, towards the bottom electrode.

Effect of Electrode Thickness

While it is already clear that care has to be taken in determining the intrinsic point contact resistance from a general four-probe measurement, a further assessment can

provide more information about the influence of electrode thickness and point contact size, parameters that are accessible experimentally. Figure 5-13 summarizes apparent values of the RxA product as a function of point contact size (A), derived from the simulated voltage drops between the four-probe voltages V^+ and V^-, averaged over the electrode edges. The results are plotted as a function of 80x80 nm^2 area units, which is the area corresponding to a single 4 Ω point contact resistor cross-linking the electrodes. Its associated (intrinsic) RxA value is indicated in the figure by the dotted line. The simulated RxA values clearly overestimate the value expected from the intrinsic device resistance and the effect is observed to become more pronounced for increasing point contact size. When comparing electrodes with different thicknesses, the effect is less pronounced for thicker electrodes (120 nm, squares) than for thinner ones (60 nm, circles). In both cases, the increase is largely linear with point contact size, which indicates a constant series resistance, as will be explained in Section 5.1.2.3.

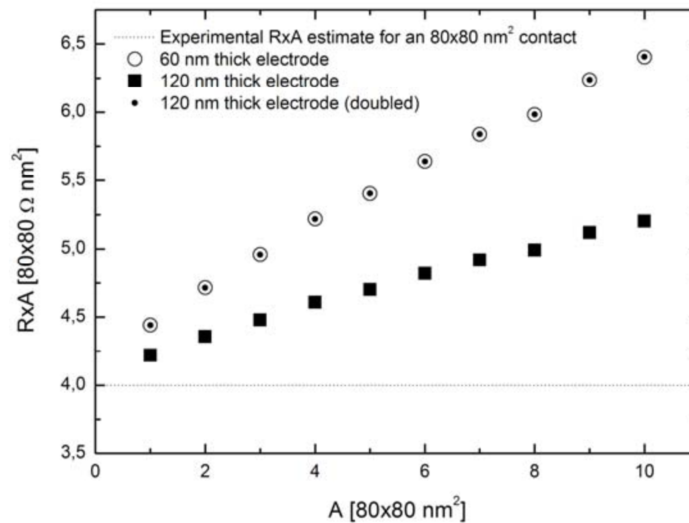

Figure 5-13: Apparent RxA values for varying point contact size obtained from finite element simulations of the current distributions in a four-probe cross geometry electrode. Electrodes with thicknesses of 60 nm and 120 nm were simulated. The horizontal axis expresses point contact size in 80x80 nm^2 area units, which is the area associated with a nominal point contact resistance of 4 Ω (estimated from experimental results). The corresponding intrinsic RxA value is indicated by the dotted line. The linear scaling of the offsets with point contact size indicates a constant series resistance. Multiplying the relative offsets for the 120 nm thick electrode (full squares) produces the filled dots, which lie exactly within the open circles corresponding to the offsets of the 60 nm electrode, indicating inverse scaling of the parasitic effect with electrode thickness. Consequently, using thicker electrodes decreases the measurement error in an intrinsic point contact resistance measurement.

More interestingly, the effect seems to scale inversely with electrode thickness, i.e. doubling the electrode thickness halves the observed parasitic voltage drops. This can be seen from Figure 5-13: doubling the 120 nm offsets (squares) produces the dots inside the 60 nm offset points (circles). Consequently, since a thicker electrode represents a decreased series resistance, implying decreased parasitic voltage drops, using thicker electrodes decreases the measurement error regarding the intrinsic point contact resistance.

Effect of Intrinsic Point Contact Resistance

The simulations performed above assumed a nominal intrinsic point contact resistance of 4 Ω associated with a contact area of 80x80 nm^2. In the following, the effect of decreasing the intrinsic resistance is explored by setting it to 2 Ω. Again, RxA values are simulated for varying point contact sizes, assuming an electrode thickness of 60 nm, so that the results can be compared with those obtained in the previous simulation. Figure 5-14 groups the previously obtained results for the 4 Ω point contact on the left axis with the results for the current simulation on the right axis. Note that the right axis has been shifted up, so that the intrinsic RxA values associated with the intrinsic point contact resistances of the two settings line up, enabling an easy comparison of the induced absolute offsets.

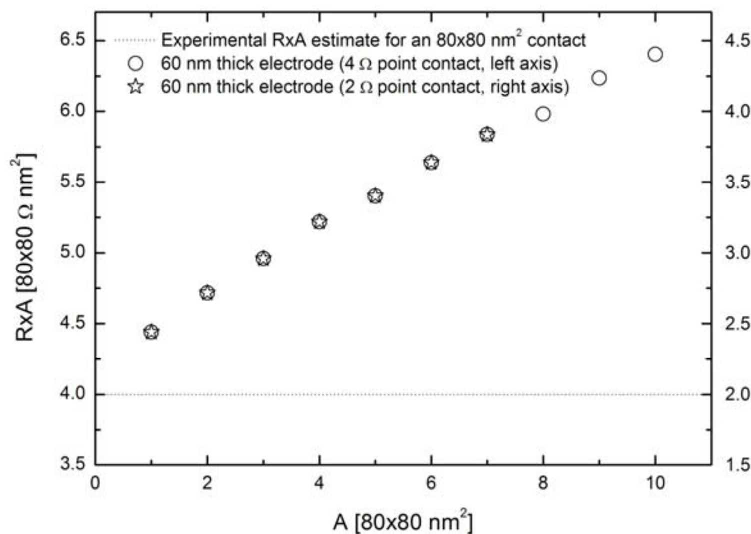

Figure 5-14: Simulated RxA values for point contacts with intrinsic resistances of 2 Ω and 4 Ω. Note that the right axis has been shifted up, so that the RxA values associated with the intrinsic point contact resistances of the two settings line up, enabling an easy comparison of the simulated absolute offsets. The resulting offsets for the 2 Ω point contact (stars) are observed to line up exactly with those of the 4 Ω point contact obtained in the previous simulation (open circles), indicating that the current distributions within the electrodes for these two cases must be identical. Since the absolute offsets in the two cases are identical, the relative error within a point contact measurement is largest for less resistive point contacts (i.e. low

intrinsic point contact resistance).

The resulting offsets for the 2 Ω point contact are observed to line up exactly with those of the 4 Ω point contact. This indicates that the current distributions within the electrodes in the two cases must be identical, since they produce identical parasitic resistances. Moreover, since the absolute offsets in the two cases are identical, the relative error within a point contact measurement is largest for less resistive point contacts (i.e. low intrinsic point contact resistance).

Effect of Electrode Width

The current distributions within the electrodes are expected to change with electrode width. Therefore, in a final experiment, the effect of altering the electrode width is investigated. Simulations were performed for 60 nm thick electrodes with widths of 4, 5 and 6 μm. As shown in Figure 5-15, wider electrodes seem to suffer more from current spreading around the point contact, leading to higher absolute offsets in the RxA values. In the limit situation that the electrodes overlap exactly with the point contact, the offsets are expected to vanish, since no current path would exist around the point contact, so that current would flow directly into the point contact and produce no additional voltage drop towards the voltage probes.

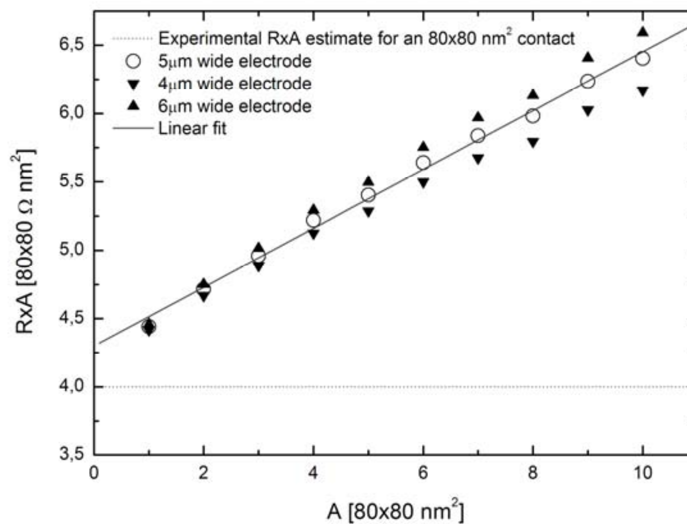

Figure 5-15: Effect of electrode width on simulated RxA values. The upward- and downward-facing triangles correspond to increasing or reducing the electrode width by 1 μm from the 5 μm width used in previous simulations. Wider electrodes seem to suffer more from current spreading around the point contact, leading to higher absolute offsets in the RxA values. In the limit situation that the electrodes overlap exactly with the point contact area, the offsets are expected to vanish, since a strip width that is exactly adapted to the point contact size would not allow for any current overshoot and associated voltage drop.

Conclusion

The simulations performed above lead to a set of conclusions regarding the four-probe measurement of resistance and magnetoresistance on low resistive point contact devices, along with some guidelines concerning the design of these devices. First of all, due to the positive linear slope observed in all simulated RxA curves, the intrinsic resistances of small point contacts can always be measured more accurately than those of large point contacts. For smaller point contact sizes, the absolute RxA offsets are minimized and so is the relative measurement error on the obtained resistance (see equation 5-5 of Section 5.1.2.3). Secondly, due to the increasing slope of the RxA curve for thinner and wider electrodes, both absolute and relative measurement error on the point contact resistance measured in an experiment increase as well. This error can be minimized by using thick (or highly conductive), narrow electrodes. An ideal electrode would precisely cover the point contact area, so that no current overshoot results and the resistance readings become exact. Thirdly, although the absolute error on the resistance does not depend on the intrinsic point contact RxA value (it does not change for point contacts of the same size with different intrinsic RxA), the relative error is higher for less resistive point contacts. Therefore, the resistance of highly resistive point contacts can be measured more accurately. A final important conclusion can be formulated regarding the effect of inaccurate resistance measurements on the obtained magnetoresistance figures. The MR' values will always be lower than the physical ones relating to the intrinsic point contact resistance, due to the additional, parasitic series resistance contribution to the observed total resistance. This explains the decrease of the MR' values for increasing point contact size (see Figure 5-6), which will be further elaborated in the next section. However, it is already clear that highly resistive point contacts with small lateral sizes, in combination with well-designed electrodes will produce the greatest magnetoresistance output which aids the observation of spin torque and other magnetoresistance related phenomena.

5.1.2.3. Magnetoresistance Model

In this section, the conclusions from the simulation results presented in the previous section are applied to the measured resistance and magnetoresistance data displayed in Figure 5-6. In the simulations, all RxA curves were observed to scale approximately linearly with point contact size, indicating a total device resistance R_{tot} that is composed of a constant series resistance R_S and a part that scales inversely with point contact area A. This can be seen from the following expression for R_{tot},

$$R_{tot} = R_S + R_{intrinsic} = R_S + m \cdot A^{-1} . \qquad 5\text{-}1$$

Here, R_S is a constant series resistance contribution to the total resistance, $R_{intrinsic}$ is the intrinsic resistance generated by the point contact itself, which is assumed to scale inversely with point contact area A with a proportionality factor m. In fact, m is linearly related to the point contact resistivity ρ and can be replaced by ρ·l, according to the formula of resistivity ρ,

$$\rho = R_{\text{int}\,rinsic} \cdot A \cdot l^{-1}, \tag{5-2}$$

leading to

$$R_{\text{int}\,rinsic} = \rho \cdot l \cdot A^{-1} \equiv m \cdot A^{-1}. \tag{5-3}$$

Since no physical meaning is given to the parameter l at this moment, m is remembered to scale linearly with the resistivity of the element. By multiplying equation 5-1 by A, an expression for the resistance-area product is obtained in the form

$$R_{tot} \times A = R_S \times A + m. \tag{5-4}$$

This equation indeed describes linear behavior of the $R_{tot} \times A$ product with a slope indicating the series resistance R_S and an offset m corresponding to the part of the total resistance that scales inversely with A. Now the physical meaning of the parameter m becomes apparent. It is the intrinsic RxA product associated with the point contact itself. When purely inverse scaling of point contact resistance with area A is assumed, as is done above, R_S indicates the absolute error on a measurement of the intrinsic point contact resistance, e.g. resulting from current distribution effects in the electrodes as in the previous simulations. The relative error is then given by

$$\frac{R_S}{R_{tot}} = \frac{R_S}{R_S + m \cdot A^{-1}}. \tag{5-5}$$

Model A

Considering that the measured resistance values are also observed to produce a largely linearly behaving RxA product (see Figure 5-6), a fit of this linear trend according to equation 5-4 can provide R_S and m. The result of the resistance fit is indicated by the red curve in Figure 5-16 and the resulting fit parameters are listed in Table 5-1. Note that based on a linear fit of the RxA product (not shown), a point contact with a diameter of 100 nm would have an intrinsic resistance of 4.53 Ω, which is of the same order as the nominal resistance of 4 Ω that was chosen in the simulations for an 80x80 nm^2 point contact.

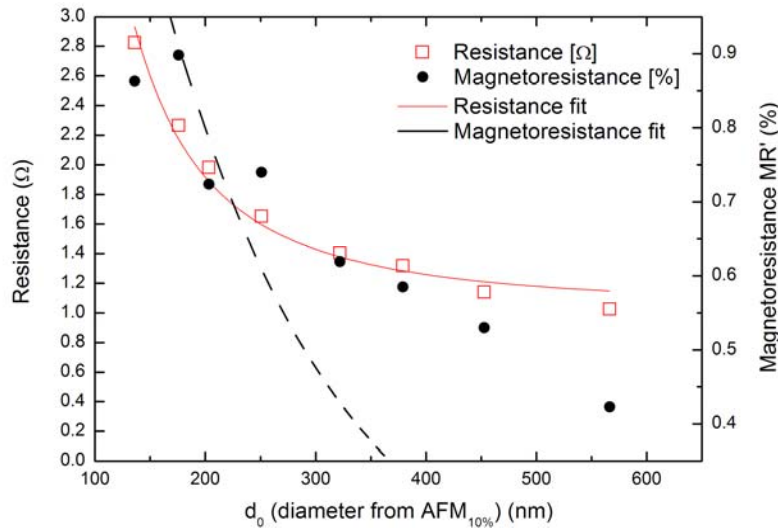

Figure 5-16: Resistance and magnetoresistance fits according to model A, which assumes a device resistance that is composed of a constant series resistance R_S and a part that scales inversely with point contact area A, according to a proportionality constant m (representing the intrinsic point contact RxA product). Although the resistance fit is relatively satisfactory, the measured magnetoresistance values MR' cannot be explained by this model, which clearly underestimates the observed magnetoresistance values.

Parameter	Fit Value
R_S	1.04 Ω
m	0.028 Ω·μm^2
MR	1.75 %

Table 5-1: Parameters R_S and m (intrinsic point contact RxA product) resulting from the resistance and magnetoresistance fits according to model A in Figure 5-16.

In the following, the relation between the observed resistance behavior and measured magnetoresistance values is further explored. First of all, assuming that only a strictly CPP magnetoresistance contribution is generated over the intrinsic point contact resistance (equation 5-3), the measured percentage of magnetoresistance, denoted by MR', can be expressed as (with MR the physical percentage of CPP magnetoresistance)

$$MR' = \frac{MR \cdot R_{intrinsic}}{R_s + R_{intrinsic}} = \frac{MR \cdot m \cdot A^{-1}}{R_s + m \cdot A^{-1}} = \frac{MR}{R_s \cdot A \cdot m^{-1} + 1} \quad (5\text{-}6)$$

This formula indicates that the measured value of MR' drops when a parasitic series resistance (R_S) is present, with the effect being more pronounced for larger R_S, larger point contacts (A) and low resistivity (m) point contacts. This prediction qualitatively

agrees with the MR’ values recorded in Figure 5-6. Note that for very big contacts (possibly combined with low point contact resistivity) the measured MR’ is expected to become very small and ultimately vanish, at least under the assumption that no CIP contribution to the magnetoresistance is generated in the leads. Using the fit parameters obtained in Table 5-1, equation (5-6) describes the expected trend for the observed percentage of magnetoresistance MR’ as a function of point contact area, based on the total resistance model (5-1). By fitting this function with the MR’ data, the physical MR percentage can be deduced. This produces MR = 1.75% for the fit indicated by the black dashed line in Figure 5-16. Clearly, the model does not reproduce the observed values of MR’, which for larger point contacts remain considerably higher than expected from the model prediction. An additional CIP contribution resulting from R_S may be responsible for the observed increased value of MR’ for the bigger contacts, as will be seen shortly.

Model B

In the previous model for the magnetoresistance, based on the linear behavior of the RxA product as a function of point contact area, any error in the determination of the point contact diameter from the AFM scans was neglected. An improved fit could include a parameter expressing a fixed offset on the point contact diameter. The point contact area A is then expressed as a function of the measured point contact diameter d_0 and an offset Δd. A fit of the measured resistances can be performed according to the formula

$$R_{tot} = R_S + m \cdot A^{-1} = R_S + \frac{m}{\pi \cdot \left(\frac{d_0 + \Delta d}{2} \right)^2} . \qquad (5\text{-}7)$$

The result of this resistance fit is shown by the red line in Figure 5-17 and the obtained values for the fit parameters R_S, m and Δd are listed in Table 5-2.

Compared with the fit parameters provided by the initial model (model A) that did not take into account a possible offset on the point contact diameters, these results indicate a slightly smaller series resistance and an increased dependence of the total resistance on the part that scales inversely with area (expressed by m). Moreover, the error on the point contact diameter indicates that the values obtained from the $AFM_{10\%}$ scans underestimate the physical point contact diameter. These results lead to a revision of the assumption made earlier about the point contact sizes obtained from the $AFM_{10\%}$ scans approximating the physical ones most accurately. Actually, returning to Figure 5-5, the diameters obtained from the SEM scans are now concluded to provide the best approximation of the physical point contact sizes.

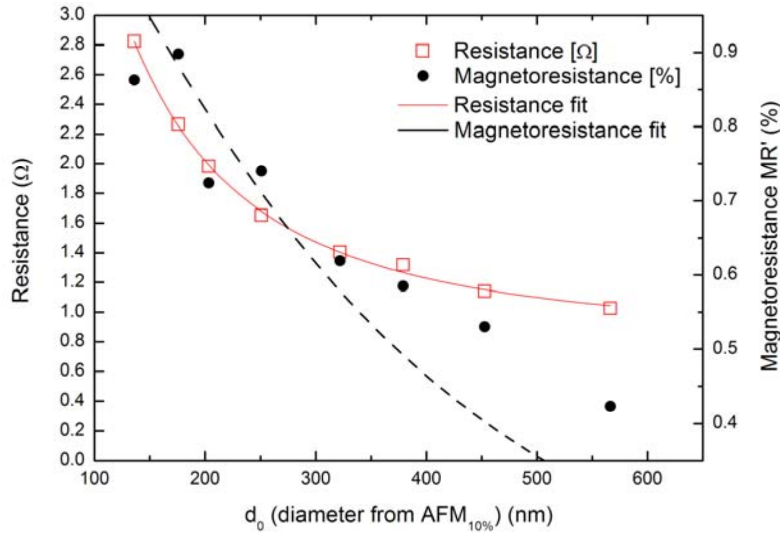

Figure 5-17: A fit of the resistance values as a function of point contact diameter obtained from $AFM_{10\%}$ scans provides the parameters R_S, m, and Δd, whose values are listed in Table 5-2. As is observed, also model B fails to produce a satisfactory fit of the observed magnetoresistance values.

Parameter	Fit Value
R_S	0.82 Ω
m	0.075 Ω μm^2
Δd	83 ± 15 nm
MR	1.38 %

Table 5-2: Values of the parameters R_S, m (intrinsic point contact RxA product), and Δd, obtained from fitting the measured resistance values as a function of point contact diameter, as shown in Figure 5-17. The physical magnetoresistance percentage MR is obtained from a fit of the observed magnetoresistance values according to model B.

The improved fit for the point contact resistances can now be used to obtain an improved fit for the MR' values, according to the following adapted form of formula (5-6):

$$MR' = \frac{MR}{R_s \cdot A \cdot m^{-1} + 1} = \frac{MR}{\frac{R_s}{m} \cdot \pi \cdot \left(\frac{d_0 + \Delta d}{2} \right)^2 + 1} . \quad (5\text{-}8)$$

The result of this fit is indicated in Figure 5-17 by the black dashed curve. Although the fit has clearly improved compared to that resulting from model A, the MR' values for larger point contacts are still not successfully recovered. According to the fit with model B, the physical MR percentage is 1.38%.

Model C

According to the previous models, the measured MR' values are supposed to become very small for big point contacts, while in reality the MR' value remains finite. This may indicate that an additional part of the total resistance is active in the generation of magnetoresistance. For example, a CIP contribution due to the series resistance R_S could add to the MR' values observed for bigger point contacts. As a further complication, only a part of R_S is expected to behave magnetoresistively, since in the fabricated devices, only the bottom electrode of the point contact device is composed of a magnetic multilayer. A reliable fit would thus require an improved model incorporating additional parameters such as the part of R_S that actually contributes to MR' and the values for the physical CPP and CIP MR values. Assuming that half of the series resistance R_S is associated with the magnetoresistive bottom electrode, the model is adapted as

$$MR' = \frac{MR_{CPP} \cdot R_{\text{int}rinsic} + MR_{CIP} \cdot \frac{R_s}{2}}{\frac{R_s}{2} + \frac{R_s}{2} + R_{\text{int}rinsic}} = \frac{MR_{CPP} + MR_{CIP} \cdot \frac{R_s}{2} \cdot A \cdot m^{-1}}{R_s \cdot A \cdot m^{-1} + 1}$$

$$= \frac{MR_{CPP} + MR_{CIP} \cdot \frac{R_s}{2m} \cdot \pi \cdot \left(\frac{d_0 + \Delta d}{2} \right)^2}{\frac{R_s}{m} \cdot \pi \cdot \left(\frac{d_0 + \Delta d}{2} \right)^2 + 1} \qquad (5\text{-}9)$$

The MR' measurement data from Figure 5-6 is now fitted with this model, employing the values obtained from the resistance fit displayed in Table 5-2. This produces a satisfactory fit (see Figure 5-18) that provides the values for the CPP magnetoresistance value associated with the point contact and the CIP magnetoresistance value associated with the series resistance generated by the bottom electrode, as displayed in Table 5-3.

Note that the MR_{CIP} value is that of the complete multilayer stack, including the non-magnetic conducting bottom electrode. Part of the current is shunted through the Cu bottom electrode and therefore does not participate in the creation of CIP GMR, explaining the relatively low value of 0.5% that is observed here. The MR_{CIP} value obtained from this model is evaluated based on an actual CIP measurement of the spin valve used in the point contact devices. This is done by measuring the magnetoresistance change on a four-probe device, sending current from the I^- to the V^- terminal, i.e. exclusively through the bottom electrode and not through the point contact (see Figure 3-8). Typical values for the measured MR_{CIP} range from 0.3 to

0.4%, which is in the order of the model forecast. Assessing the CPP GMR is much more difficult. In fact, this was exactly one of the reasons why the model was constructed, i.e. to gain an idea of the intrinsic CPP GMR of the point contact device which cannot be measured directly in the four-probe geometry. In this case, the CPP GMR value is higher than the CIP value, as is often observed, with the ratio of CPP to CIP MR being a factor 2.4.

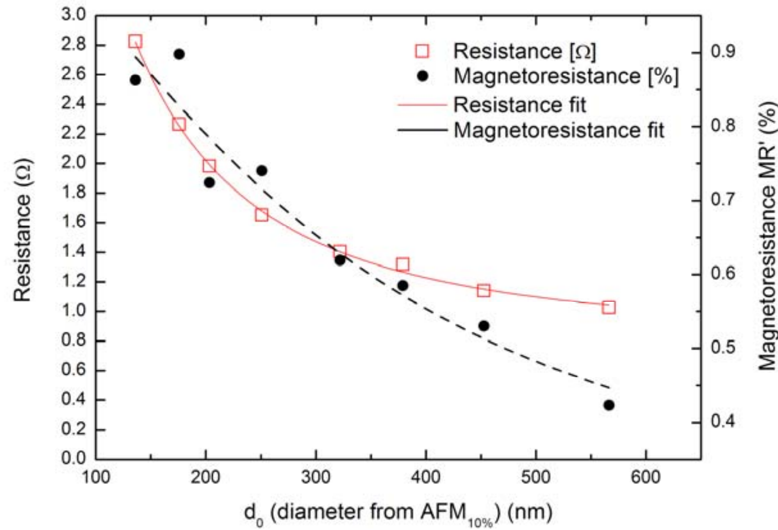

Figure 5-18: A fit of the resistance values as a function of point contact diameter obtained from $AFM_{10\%}$.scans provides the parameters R_S, m, and Δd, whose values are listed in Table 5-2. Based on these values, a fit of the MR' values according to equation (5-9) (Model C) provides the MR_{CIP} and MR_{CPP} magnetoresistance values for the electrode and point contact.

Parameter	Fit Value
MR_{CPP}	1.2 ± 0.1 %
MR_{CIP}	0.5 ± 0.1 %

Table 5-3: MR_{CPP} and MR_{CIP} values obtained from a fit with equation (5-9) (Model C) of the MR' measurement data in Figure 5-6, based on values obtained from the resistance fit displayed in Table 5-2.

In conclusion, the peculiar behavior of resistance and magnetoresistance values observed in low resistive point contact devices is understood to be due to current distribution effects in the point contact electrodes. If the total resistance is modeled as the sum of an intrinsic resistance due to the point contact (which scales inversely with point contact area) and a constant series resistance (due to the electrodes), the series resistance and point contact intrinsic RxA (m) values can be found from a fit of the total resistance values versus point contact area. Based on these parameters, together with the assumption that the additional series resistance yields a CIP contribution to the observed magnetoresistance values, a fit of the MR' values versus point contact

diameter provides the values of the physical contributions to the magnetoresistance, i.e. MR_{CIP} for the bottom electrode and MR_{CPP} for the point contact. The value for MR_{CIP} that is estimated by the model agrees fairly well with experimental observations. In addition, it was concluded that in the assessment of point contact diameter, the values obtained from the SEM scans are the most accurate, instead of the previously assumed $AFM_{10\%}$ values. Apparently the manufactured point contacts are still considerably larger than they were designed for, implying the need for further optimization to further decrease the point contact diameters. This conclusion has direct consequences in the observation of low frequency microwave emission from point contact devices, as will be discussed in the next section.

5.2. Point Contact Microwave Oscillations

The point contact nano-oscillators fabricated in this work were observed to generate microwave emission upon the application of a direct current. The setup used to assess RF emission was introduced in Section 3.4.3. The RF measurements discussed here were performed on a 100 nm (design) point contact device with a nominal resistance of 19.4 Ω due to the increased series resistance of the CPW electrodes in a two-probe measurement and featuring a magnetoresistance change of 40 mΩ at 2 mA sense current, as is displayed in Figure 5-19.

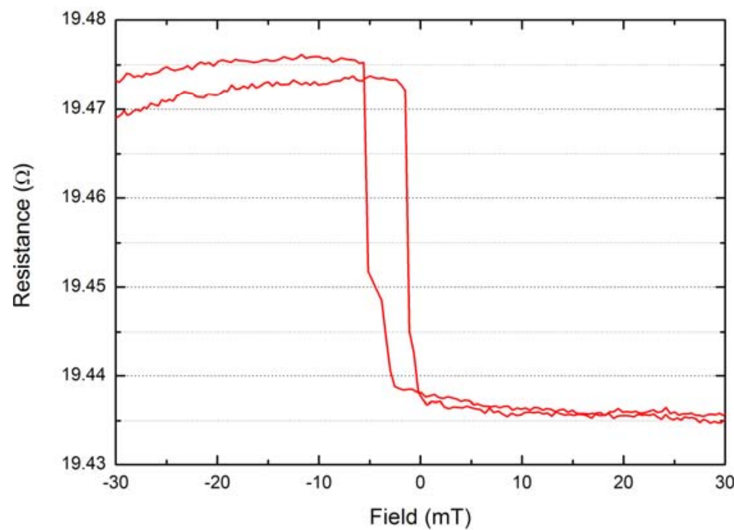

Figure 5-19: Magnetoresistance change associated with the free magnetic layer switching its direction is approximately 40 mΩ for a 100 nm point contact oscillator.

Although no convincing high frequency RF oscillations were observed on the fabricated samples, interestingly, emission was discovered in the low frequency spectrum, ranging from 200 to 400 MHz, for out-of-plane external magnetic fields (0 to 346 mT). Figure 5-20 displays a set of RF emission spectra as a function of DC

current in the 220 to 420 MHz frequency range, which were recorded for a 301 mT out-of-plane external field (i.e. perpendicular to the thin film plane). Current-tunability of the low frequency emission peaks is demonstrated as the peaks blue-shift (i.e. towards higher frequency) with increasing current. Additionally, the linewidth of the emission peaks increases considerably for increasing current. Emission is only observed for one particular direction of the current through the magnetic multilayer. Therefore, a positive current is defined to flow from the fixed to the free magnetic layer, corresponding to electrons flowing from the free to the fixed layer. For the application of an out-of-plane external field, emission was only observed for negative currents.

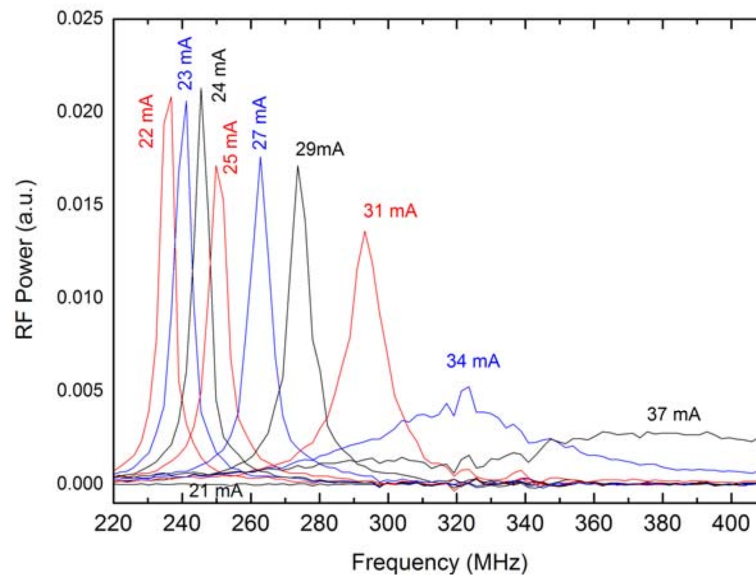

Figure 5-20: Low frequency RF power spectra of a 100 nm point contact device for a 301 mT out-of-plane field and varying negative DC current. The low frequency emission peaks shift towards higher frequencies for increasing current. At the same time, linewidth broadening of the peaks for increasing current can be observed.

Figure 5-21 displays point contact device RF emission spectra in the 200 to 1400 MHz frequency range (x-axis) for negative currents (y-axis) as a function of increasing external field (top to bottom panel). The applied field is stepped between 80, 147, 222, 301 and 346 mT. For the lowest field, no RF emission is observed (the features at 890 MHz are artifacts resulting from cellular network bleed into the measurement setup). For slightly higher fields, emission is observed with a current threshold that decreases with applied field. Harmonics of the fundamental mode are also clearly visible. For the highest field, oscillations start at currents around 22 mA. For each distinct field setting, the emission frequency increases with DC current, as was already observed in Figure 5-20. Additionally, the emission frequency seems to decrease with increasing applied field, most notably when going from 222 mT to 301 mT. Linewidth broadening is typically observed for increasing currents. Although the measurements indicate a field dependence of the threshold current related to the onset

of the dynamics, it is not easy to quantify its value due to the typical current- and field-hysteretic nature of the magnetization dynamics [47]. For example, it is observed that once the precession has been started, either or both field and current can be reduced considerably, while the dynamics pertain.

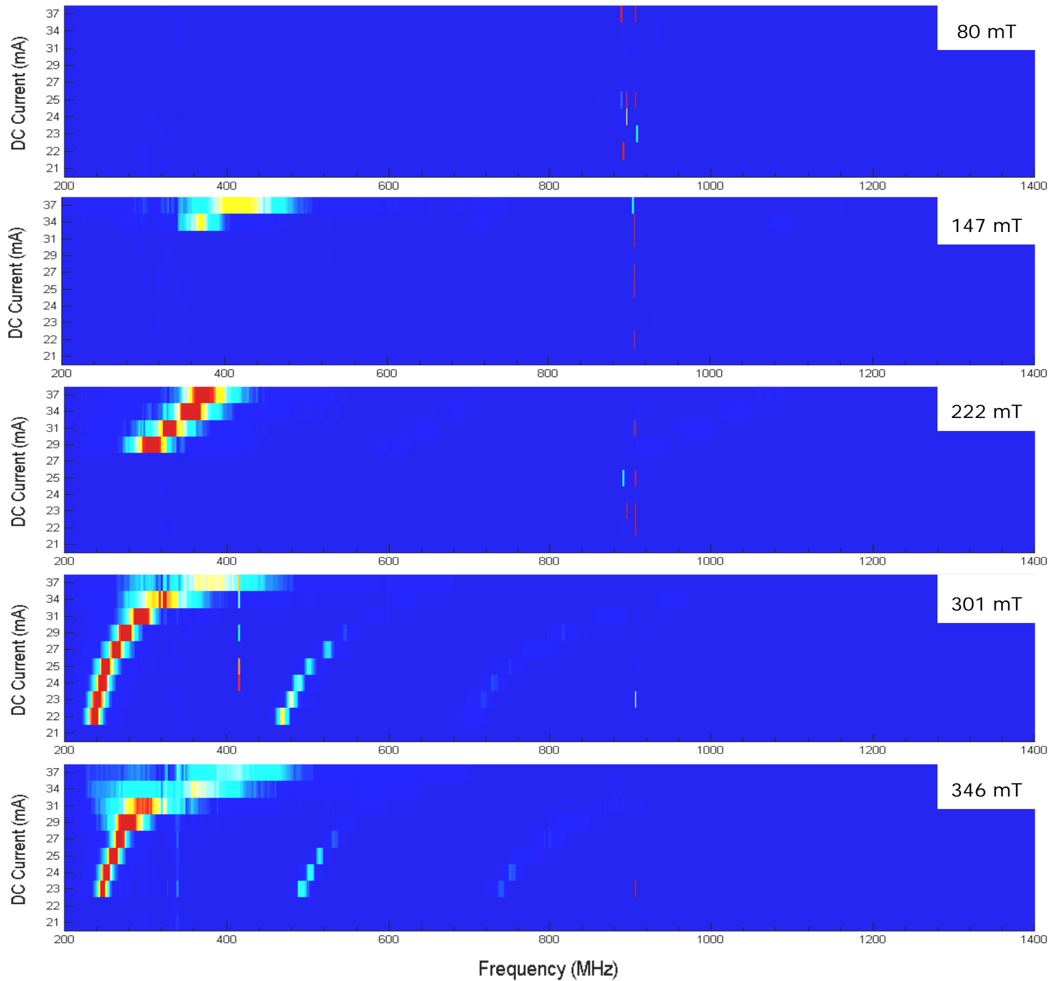

Figure 5-21: RF emission from a point contact device in the 200 to 1400 MHz frequency range as a function of applied field and DC current. In this experiment, a negative current is applied to the point contact device, corresponding to electrons flowing from the fixed to the free magnetic layer. The field is applied out-of-plane and is varied from top to bottom between 80, 147, 222, 301 and 346 mT. For the lowest field, no RF emission is observed, while for higher fields, a current threshold is noticed. For the highest fields, oscillations start at currents around 22 mA. The emission frequency seems to decrease with applied field, featuring additional broadening of the high current peaks for the highest field value.

The observation of low frequency dynamics in point contact devices is relatively new and has only recently also been reported by another group [47]. However, the suspected mechanism that causes the low frequency oscillations is thought to be understood for some time from predictions [48] and observations [49][50] of the gyrotropic motion of a vortex core in patterned micrometer size NiFe disks.

According to micro-magnetic simulations, a spin-transfer current is also able to move a vortex core around its equilibrium position [51], which supports that the observed low frequency oscillations may indeed be due to the current-driven motion of a vortex core domain state under the point contact area.

Although emission in the higher frequency range may be more interesting for the application of point contact devices in wireless applications, especially when the observation of spin waves in optical BLS experiments is aimed for, the current samples only revealed interesting phenomena in the low frequency range. It is suggested that the low frequency vortex modes dominate in the current samples, due to the larger than expected point contact sizes (and thus, increased Oersted fields, which act as a restoring force for the non-uniform vortex mode). Consequently, to eliminate these vortex modes, the point contact fabrication process should be further refined to deliver smaller point contacts. This may require the consideration of a different etching technique, or the existing PMMA process should be further optimized. The combination of a thinner SiO_2 passivation layer and a thinner resist layer (currently 300 nm PMMA) could increase the resolution of the definition process and improve the point contact sizes, so that eventually the low frequency vortex oscillations can be suppressed in favor of high frequency phenomena.

5.3. Brillouin Light Scattering from Spin Waves

One of the primary goals of this thesis was to provide point contact nano-oscillator devices featuring optical access to the extended magnetic layer around the active point contact area, in order to enable the study of spin wave emission with the Brillouin light scattering technique. This technique uses a focused laser spot to probe the free magnetic layer around the point contact. The interest for the study of spin wave emission is triggered by the fact that these spin waves may provide a coupling mechanism for the frequency and phase locking of multiple point contact nano-oscillators [18]. Eventually, this could enable the construction of an array of mode locked oscillators that produces a considerable increase in RF output power compared to a single oscillator design [16]. The following sections consider the nano-oscillator devices that were designed with CPW top electrodes ending in a very narrow tip above the point contact (see Figure 4-1-c). The tip dimensions are maintained very small to allow the focused laser spot in the Brillouin light scattering setup (approximately 300 nm in diameter) to probe the free magnetic layer as close to the point contact as possible. The design of the tip was evaluated through basic electrical measurements combined with SEM and optical imaging in Section 4.2.3. This section presents a number of interesting preliminary results from the Brillouin light scattering (BLS) experiments that aim to study spin wave emission from a point contact and associated power decay into the extended magnetic layer around the excitation area.

The experiments were performed in collaboration with the University of Kaiserslautern. A short description of the experimental setup available there is provided in Section 3.4.4. Note that, due to the limitations on the current that can be sent through the present devices, the spin waves are excited through the application of an RF current, rather than using a DC current. The effect of applied field strength and RF excitation frequency is studied and spatial scans of the power decay of the magnetization dynamics away from the point contact into the extended free layer are presented. Due to the extremely complicated interplay of device geometry, external and internal bias and Oersted fields, the dispersive nature of the magnetostatic mode propagation and possible quantization of the modes, the currently available set of experimental data should be seriously expanded to enable a complete understanding of the partial observations presented here. Although the limited results from this ongoing research may not yet enable definitive conclusions to be drawn, some interesting phenomena could be observed concerning spin wave emission in the free layer. Through the presentation of these measurements, this section thereby demonstrates the power of optical BLS measurements as a tool in the analysis and understanding of synchronization phenomena in spin torque nano-oscillators.

5.3.1. Thermally and DC Excited Magnetization Dynamics

A first experiment aimed to collect the intensity spectrum of thermally excited spin waves (without RF excitation). However, no BLS signal was found, which is possibly due to excessive absorption of light in the SiO_2 layer that caps the free $Ni_{80}Fe_{20}$ layer. Subsequently, a DC current was applied to the devices to verify whether direct current induced spin waves could be generated. However, although there was some variability between devices, all of them were destroyed for currents below 40 mA and no direct current generated spin wave emission could be observed. From the microwave RF experiments in Section 5.2, the typical critical current density required to start direct current induced low frequency RF emission, i.e. to start spin torque driven vortex oscillations of the free layer magnetization, is known to be approximately 25 mA for the smallest point contact size, while limited high frequency spin current induced phenomena could only be observed for substantially larger currents (over 45 mA). In conclusion, the early breakdown of the tips for relatively low currents and the strong vortex mode generation due to large point contact sizes as such currently impede the execution of BLS experiments that are to show direct current induced high frequency spin torque driven spin wave emission from a point contact into the free magnetic layer. Although direct current excitation of high frequency dynamics seems impossible at present, spin waves can still be resonantly excited through the application of an RF AC current. In the following experiments, this is the way spin wave emission from the point contacts will be generated.

5.3.2. RF Excited Magnetization Dynamics

In the following experiments, the micro-focus laser spot probes the magnetization dynamics at a location approximately 1 μm away from the point contact tip, as indicated by the arrow in Figure 5-22, showing a BLS tip connecting to a 200 nm point contact. To obtain an idea of the possible modes that can be excited, the device is electrically pumped with a 13 dBm RF AC current of varying frequency to check for resonances in the BLS intensity spectrum. BLS intensity spectra were recorded for various strengths of the external magnetic field that is applied in the plane of the magnetic layer, along the long axis of the magnetic element, which is to the right in Figure 5-22. In Figure 5-23, the frequency of the RF excitation source is swept between 3.0 GHz and 18.0 GHz (x-axis), while for every excitation frequency, a BLS intensity spectrum is recorded and mapped in color scale as a function of the BLS scan frequency (y-axis). From the information in these images, integrated BLS intensity spectra can be calculated as a function of external field, which are displayed in Figure 5-24.

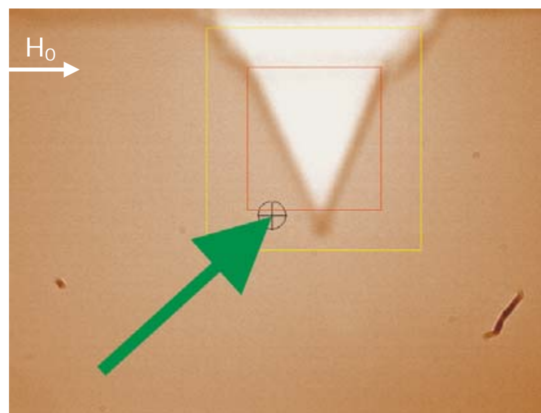

Figure 5-22: Image of a BLS tip connecting to a point contact. The circle indicates the location where the laser spot is focused on the free magnetic layer to obtain the BLS intensity spectra (approximately 1 μm to the left of the point contact).

For zero applied field, the system is observed to display a resonance around 8 GHz, which is visible both in the intensity maps (resonance indicated by the red area in the left panel of Figure 5-23-d) and in the integrated BLS intensity spectrum (resonance peak in the purple line in Figure 5-27). With increasing field, the resonance peak observed at 8 GHz for zero field red-shifts towards lower frequencies, while an additional lower frequency peak initially around 3 GHz is observed to blue-shift towards higher frequencies. The integrated BLS spectrum for the largest applied field (18.5 mT - blue line) features a hybrid peak that is composed of contributions of the high frequency mode with both its second harmonic and the previously observed lower frequency mode. (see Figure 5-23-a). Although the higher order peak at 4.9 GHz and the red-shifting peak at 5.7 GHz partly overlap for the maximum field value, they remain distinguishable. The lowest frequency peak, whose frequency increases

with increasing external field, is assumed to be due to excitation of the uniform dynamic mode, while the higher order peak is suspected to represent a spin wave mode, possibly the MSBVW one, considering the field geometry and the location of measurement.

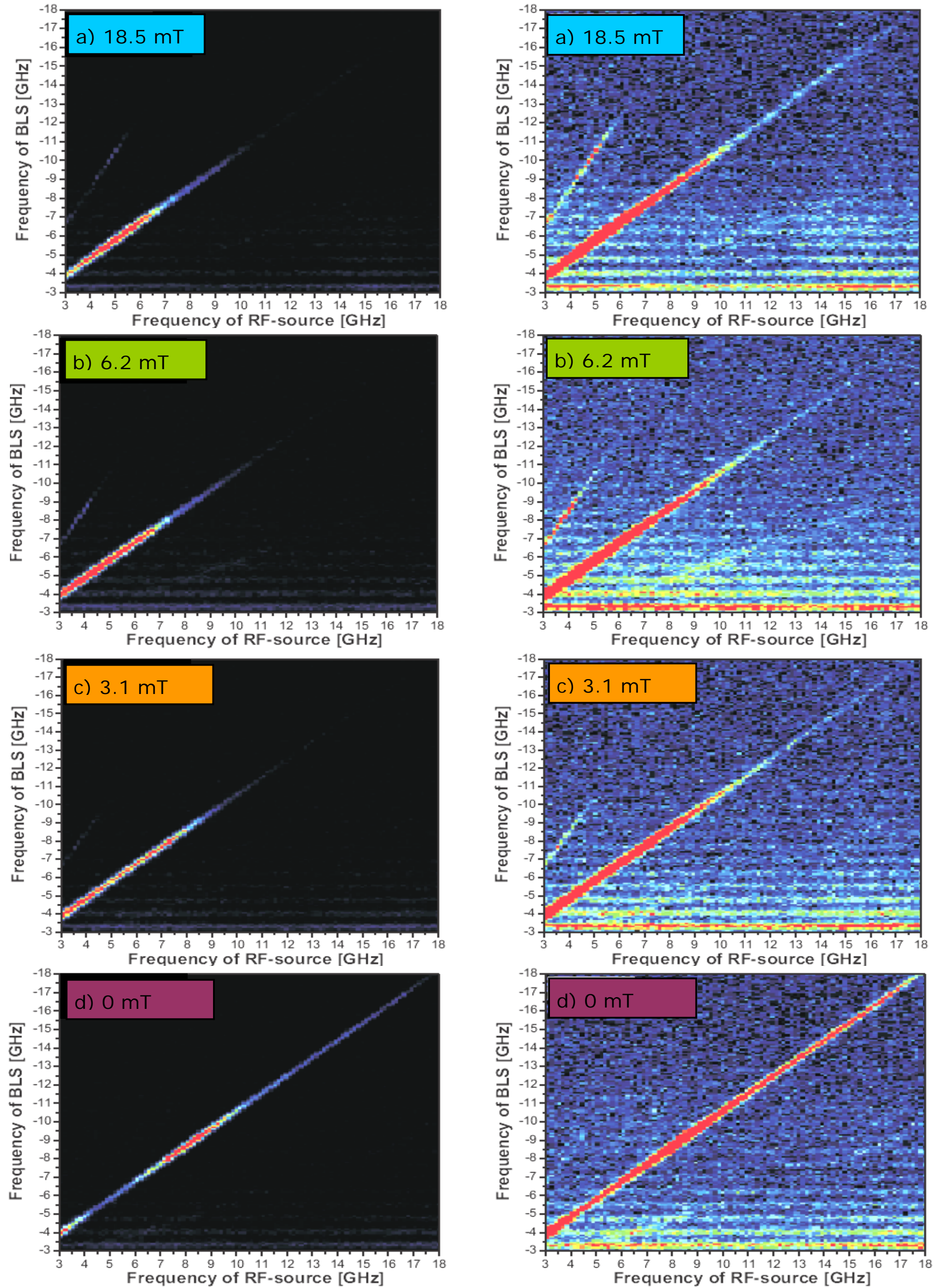

Figure 5-23: Logarithmic (left) and linear scale (right) BLS spectral intensity (y-axis) maps as a function of RF excitation frequency (x-axis). The externally applied field is increased from bottom (d) to top (a). The corresponding integrated BLS intensity spectra are displayed in Figure 5-24.

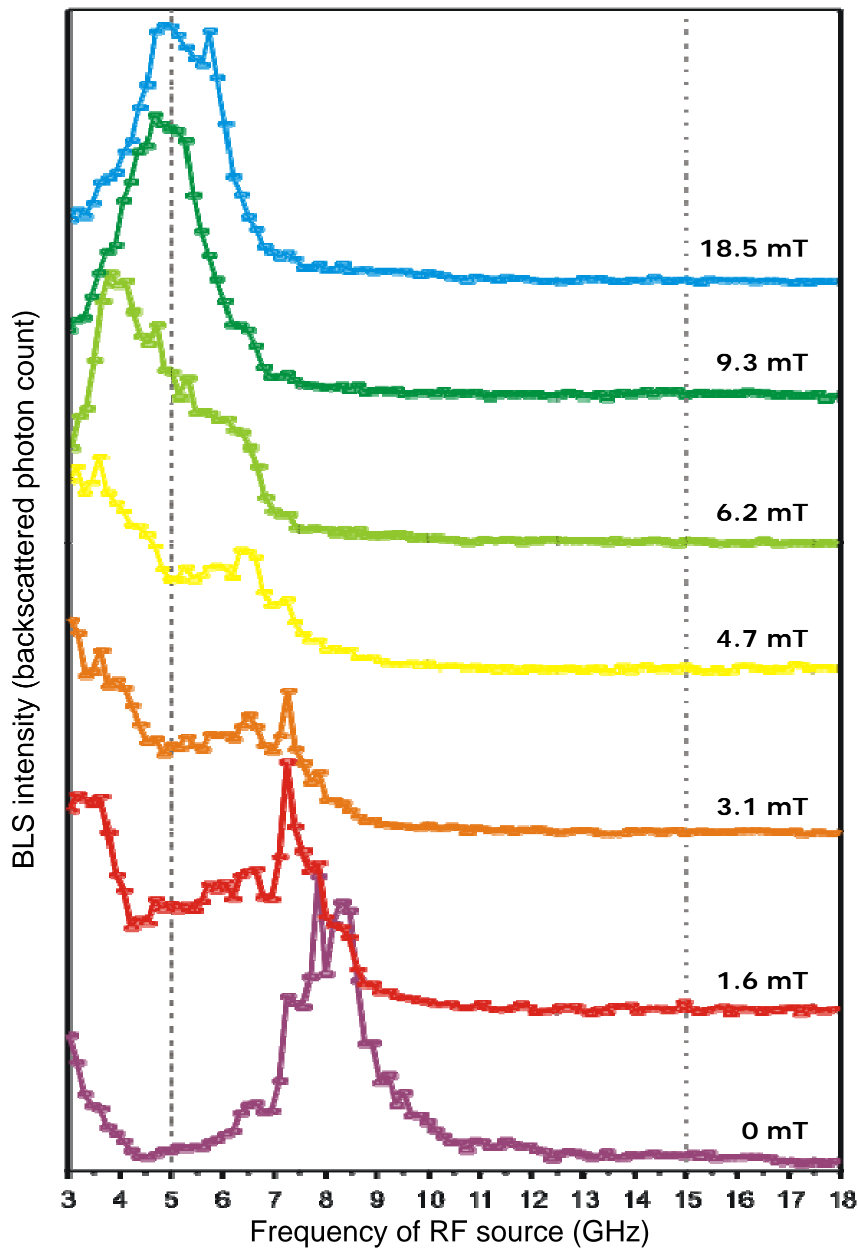

Figure 5-24: Integrated BLS spectra as a function of RF excitation frequency for various external field values. The externally applied field is increased from bottom (0 mT - purple line) to top (18.5 mT - blue line).

For intermediate fields, the peaks overlap, resulting in the highest integrated intensity peak (dark green curve) for a pumping frequency around 4.9 GHz. For an appropriate field setting, both modes are pumped effectively at a common frequency. Note that in all integrated spectra, a smaller peak is observable around 6.5 GHz, which is not assumed to be related to any magnetic phenomenon, since it does not shift with varying external field. This small ripple is instead assumed to be caused by RF transmission effects in either the device or cabling. The spectral maps in Figure 5-23 also reveal a set of horizontal, equally spaced lines. These are an artifact of the multi-mode laser cavity resonances of the laser that probes the sample.

The red-shifting behavior of the suspected MSBVW mode in the integrated BLS intensity spectra remains somewhat puzzling. Note that also in the case of the MSBVW mode, frequency is expected to increase with increasing field, equation (2-35), unless the external field is able to lift any other anisotropy present in the system, by which the total internal field, and thus the frequency of the MSBVW mode could decrease. Although the free layer may experience slight stray field induced anisotropy due to the bottom exchange pinned layer, this interaction is expected to be an order of magnitude smaller than the external 18 mT field (see for example the magnetoresistance curve in Figure 5-7). Furthermore, if indeed the internal field would be lowered by the application of the external field, also the uniform mode frequency should go down, which is not the case.

A cautious hypothesis is formulated here that the red-shift could be caused by the interplay between the Oersted field generated by the excitation current and the externally applied field, in such a manner that the net local field at the place of measurement changes its direction from vertical to horizontal. This generates a local transition from MSSW to MSBVW mode behavior, implying a decrease in frequency. Using the formula for the Oersted field of an infinitely long current carrying wire, the maximal field amplitude obtained at 1 μm away from the point contact is of the order of 7 mT, which is in the range of the applied fields and strong enough to cause tilting of the net internal magnetic field. Note that this reasoning is slightly complicated by the simultaneous effect of increasing overall frequency for both modes due to increasing field. A full quantitative argument would require precise fitting of the peak frequencies and the calculation of hybrid MSSW and MSBVW mode dispersion relations for the various angles of propagation.

To gain more insight into the observed resonances, the measurement of the BLS intensity as a function of excitation frequency is repeated for the zero and maximum field settings of the previous measurements. In order to increase the BLS signal, especially for the higher frequency modes which are known to decay faster, the laser spot is positioned closer to the point contact. The resulting BLS frequency versus RF excitation frequency maps for 0 mT and 18.5 mT in-plane fields, Figure 5-25, reveal increased detail compared to the previous measurements. Up to five harmonic modes are now observable above the main excitation frequency, along with two modes with 0.5 and 1.5 times the excitation frequency. These non-integer factor modes are assumed to be associated with magnon splitting processes. Note that in the case of an applied field, the splitting process seem to be prohibited below a threshold excitation frequency close to 8 GHz, indicated by the abrupt onset of both the 0.5 and 1.5 line at this frequency. Apparently, the splitting process cannot produce spin waves with a frequency less than approximately 4 GHz. This threshold can be explained by looking at the magnetostatic mode dispersion curves displayed in Figure 5-26, which are

calculated for a 10 nm thick permalloy film and an in-plane bias field of 20 mT. In these figures, subsequent curves indicate the transition from MSSW (top) to MSBVW (bottom) behavior, or alternatively, the wave vector changing its direction from perpendicular to parallel to the external field. Clearly, neither the MSSW nor the MSBVW mode can exist below the uniform mode frequency (in principle, the MSBVW mode can exist below this frequency, but the dipolar contribution to the dispersion curve is very small for very thin films). Finally, note that for zero applied field, no magnon splitting is observed between 11 GHz and 14 GHz, which cannot be explained so far.

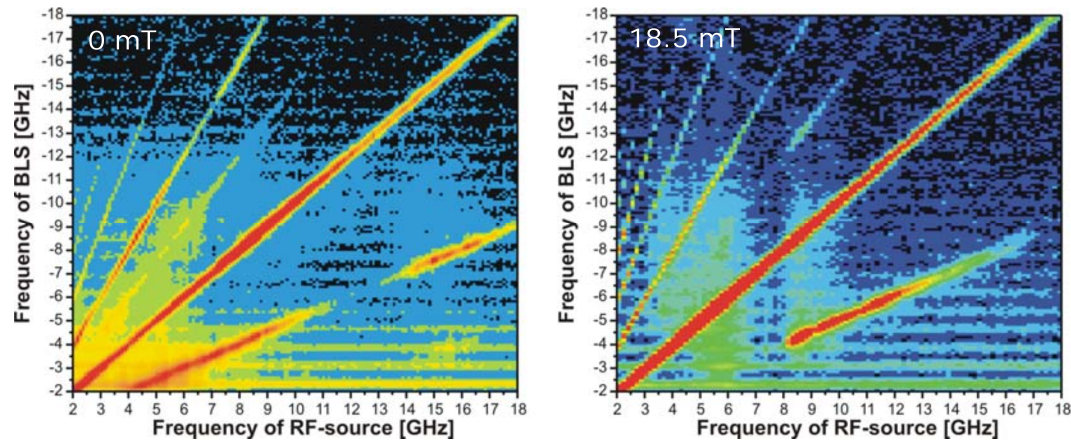

Figure 5-25: Logarithmic scale BLS spectral intensity (y-axis) maps as a function of RF excitation frequency (x-axis, RF power 13dBm) for an externally applied in-plane field of 0 mT (left) and 18.5 mT (right). For the 18.5 mT field, the magnon splitting process is prohibited to produce magnons below approximately 4 GHz (i.e. excitation frequency 8 GHz).

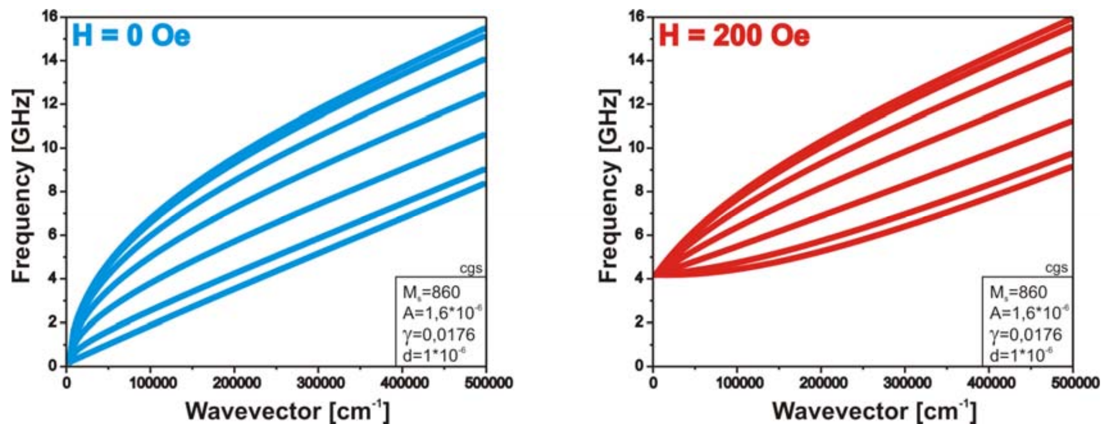

Figure 5-26: Effect of the application of an external field on the dispersion relations. In each figure, the top curve corresponds to the MSBVW mode, while the bottom curve represents the MSSW mode. The dispersion curves in between are for 15, 30, 45, 60 and 75 degrees angles between the wave vector and external field. Clearly, for a 200 Oe field the magnon splitting process is prohibited for generating magnons with a frequency below 4 GHz. Calculation provided by H. Schultheiß.

5.3.3. Spatially Resolved Spin Wave Decay

In Figure 5-24, a resonance peak was observed for an excitation frequency around 8 GHz and zero applied field. On the other hand, for the maximal applied field of 18.5 mT, the dynamics seemed to be located around 4 GHz. These two resonances are now investigated in more detail. First, the system is excited in the absence of an external field at 7.0 GHz (slightly below resonance), 8.0 GHz (resonance frequency) and 9.0 GHz (slightly above resonance). The resulting spatial intensity maps, integrated in the frequency intervals associated with the main (top figures), second harmonic (middle figures) and half harmonic (bottom figures) are displayed in Figure 5-28. Note that no second harmonic is presented for the 9.0 GHz excitation, as it falls outside the interferometer measurement range. For each integration interval, the left picture displays the BLS intensity in a linear scale, while the right picture provides the same information on a logarithmic scale. Apart from the reduced intensity in the triangular area on top, due to blocking of the electrode tip, the spin wave radiation for the main mode is clearly anisotropic with a preferred horizontal direction of radiation. Both the half and second harmonic modes are strongly localized within the point contact area.

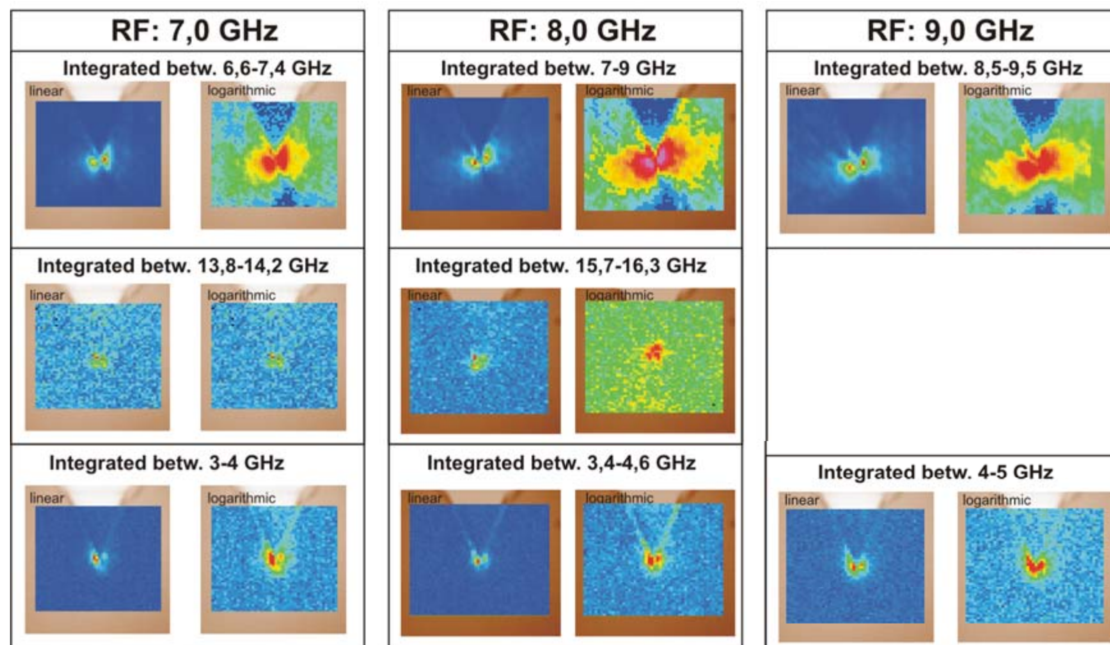

Figure 5-27: BLS spatial intensity maps show RF-excited spin dynamics in the free magnetic layer around the point contact for zero applied field. The system is excited at frequencies at, below and above its resonance frequency. The main mode radiation profiles are clearly anisotropic, while both higher and lower modes appear to be more localized in the vicinity of the point contact.

Secondly, the procedure is repeated with the application of an 18.5 mT external field. In this case, the system is excited at 4.2 GHz, 4.9 GHz and 5.7 GHz, while the

integration intervals for the main and second harmonic are adapted to appropriate frequencies. The resulting spatial intensity maps are displayed in Figure 5-27. Note that the half frequency mode is no longer displayed, since the magnon splitting process is prohibited at this excitation frequency.

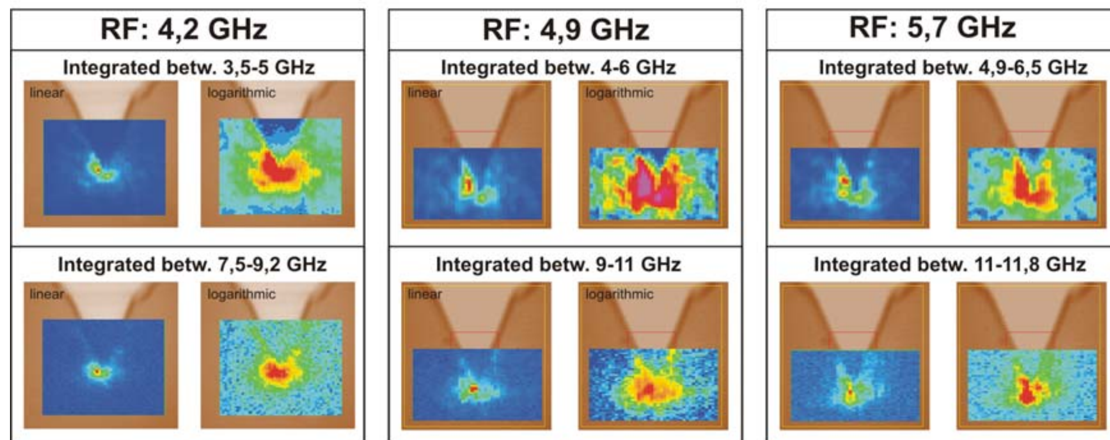

Figure 5-28: BLS spatial intensity maps show RF-excited spin dynamics in the free magnetic layer around the point contact for an 18.5 mT field applied in the horizontal x-direction. The system is excited at frequencies at, below and above its resonance frequency, leading to symmetric radiation of the normal mode and its second harmonic in the magnetic layer around the point contact.

When comparing the results of the experiments without and with an external field, the radiation pattern integrated around the excitation frequency was clearly quite anisotropic when no external field was present, while it becomes much more symmetric in the case with external field. Now both the main and second harmonic mode are observed to be quite isotropic and the second harmonic mode is obviously much less localized in the point contact area. At present it is not completely clear in which way the application of an external 18.5 mT field can lift the anisotropy which is present for zero field, nor where the zero field anisotropy originates from. The simulations performed in the next section reveal anisotropic radiation that displays similarity with the one observed here. In the simulations, the anisotropic behavior will be shown to originate from a geometrical effect combined with the dispersive nature of the spin wave propagation that strongly confines a single spin wave mode to the point contact area. Although no definitive conclusion will be drawn here, the spatial intensity maps for zero field show considerable intensity near the point contact for integration intervals centered at half and double the excitation frequency, indicating a stronger localization of the dynamics near the point contact area, which could indicate a similar effect as recovered in the simulations (see, for example Figure 6-18 for 36 GHz). Although quite some questions remain to be answered at this moment, it is clear that progress has been made in enabling the study of spin wave emission from point contact nano-oscillators in an extended magnetic free layer through the optical

BLS technique. Upon further optimization of the point contact devices (smaller point contacts and slightly wider top electrode) it is hoped that the study can be extended to direct current induced dynamics.

6. Micro-Magnetic Spin Wave Modeling

6.1. Introduction

To gain a deeper insight into the magnetization dynamics associated with spin torque nano-oscillators in the point contact geometry with an extended magnetic layer, micro-magnetic numerical simulations have been carried out. The emission and propagation of spin waves in this layer is given particular attention, since spin waves have been identified as a possible coupling mechanism for the synchronization of multiple point contact nano-oscillators. The spin waves originate from spin torque induced magnetization dynamics in the area under the point contact upon application of a direct current. Synchronization then proceeds through the frequency and phase locking of multiple oscillators and results in an increase of the total emitted power if the oscillators resonate in phase [17][18][19]. From the physical point of view, it is interesting to characterize the wavelengths, phase and group velocities of the spin waves, together with the dispersion relations that define the various modes of propagation. Specifically, particular modes of spin wave propagation may be observed, depending on the orientation of an externally applied magnetic field, as was explained in Section 2.4. Moreover, it is interesting to know over which range magnetic excitations can travel in a thin film layer. The associated spatial power decay is an important factor in experiments that are to prove oscillator locking, as it provides an indication as to how close point contacts should be spaced in order to experience sufficient coupling for synchronization. From the design point of view, this information can be used to determine limits on the physical spacing of multiple point contacts in synchronization experiments. In conclusion, not only can simulations provide an expansion of parameter space available experimentally, they can also guide the designer of spin torque nano-oscillators towards devices with favorable properties, tailored to the type of experiments to be performed, such as those concerning synchronization of multiple point contact oscillators or BLS experiments which require optical access to the region of a free magnetic layer where spin waves exist.

In the following, spin wave emission is studied through micro-magnetic simulations of a magnetic thin film using the public-domain OOMMF micro-magnetic simulation environment, which is fully introduced in Section 6.1.1. Physically, the spin waves of interest originate from spin torque driven magnetization dynamics in the area under a point contact upon application of a direct current. In the simulations, however, these magnetization dynamics will be artificially reproduced by the application of an oscillating magnetic field, localized in the magnetic layer under the point contact. This approach is discussed in more detail in Section 6.1.2. The simulation results are

further divided into two sections. Section 6.2 considers whether the situation of interest can be translated into a one-dimensional problem that reproduces analytically known solutions of spin wave propagation in an extended thin film. When this is the case, one-dimensional simulations provide a fast and easy way of analyzing some aspects of spin wave propagation. In Section 6.3, a limited number of two-dimensional simulations are performed to enable comparison with the solutions of the one-dimensional setting. Finally, Section 6.4 presents the conclusions that generate from the performed simulations, together with an outlook that discusses further opportunities for continued simulations.

6.1.1. OOMMF

The Object-Oriented Micro-Magnetic Framework (OOMMF) is a public domain micro-magnetic simulations program developed at the National Institute of Standards and Technology (NIST) that can be used to simulate the magnetization dynamics of various magnetic structures [52]. The OOMMF program is object-oriented, which means that it can be extended with custom, user-definable functions and classes. This way, the program is capable of performing both two- and three-dimensional simulations of a wide range of geometries, while it can be expanded at wish with user-defined modules that introduce specific parts to the dynamic equation, such as the spin torque term described by equation (2-25) in Section 2.3.1.3.

The general working principle behind OOMMF is now discussed. In general, micro-magnetic simulations proceed by the space and time discretization of a magnetic problem. The space discretization is imposed by the definition of a geometric mesh that breaks up the simulated geometry into discrete units of magnetization which are considered macro-spins on the microscopic level. The dynamics of these macro-spins are described by the Landau-Lifshitz-Gilbert-Slonzcewski (LLGS) equation of motion, which was introduced as equation (2-26) in Section 2.3.1.3. OOMMF imposes rectangular meshing with cells that have a length, width and height on the nanometer scale. When the problem geometry and initial state have been defined, magnetization dynamics are simulated through integration of the LLGS dynamic equation of motion using a fourth-order Runge-Kutta algorithm with time step control. During every subsequent iteration, a new magnetic configuration is calculated based on the previous one that was passed to the program, complying with the energy error and time step constraints imposed by the user. OOMMF can be programmed to save the subsequent magnetic configurations to disk for visualization and analysis of the magnetization dynamics.

Although the OOMMF package proves to be a very powerful tool in the investigation of magnetization dynamics, it does currently lack some features that are available in

other (commercial) packages. For example, OOMMF uses a rectangular spatial discretization grid as standard, while other packages offer the possibility of non-uniform grid definition in various geometries, such as the triangular one. Also, when inducing spin torque into a certain volume of magnetic material, using the current OOMMF spin torque module, the Oersted field associated with the current distribution is not directly accounted for. However, in principle OOMMF does allow this Oersted field to be programmed separately through advanced scripting. In particular, the Oersted field is believed to be responsible for the creation of vortex-like domain structures in point contacts which can lead to complicated magnetization dynamics, such as the low frequency oscillations that were observed in Section 5.2. Although a complete physical picture certainly requires these effects to be included, much can be learned about the basic spin wave propagation properties of the system in a simplified context that temporarily omits these contributions to the magnetization dynamics.

6.1.2. Local Excitation of a Magnetic Film

As stated before, spin wave emission from a point contact spin torque nano-oscillator into an extended thin film originates from spin torque driven magnetization dynamics in the area under the point contact upon application of a direct current. Due to the localization of the current-induced magnetization dynamics in the small area under the point contact, it is expected that the propagation of spin waves far away from the point contact is only marginally affected by the way they are being generated locally. Therefore, in the following simulations, the magnetization dynamics will be artificially produced by the application of a local oscillating magnetic field in the area under the point contact. Local excitation of a magnetic thin film has been reported before as an artificial way to generate and study spin waves [55]. However, the results obtained from this kind of simulations should be interpreted with extreme care, as they do not always deliver a completely correct representation of all quantities involved [56]. Although the method of local field excitation may not fully capture some of the intricate physics of spin torque excitations, such as those associated with particular current distribution effects, the study of spin waves generated by the application of an artificial, local field may enable the characterization of some basic properties of spin wave emission and propagation in the studied magnetic thin film elements. In a later stage, the spin torque action may be included in the spin wave generation to verify its additional effect on spin wave emission and propagation.

6.1.3. Spin Wave Propagation

The theory associated with dipolar-exchange spin wave propagation was introduced in Section 2.4. The geometries for external field and wave vector associated with the

MMSW, MSBVW and MSFVW modes of propagation are repeated here in Figure 6-1. Only the in-plane MSSW and MSBVW modes will be considered in the following simulations, since the in-plane application of a field is the most common geometry in experiments, including the optical BLS setup which probes spin waves through the inelastic scattering of light. Assessing the out-of-plane modes in an experimental setup is more difficult because of the high saturation fields required to realize a completely out-of-plane magnetization of the thin film and due to the fact that the devices have to remain optically accessible to the BLS laser spot in a backscattering geometry.

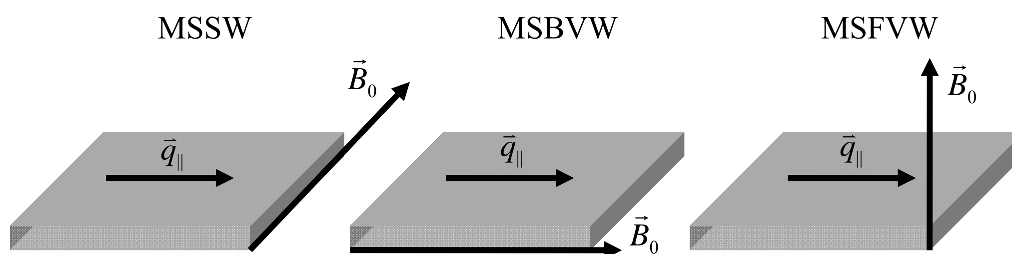

Figure 6-1: MSSW, MSBVW and MSFVW magnetostatic mode geometries of in-plane wave-vector ($\vec{q}_{||}$) and externally applied field ($\vec{B}_0$) for spin wave propagation in an extended magnetic thin film.

6.2. One-Dimensional Simulations

Although fully three-dimensional dense grid simulations may provide the most complete and detailed picture of a magnetic problem, processing requirements make these simulations very time consuming to run in standard computing environments, especially when a large parameter space is to be explored. Therefore, in the following, it is investigated whether the problem of spin wave emission from a point contact into an extended magnetic thin film can be translated into a one-dimensional setting that reproduces analytically known solutions of spin wave propagation. If the relevant properties of the higher dimensional case can be successfully recovered, one-dimensional simulations provide a convenient way of analyzing spin wave propagation with only limited computing resources, enabling large numbers of simulations to be performed easily and quickly.

In the following simulations, only the free magnetic layer of the spin valve stack is considered and any effective field contribution due to the exchange-biased fixed magnetic layer is not taken into account. When this coupling is neglected and very thin layers are assumed (like the ones used in point contact oscillator devices), the original physical problem, which is formally three-dimensional, can be regarded as quasi two-dimensional. Note that all simulations to be discussed in the following

sections (both the 'one-dimensional' as well as the 'two-dimensional' simulations) are in fact performed in a three-dimensional simulation environment. The terms 'one-dimensional' and 'two-dimensional' therefore relate to the dimensionality of the spin wave propagation, being along a single direction in the one-dimensional case, and in any combination of two orthogonal in-plane directions in the two-dimensional case. Furthermore, since the spin waves are being generated by the local application of a magnetic field, no Oersted field associated with the current flowing through the point contact is taken into account. Finally, the simulations are performed in the assumption of zero temperature.

First, the results from the one-dimensional simulations are validated by comparison with known analytical expressions that describe spin wave propagation in an infinite thin film. The effect of film thickness and diameter of the excitation area (i.e. the point contact area) on the mode dispersion curves and power emission into the free layer is investigated. In Section 6.3 these findings will be subjected to further comparison with the results of two-dimensional thin film simulations.

6.2.1. Simulation Geometry and Parameters

This section discusses the geometry adapted in the one-dimensional simulations, along with the magnetic and material parameters governing the problem. To enable the study of spin wave propagation in a one-dimensional setting, a chain of square cells was first constructed as shown in Figure 6-2. The local excitation field is applied within the first cell at the left, which has a different color than the rest of the chain.

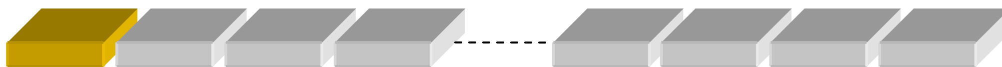

Figure 6-2: A one-dimensional array of square cells results in a structure that exhibits strong axial shape anisotropy. Therefore, this system does not resemble the situation of an infinitely extending thin film.

This geometry, which actually represents a one-dimensional magnetic wire, was observed to display strong shape anisotropy along its axial direction. This is an important difference with the extended thin film problem that is to be studied, since in an infinite thin film, for which the modes are analytically known, no such anisotropy should be present. In fabricated devices, patterning-induced shape anisotropy effects may alter the spin wave dynamics compared to the analytical solutions for the infinite thin film, expressed through additional contributions to the effective field term in the LLGS equation (2-26). The exact form of the contribution is determined by the aspect ratio of the element, the fact if the element is in a single or multiple domain state, the

crystalline anisotropy of the material and the presence of stray field coupling from the exchange-biased layer. Since principal interest goes out to the extended magnetic thin film problem, the discretization cell sizes were adapted towards a simulation geometry that, while remaining one-dimensional, resembles the thin film situation better. Therefore, the thin film is modeled by a one-dimensional array of elongated rectangular cells as indicated in Figure 6-3. The discretization cell dimensions are chosen such that the height ($\hat{z}$–direction) resembles film thickness, the width ($\hat{x}$–direction) is small enough for adequate sampling of the spatial variation of the magnetization in the spin wave propagation direction (along the $\hat{x}$–axis) and the length ($\hat{y}$–direction) is large enough so that the set of cells making up the total structure resembles the geometry of a thin film (extended in the two lateral dimensions and bound in the third). From preliminary spin wave excitation simulations in a 5000x5000x5 nm^3 film, it was concluded that a cell width in the order of 5 to 20 nm is sufficient for spatial sampling of the spin waves for excitation frequencies in the GHz range. The length of the grid cell was chosen equal to the total length of the structure in the $\hat{x}$–direction, so that a square problem geometry results. The resulting structure was verified to resemble the thin film situation with respect to shape anisotropy and magnetization uniformity. The previously obvious hard axis behavior was reduced appreciably and upon the application of a 200 mT saturation field, the magnetization is largely uniform, with only small deviations due to demagnetization effects at the left and right edges. This should form no problem when the spin waves are being studied at sufficient distances away from the edges. Note that in the one-dimensional array of elongated cells, magnetization waves can only propagate in the $\hat{x}$–direction. By applying an external saturation field in the appropriate direction, the analytically known dipolar-exchange modes can be studied by comparing the results obtained from the simulations with the known analytical solutions presented in Section 2.4.2.

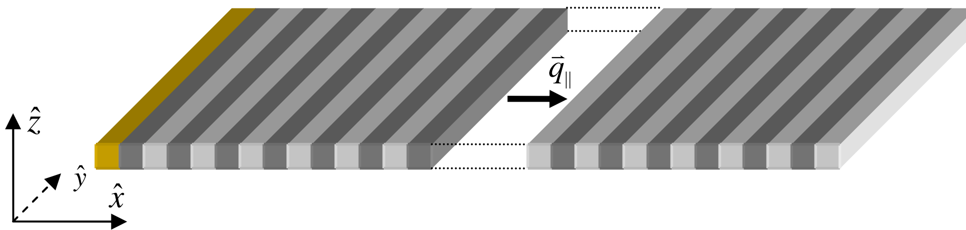

Figure 6-3: Representation of a magnetic thin film as a one-dimensional array of elongated rectangular cells. In this geometry, spin wave propagation is assumed to be in the $\hat{x}$–direction.

The time step used in the simulations should remain sufficiently small for the integration of the dynamic equation by OOMMF to remain stable. The time step can either be determined automatically by OOMMF, possibly based on user-defined

constraints on energy accuracy and maximal time rate of change of the magnetic moment, or can be fixed through user soft limits, as is done here (2 ps). Note that when the time evolution of a magnetization profile is to be studied, the magnetization states have to be saved to disk in intervals consistent with the Nyquist sampling theorem, to enable time-resolved visualization of spin wave emission that does not suffer from aliasing effects.

As stated in the introduction of this section, in the following simulations spin waves will be produced by the application of a local, harmonically varying field to one or more cells at the left edge of the one-dimensional thin film. The orientation of the excitation field is always perpendicular to the external field (200 mT) that saturates the thin film and its amplitude (0.8 mT) is kept small to avoid non-linear effects in the magnetization dynamics. In fact, the Damon-Eshbach theory assumes a linear regime for its results to be valid. The names and values of the remaining general parameters governing the problem are listed in Table 6-1.

Parameter	**Symbol**	**Value**
Magnetic permeability in vacuum	μ_0	$4\cdot\pi\cdot10^{-7}$ H/m [N/A^2]
Gilbert damping	α	$0.01 < \alpha < 0.5$ [-]
Gilbert gyromagnetic ratio	γ	$-2.211\cdot10^5$ [m/(A·s)]
	γ	-28.0 [GHz/T]
Exchange parameter	A	$13\cdot10^{-12}$ [J/m]
Saturation magnetization	M_s	636.6 10^3 [A/m]
	$\mu_0\cdot M_s$	800 [mT]
External field	H_0	159.2 10^3 [A/m]
	$\mu_0\cdot H_0$	200 [mT]
Excitation frequency	f	$10 < f < 60$ [GHz]
Excitation field	$\mu_0\cdot dH(t)$	$0.8\cdot10^{-3}\cdot\sin(2\cdot\pi\cdot f\, t)$ [T]
Time step	dt	1 [ps]

Table 6-1: Names, symbols and values of the parameters that were used in the OOMMF simulations.

6.2.2. One-Dimensional Thin Film Magnetostatic Modes

The first simulations verify whether the analytical MSBVW and MSSW thin film in-plane field modes described in Section 2.4.2 can be excited in the one-dimensional thin film geometry that is adapted here. Therefore, a 5000x5000x5 nm^3 film is spatially discretized using a mesh of rectangular 20x5000x5 nm^3 cells. The film is saturated through the application of a 200 mT in-plane field applied in the $\hat{x}-$ or $\hat{y}-$ direction, depending on whether the MSBVW or the MSSW mode is to be produced. The film is excited at the left edge over a single 20 nm wide cell through the application of a local field with an amplitude that varies harmonically with time as 0.8

mT·sin(2·π·f·t), with f the excitation frequency in GHz. The excitation frequency is varied in discrete steps between 12 and 40 GHz and the wave vectors of the resulting magnetization waves are determined. Note that, to exclude interference due to back-reflection of spin waves that may reach the right outermost edge, an adaptive damping profile is imposed. After 4000 nm from the left edge, the Gilbert damping value starts to increase linearly from 0.01 (value for permalloy) towards 0.5 (critical damping). The simulation results for the MSSW and MSBVW geometries are presented in Figure 6-4, which also displays the analytical dispersion curves (blue and red lines) that were calculated using the formulas from Section 2.4.2. The procedure is repeated for a 50 nm thick film, which results in the dispersion MSSW and MSBVW curves presented in Figure 6-5.

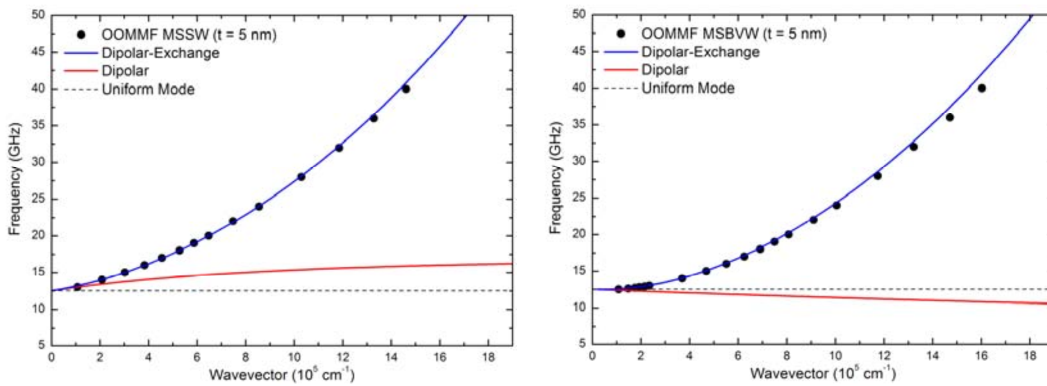

Figure 6-4: MSSW (left) and MSBVW mode (right) simulations (black dots) for a 5x5000x5000 nm^3 one-dimensional thin film. The simulated points fit well with the (blue) dipole-exchange dispersion curves that were calculated according to equations (2-35) and (2-38). For thin films, the dipole contribution (red) is minimal and the modes are largely exchange dominated over the simulated frequency range.

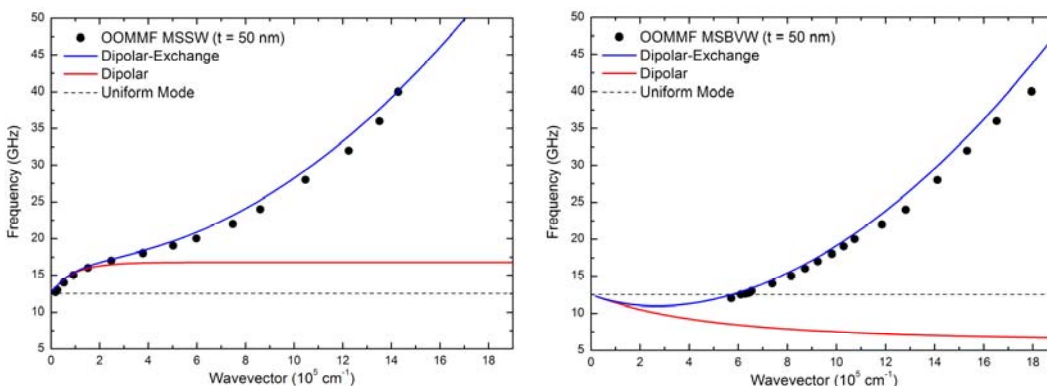

Figure 6-5: MSSW (left) and MSBVW mode (right) simulations (black dots) for a 50x5000x5000 nm^3 one-dimensional thin film. The simulated points agree qualitatively with the (blue) dipole-exchange dispersion curves that were calculated according to equations (2-35) and (2-38). For thicker films, the dipole contribution (red) is more noticeable and the modes carry a combination of dipole and exchange character over the simulated frequency range.

The simulated MSSW and MSBVW mode points (black dots) agree quite well with the dipole-exchange dispersion curves that were calculated based on the theory presented in Section 2.4.2, using equations (2-35) and (2-38) for both the 5 and 50 nm thick film. The red lines indicate the purely dipole dominated case in which no exchange interaction is considered. Note the characteristic negative dispersion in the dipolar regime for the MSBVW mode, as was discussed in the spin wave theory section. The blue lines are the dispersion relations that result when exchange is taken into account (together with the dipolar action). As expected, the dipole-exchange curve fits closely with the dipolar mode for small wave vectors, since the dipolar contribution to the magnetization dynamics is dominant for long wavelengths. This is especially visible for the thicker 50 nm film MSSW mode. At higher frequencies, the modes acquire a more exchange dominated character at the cost of the dipolar contribution (from red to blue). Keeping in mind that the calculated dispersion curves are valid for an infinitely extending thin film, the small offsets of the simulated points may be explained by subtle demagnetization effects related to the bound geometry of the one-dimensional thin film. More likely, however, the error is caused by insufficient resolution of the grid to resolve dynamics with wavelengths shorter than approximately 50 nm, since the offsets seem to increase for wave vectors beyond $10 \cdot 10^5$ cm^{-1}. For the 50 nm thick film, very long wavelength, dipolar MSSW modes are clearly observable down to the uniform mode (FMR) frequency. Apparently, for similar excitation frequencies, the thicker 50 nm film more readily supports a near-uniform ($q = 0$) mode compared to the 5 nm film. This strong uniform mode will also be apparent in the simulations of the power extinction profiles for the 50 nm film, presented in Section 6.2.4, where a long wavelength mode is observed around the FMR frequency. Note that no MSSW mode spin wave propagation is observed below the uniform mode (FMR) frequency of 12.51 GHz, which was calculated using equation (2-36). Although excitation of the first cell at frequencies below the FMR frequency is possible, these excitations are damped out quickly and cannot travel far into the film. Note that due to the increased mode softening for thick films in the MSBVW geometry, spin waves can be excited below the uniform mode frequency.

6.2.3. Spatial Power Decay and Localization Effects

The previous section showed that the simulated modes agree fairly well with those calculated from the extended thin film theory, indicating that the one-dimensional setting can reproduce these modes successfully (at least concerning the dispersion relations). This section explores the spatial decay of the magnetization dynamics resulting from the local excitation of the one-dimensional thin film in the MSSW geometry for varying widths of the excitation area. Several interesting phenomena are observed in the resulting power contour plots, which are shown in Figure 6-6. From top to bottom, the excitation area is expanded over the 1, 2, 4, 8 and 10 first cells at

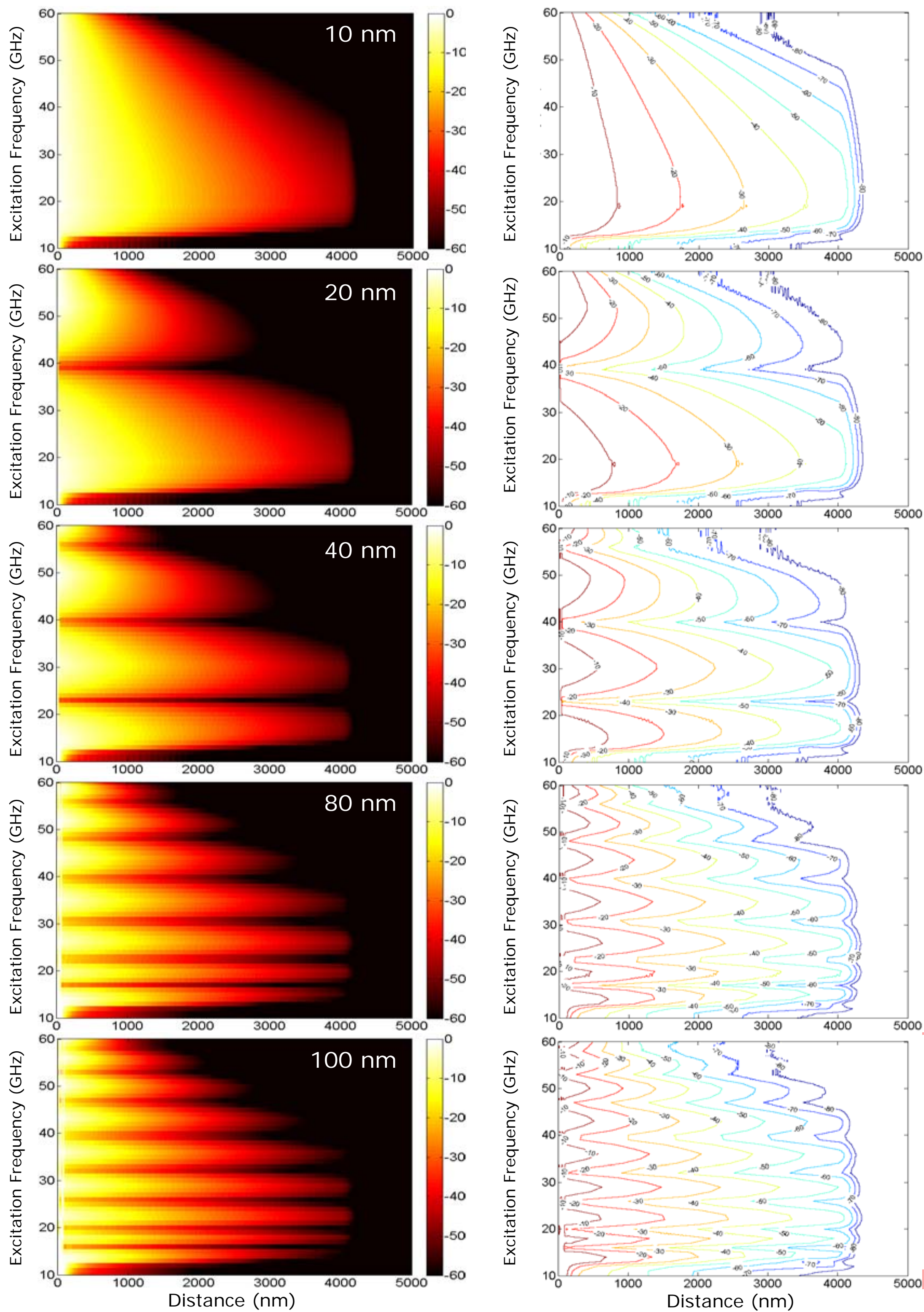

Figure 6-6: Spatial power maps and contour plots as a function of excitation area. From top to bottom, the excitation area is expanded over the 1, 2, 4, 8 and 10 first cells at the left of a 5000x5000x5 nm^3 one-dimensional thin film (10x5000x5 nm^3 mesh). The total excitation area width correspondingly varies from 10, 20, 40, and 80 to 100 nm. The x-axis of every plot indicates the propagation distance of the magnetization excitation with respect to the excitation area (located at x = 0), while the y-axis indicates the imposed excitation frequency.

the left of a 5000x5000x5 nm^3 one-dimensional thin film (10x5000x5 nm^3 mesh). The total excitation area width correspondingly varies from 10, 20, 40, and 80 to 100 nm. The x-axis of every plot indicates the propagation distance of the magnetization excitation with respect to the excitation area (located at x = 0), while the y-axis indicates the imposed excitation frequency, which is varied from 10 to 60 GHz in 1 GHz steps. The left panel shows a logarithmic scale intensity map while the right panel captures the same information in the form of continuous lines that delimit the distance from the excitation area at which the magnetization RMS envelope falls off to a certain amount of its maximum value. The power is in both cases expressed in dB, according to

$$dB(x) = 20 \cdot \log_{10}\left(\frac{\Delta M_z(x)}{\Delta M_{z,\max}}\right). \qquad (6\text{-}1)$$

In this formula, ΔM_z is the local magnetization excitation amplitude in the $\hat{z}-$direction at some distance x from the left edge of the one-dimensional thin film and $\Delta M_{z,max}$ the maximum excitation amplitude obtained over the range of the thin film, which is used to normalize the profiles.

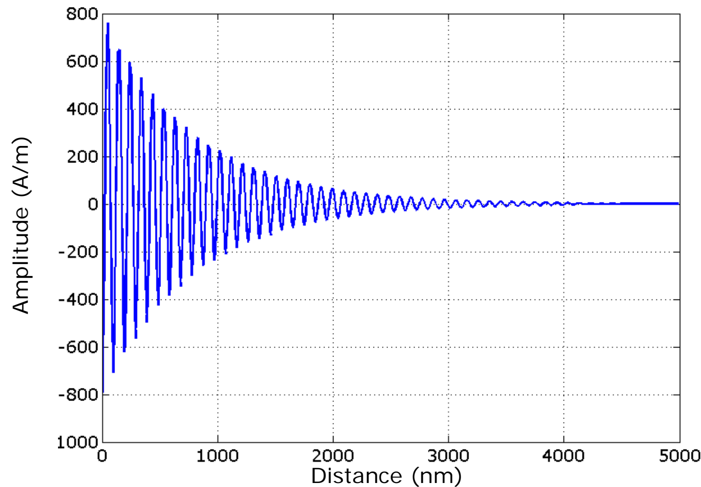

Figure 6-7: Typical spatial decay of a magnetization wave excited at the left of a one-dimensional film with a local 0.8 mT magnetic field. The dynamics in this figure are for a 20 Ghz excitation frequency. An exponential decay of the spin wave amplitude is observed.

First of all, disregarding the spikes that appear for larger excitation areas, the -80 dB level contours for the various excitation area sizes display more or less likewise behavior concerning power radiation into the film, featuring a common penetration depth into the sample as a function of frequency when the spikes are not considered. This indicates that the propagation of the waves into the thin film at large distances is

largely decoupled from the exact size of the excitation area. Note that no long range spin wave propagation is possible below the FMR frequency, just as was observed in the previous simulations of the MSSW dispersion curves. The only mode that could possibly exist below the uniform FMR frequency would be the MSBVW mode, but that would require the field to be applied in another direction (here, the MSSW geometry is simulated). Also note the obvious effect of the linear damping profile that increases the Gilbert damping from 0.01 to 0.5 over the last 1000 nm of the film. At the right side of the film, all magnetization dynamics are effectively damped out. Figure 6-7 depicts the typical amplitude decay of a spin wave resulting from a 20 Ghz excitation. The power decay is observed to follow an exponential scaling with distance away from the excited area. This is also indicated in Figure 6-6 by the equidistantly spaced power contours (right panels) when considering an arbitrary excitation frequency. It is important to note that damping depends on frequency: higher frequency phenomena are damped out more quickly, indicated by the power contour lines lying much closer to each other for higher excitation frequencies. The decay is more readily visible in Figure 6-8, which shows a selection of averaged power profiles over the first 1000 nm for a 80 nm excitation area. The linear decay in the logarithmic plot indicates scaling of the power according to $e^{-\beta x}$ with the scaling factor given by $\beta = m \cdot \ln 10/10$ (the slope m of the decay curve on the logarithmic plot is approximately 5 dB/300 nm = 0.017 nm^{-1} for the 44 GHz excitation, corresponding to a value of β of approximately 0.0038 nm^{-1}. An exponential decay of this kind is typically observed in experimental situations, such as in [53], although the decay rates are slightly different there.

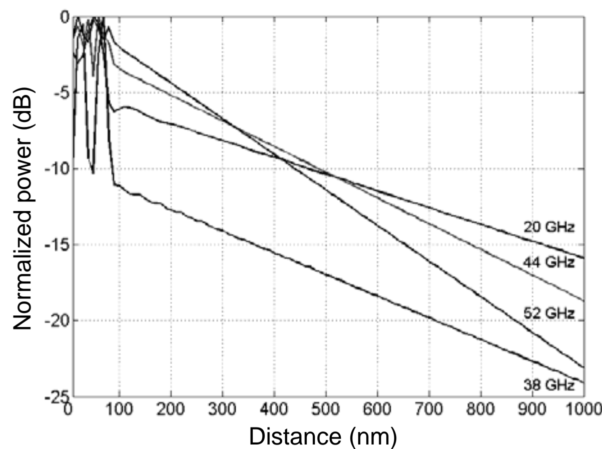

Figure 6-8: The power decay of the magnetization dynamics as a function of distance from the excitation area is quasi-linear on a logarithmic scale, indicating an exponential power decay, which is clearly faster for increasing frequencies.

When the size of the excitation area is increased from 20 to 100 nm, an increasing number of power dissipation spikes becomes visible in the power contour plots of

Figure 6-6. These spikes indicate that, for some particular excitation frequencies, no extended spin waves can propagate into the sample. The fact that the number of spikes grows when the excitation area is increased (no other parameters are altered) suggests that the origin of these spikes is related to an interaction of the generated spin waves with the excitation area. Note that, every time the excitation area is doubled (from 10 to 20, 20 to 40 and 40 to 80 nm), additional spikes occur which complement those that were already present in the previous setting. This kind of behavior is reminiscent of standing wave like phenomena, apart from the fact that in this case the new frequencies entering the dissipation spectrum do not seem to be harmonically related.

The exact origin of these remarkable spikes is explained by looking at the magnetization dynamics within and in the close vicinity of the excitation area. Figure 6-1 displays a set of averaged magnetization power profiles over the first 200 nm of a 5000x5000x5 nm^3 film (2x5000x5 nm^3 mesh, see further) which is excited over an 80 nm wide excitation area. The power profiles corresponding to the adsorption spikes at 17 GHz, 23 GHz, 31 GHz and 44 GHz are indeed observed to form standing wave-like patterns within the excitation area. Note that all of the patterns have an anti-node located exactly at the right edge of the 80 nm excitation area. Correspondingly, at x = 80 nm, the magnetization deviation amplitude is minimized, as is the power emitted into the film, explaining the observed dissipation spikes.

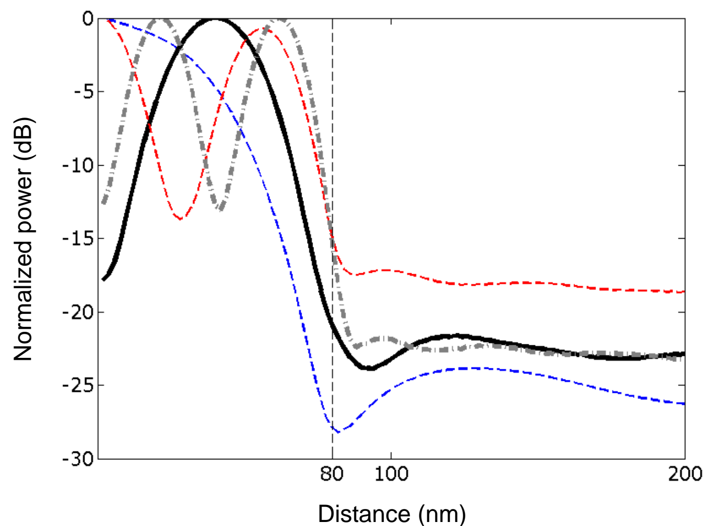

Figure 6-9: Normalized (rms) power profiles as a function of distance from the 80 nm wide excitation area for 17, 23, 31 and 44 GHz excitation frequencies. An integer number of halve wavelengths form a standing wave pattern within the excitation cell. Negligible power is emitted into the thin film for these frequencies, which explains the adsorption spikes observed before. The power profiles are normalized using the maximum magnetization amplitude.

In fact, this effect is also observable in the experimental results presented in FIG.6 of [53], repeated here as Figure 6-10, where magnetostatic mode excitation using a

localized field and spin wave relaxation in permalloy films is studied using scanning Kerr imaging. These experimental results display great analogy with the results produced by the simulations, with an observed exponential decay of the magnetostatic mode, although the geometrical effect of the excitation methodology (RF excitation with a narrow 3 μm stripline) on the emission power profiles apparently went unnoticed there.

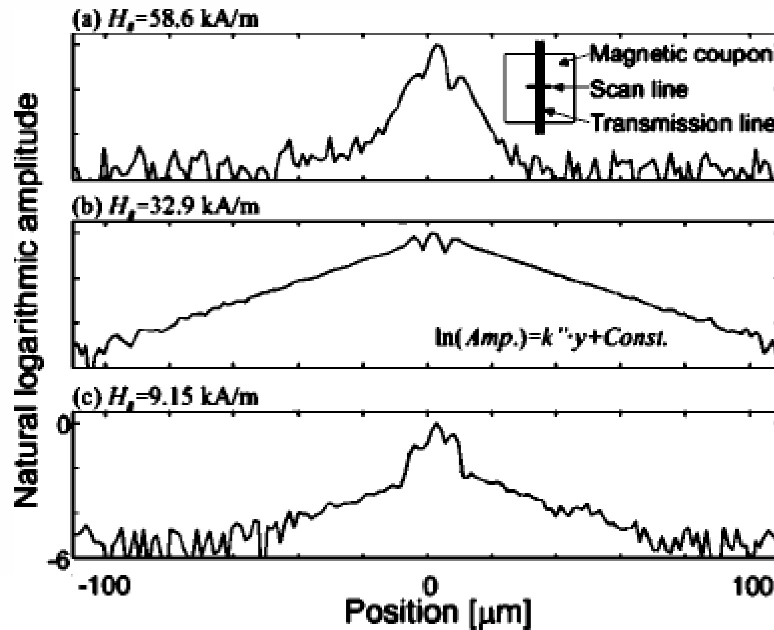

Figure 6-10: Magnetostatic mode excitation with a localized field generated from an RF strip line above an extended 1x1 mm^2 permalloy thin film element by Tamaru et al. Figure taken from [53]. The excitation frequency is fixed to 8.0 GHz for three different bias fields. Exponential decay of the power emission can be observed, along with a clear localization effect around the strip line center in (c).

The link of the observed power spikes with experimental results hereby seems to be established, which indicates the physical relevance of the simulated phenomena. From a technological point of view, the observations made above put forward an additional consideration concerning the optimization of RF power emission from a single nano-oscillator: tuning the oscillator near a spike frequency will inhibit excessive power loss by radiation of spin waves into the common magnetic layer, at least in one direction. Moreover, by tuning a one-dimensional array of oscillators in a two-dimensional layer to a spike frequency, emission of MSSW mode waves could be (partially) suppressed, while coupling is still possible when the oscillators are arranged in the MSBVW direction, leading to more efficient coupling with less power loss in the passive part of the common magnetic layer. As will be seen in a following section, unidirectional, ‘dipole’ like emission is indeed partly discovered in the 2D simulations near frequencies for which an MSSW dissipation spike is expected.

Now the origin of the spikes has become clear, i.e. they are introduced through the formation of a standing wave pattern in the excitation area so that negligible power is emitted into the film, the occurrence of these standing waves is investigated in more detail. For an 80 nm wide excitation area, power dissipation spikes are observed at 17, 23, 31, 40, 48, 56 and 60 GHz. First, the important question is addressed why the spike frequencies are not harmonically related, as would be expected for a standard standing wave pattern. This is obviously caused by the dispersive nature of the magnetostatic modes, due to which wavelength and frequency are no longer linearly related. The frequencies for which an integer number of half wavelengths fits into the 80 nm wide excitation area are now calculated. The frequencies can be found by combining the MSSW dispersion relation with the standing wave condition for the wavelength λ_n as

$$n\frac{\lambda_n}{2} = 80nm \Leftrightarrow \lambda_n = \frac{160}{n}nm. \tag{6-2}$$

Here, n is the integer number (n = 0, 1, 2, 3 …) of halve wavelengths fitting into the 80 nm excitation area. The obtained wavelengths are associated with wave vectors

$$q_n = \frac{2\pi}{\lambda_n} = n \cdot \frac{2\pi}{160}nm^{-1}. \tag{6-3}$$

The frequencies associated with these wave vectors are calculated using the MSSW mode dispersion relation (2-38) for a 5 nm thick film. The results are displayed in Table 6-2. The last two columns indicate whether the calculated frequency spikes are observed for a 5000x5000x5 nm^3 thin film that is excited over an 80 nm wide area for both a coarse 10x5000x5 and a denser 2x5000x5 grid (see further).

n	λ_n (nm)	$\lambda_n/2$ (nm)	q (nm^{-1})	q (10^5 cm^{-1})	$f_{MSSW}(q)$ (GHz)	10 nm	2 nm
1	160	80	0,03927	3,926991	16,1279582	•	•
2	80	40	0,07854	7,853982	22,63247876	•	•
3	53,33	26,67	0,11781	11,78097	32,08778911	•	•
4	40	20	0,15708	15,70796	44,74313899	-	•
5	32	16	0,19635	19,63495	60,76673375	•	•

Table 6-2: Mode numbers n with corresponding wavelengths, halve wavelengths, wave vectors in nm^{-1} and $10^5 \cdot$cm^{-1}, MSSW frequency and occurrence in the simulations of a 5000x5000x5 nm^3 thin film that is excited over a 80 nm wide area for both a coarse 10x5000x5 and denser 2x5000x5 grid (see further).

Observed peaks at 17, 23, 31 and 61 GHz. Apparently, the 17 (n = 1), 23 (n = 2), 31 (n = 3) and 61 (n = 5) GHz frequency spikes in Figure 6-6 are recovered by the

approach described above. However, this reasoning does not explain the peaks at 40, 48 and 56 GHz, while the peak that was expected at 44.74 GHz is clearly not present.

Observed peak at 40 GHz. A peculiar observation considering the 40 GHz peak is that it occurs in any of the 10 nm, 20 nm, 40 nm, 80 nm and 100 nm cases, which suggests its presence is an artifact of the simulation setup. This will also be confirmed in a next simulation that uses a denser grid of 2 nm wide cells instead of the 10 nm wide cells used here.

Observed peaks at 48 and 56 GHz. The 56 Ghz peak is visible for the 40 nm and 80 nm excitation area case and shifts down a little bit to 53 GHz in the 100 nm case, indicating that its presence is associated with the size of the excitation area. Note that according to the approach outlined above, the excitation of a 50 nm area would produce spikes at 57 GHz, a 70 nm area at 37 and 53 GHz and a 90 nm area at 38 and 52 GHz. Seemingly, the 80 nm area can sustain the 57 GHz mode, while the 100 nm area indicates the presence of both the 53 and 57 GHz mode (the 57 GHz is also an even 100 nm mode). At this moment, only the presence of the spike at 48 GHz remains unresolved.

Absent peak at 44.74 GHz. The wavelength associated with this even order (n=4) frequency is exactly 40 nm, and the halve wavelength exactly 20 nm. When looking at the power profiles for this frequency, the 10 nm mesh seems to have trouble accommodating this frequency, due to the half wavelength becoming increasingly small. In a following simulation, this peak will be considered further for an increased mesh resolution. To gain a better understanding of the supposed artifact at 40 GHz and the absent 44.74 GHz mode, the simulation was repeated with a denser grid of 2 nm wide cells (instead of 10 nm) and a finer frequency stepping of 0.5 GHz. The resulting power maps and contour plots are presented in Figure 6-11.

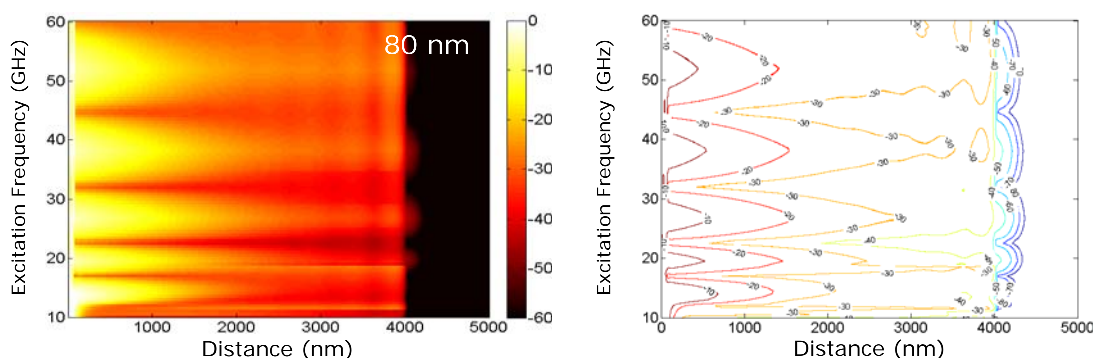

Figure 6-11: Power contour plot as a function of excitation frequency ranging from 10 to 60 GHz for a one-dimensional 5000x5000x5 nm^3 thin film (2x5000x5 nm^3 mesh). The locally applied field varies harmonically over an 80 nm wide excited area at the left of the one-dimensional film. The frequency stepping resolution is increased to 0.5 GHz, compared to 1 GHz in the previous simulations.

The absence of the formerly discussed spike at 40 GHz is immediately obvious in the 2 nm grid simulation. This peak is therefore thought to be associated with a simulation artifact. Note that the previously unobserved 44 GHz mode has also appeared now and that the (unexpected) 56 GHz mode is no longer visible. The presence of the various modes can be visualized by zooming in on the first 200 nm of the film, as shown in Figure 6-12. An increasing number of nodes can be observed for increasing frequency as discussed above.

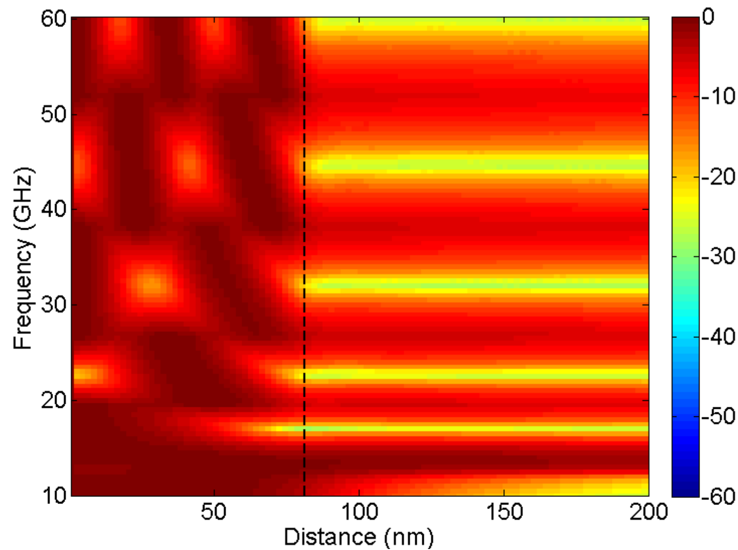

Figure 6-12: Detail of the power profiles as a function of frequency over the first 200 nm of the 5000x5000x5 nm^3 film, simulated with a 2x5000x5 nm^3 mesh. At every frequency where a number of nodes exactly matches the excitation area width (denoted by the dashed line), a power dissipation spike occurs, and the emission of magnetization waves into the thin film is minimized.

6.2.4. Film Thickness

In the following simulations, the effect of increasing the film thickness on the observed power emission profiles is studied. Therefore, a one dimensional 5000x5000xT nm^3 film with variable thickness T is excited as in the previous simulations over an excitation area of 20 nm, corresponding to two 10 nm excitation cells of the 10x5000xT nm^3 grid. The film thickness T is varied between 5, 10 and 50 nm. The resulting power contours as a function of frequency are displayed in Figure 6-13.

The main feature observed in these simulations is that a thicker film (50 nm) displays generally the same power profile behavior as the 5 nm or 10 nm film, except for a much more powerful uniform mode that is apparent as the obvious spike around the uniform mode frequency (12.51 GHz). This effect was also apparent in Figure 6-5, where a long range (small wave vector) mode was observed near the uniform mode

frequency. The dipolar contribution, which is stronger for long wavelength waves, is amplified by the increased dipole moment per unit area due to the increased film thickness, which makes that the long wavelength magnetostatic waves can travel far into the film. This means that making the free spin valve layer thicker will enable the observation of these modes relatively far away from the point contact. An observed peculiarity is the appearance of a dissipation spike at 17 GHz for the 50 nm film. It is at present unclear why this spike develops here, since the halve wavelength associated with the 17 GHz frequency is 80 nm.

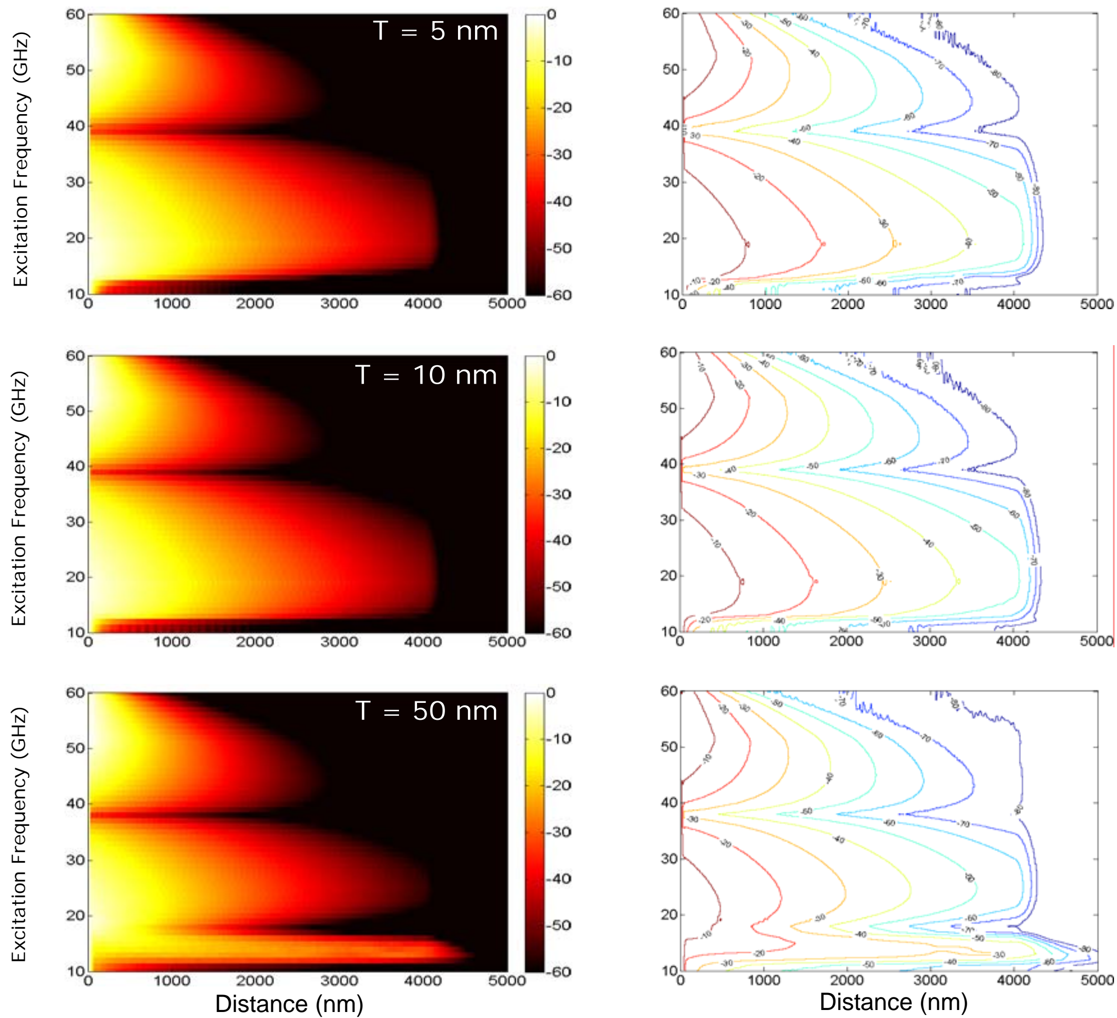

Figure 6-13: Spatial power profiles as a function of excitation frequency for variable thickness 5000x5000xT nm^3 film (T = 5, 10 and 50 nm) with a 10x5000xT mm^3 mesh and a 20 nm wide excitation area. The 50 nm film displays a strong near-uniform mode.

6.3. Two-Dimensional Simulations

The one-dimensional simulations of the previous section revealed some interesting observations, such as the existence of power dissipation spikes whose frequencies of occurrence were related to the geometry of the excitation area. Although the physical

relevance of this phenomenon is thought to be established through the experimental observations in [53], the validity of the one-dimensional simulations as a tool to predict the aforementioned phenomena should be further investigated through non-reduced simulations. Therefore, a limited amount of two-dimensional simulations have been performed to verify the results obtained in the one-dimensional case. The two-dimensional simulation methodology is largely identical to that of the one-dimensional case with respect to field geometries and excitation parameters. Magnetization dynamics are now simulated through the application of a localized 5 mT magnetic field in a 10000x10000x5 nm^3 film discretized using 10x10x5 nm^3 cells. In the following simulations, a circular damping profile is imposed on the simulated geometry as shown in Figure 6-14-a: after 4000 nm from the center, the damping increases linearly from 0.01 to 0.5.

For a comparable mesh definition, the most interesting phenomena in the one-dimensional case were observed for excitation areas of 20 nm and larger (the number of dissipation spikes increased with excitation area size). Therefore, it was decided to simulate a square 80x80x5 nm^3 point contact, consisting of sixty four 10x10x5 nm^3 grid cells arranged in a 8x8 array. A complete stepping of the frequency was virtually impossible due to time constraints, so dynamics were only simulated for excitations at 12.6, 13, 14, 15, 16, 18, 20, 24, 28, 32, 36 and 40 Ghz.

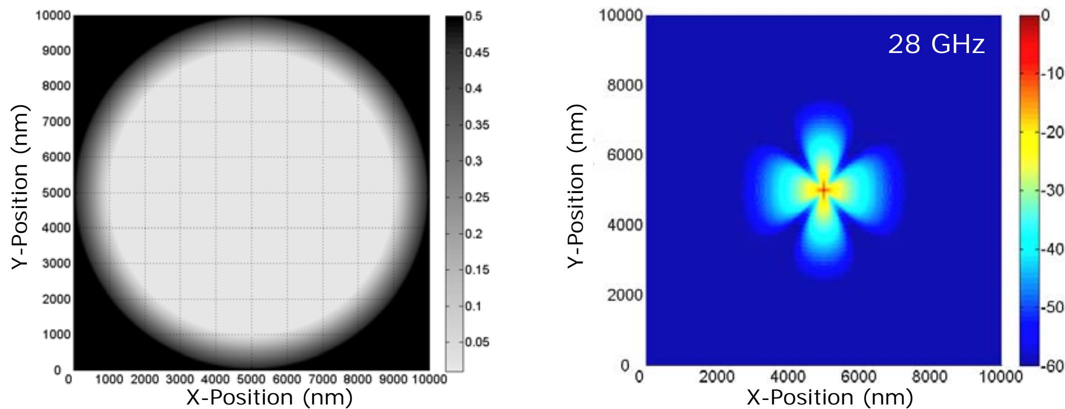

Figure 6-14: (Left) A circular damping profile is imposed in the two-dimensional simulations. Within a 4000 nm radius from the center, the Gilbert damping value is set to 0.01. Over the next 1000 nm the damping increases linearly towards 0.5. Outside the 5000 nm disc, the damping is also set to 0.5. (Right) Directional radiation power pattern of a 80x80x5 nm^3 point contact excited at 28 GHz with a 5 mT local field. The color scale expresses normalized power in dB.

Considering the power decay, the 80x80x5 nm^3 excitation area simulation is compared with the one-dimensional simulation for a 80 nm wide excitation area. For 40 GHz, the one-dimensional decay rate is -30 dB/2000 nm = -0.015 nm^{-1}, while for the two-dimensional simulation, a decay rate of -40 dB/2000 nm = -0.02 nm^{-1} is recorded. For this particular frequency, the decay is thus greater than in the one-

dimensional case, as is expected due to the possibility for the waves to expand and lose energy in all in-plane directions. However, a systematical study of the power decay is difficult, due to the directional power radiation patterns observed for the simulations, as can be seen for a 28 GHz excitation in Figure 6-14-b (and also Figure 6-18).

Next, the relation of the excited wave vectors with those of the one-dimensional case is investigated. This will only be done for the discrete set of frequencies mentioned before. Figure 6-15 displays some typical magnetization amplitude maps (z-component). By taking the two-dimensional spatial fast fourier transform of the amplitude map, the spatial wave vector spectrum is obtained, see Figure 6-16, which delivers the magnetization dynamics wave vectors for all in-plane directions of propagation. Note that, apart from the wave vector contour (dark line), the wave vector spectrum displays a number of features that are not directly related to the magnetization dynamics. For example, the bound geometry of the simulation problem (both the square thin film boundary and the square excitation area) as well as the circular damping profile may give rise artifacts such as the observed two-dimensional sine cardinal functions, which in principle could be filtered out. On the other hand, a high amplitude sine cardinal function may indicate a higher degree of localization of the magnetization dynamics in the square excitation area.

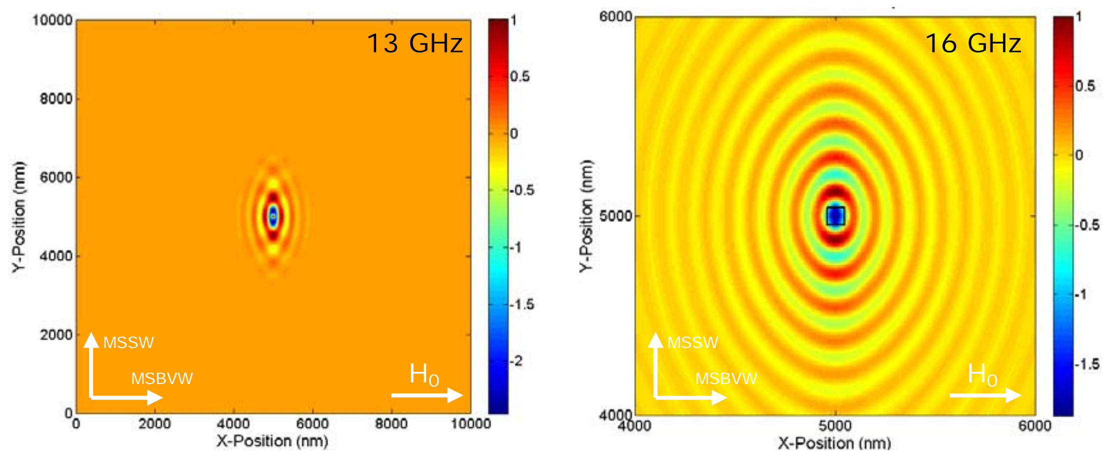

Figure 6-15: Spatial spin wave amplitude (normalized z-component) for the 13 and 16 GHz frequencies for an 80x80 nm^2 excitation area at the center of a two-dimensional film. The wavelength differences in the directions of the MSBVW (x-direction) and MSSW modes (y-direction) leads to an anisotropic wave vector distribution in the spatial fourier transforms presented in Figure 6-16.

From Figure 6-16, the wave vectors of the pure MSSW and MSBVW modes can be deduced from the intersections of the wave vector contour (dark line) with the y- and x-axis. The difference between vertical (MSSW) and horizontal (MSBVW) wave vectors is apparent, with the MSSW wave vector being the smallest one

(corresponding to the largest wavelength in the MSBVW direction in Figure 6-15). The obtained wave vectors are compared with the results of the one-dimensional simulations in Figure 6-17 (red squares). Although they qualitatively agree, the resulting dispersion relation seems to be slightly different from both the analytical solution and the simulation results of the previous section, most notably for the large wave vector region where the dispersion curve is dominated by exchange interactions. Since in both cases, the dispersion curves are lowered, it is suspected that the exchange interaction is not fully captured for wave vectors due to the mesh resolution capabilities being exceeded, which was also discussed as the cause for the dispersion curve offsets in the one-dimensional case.

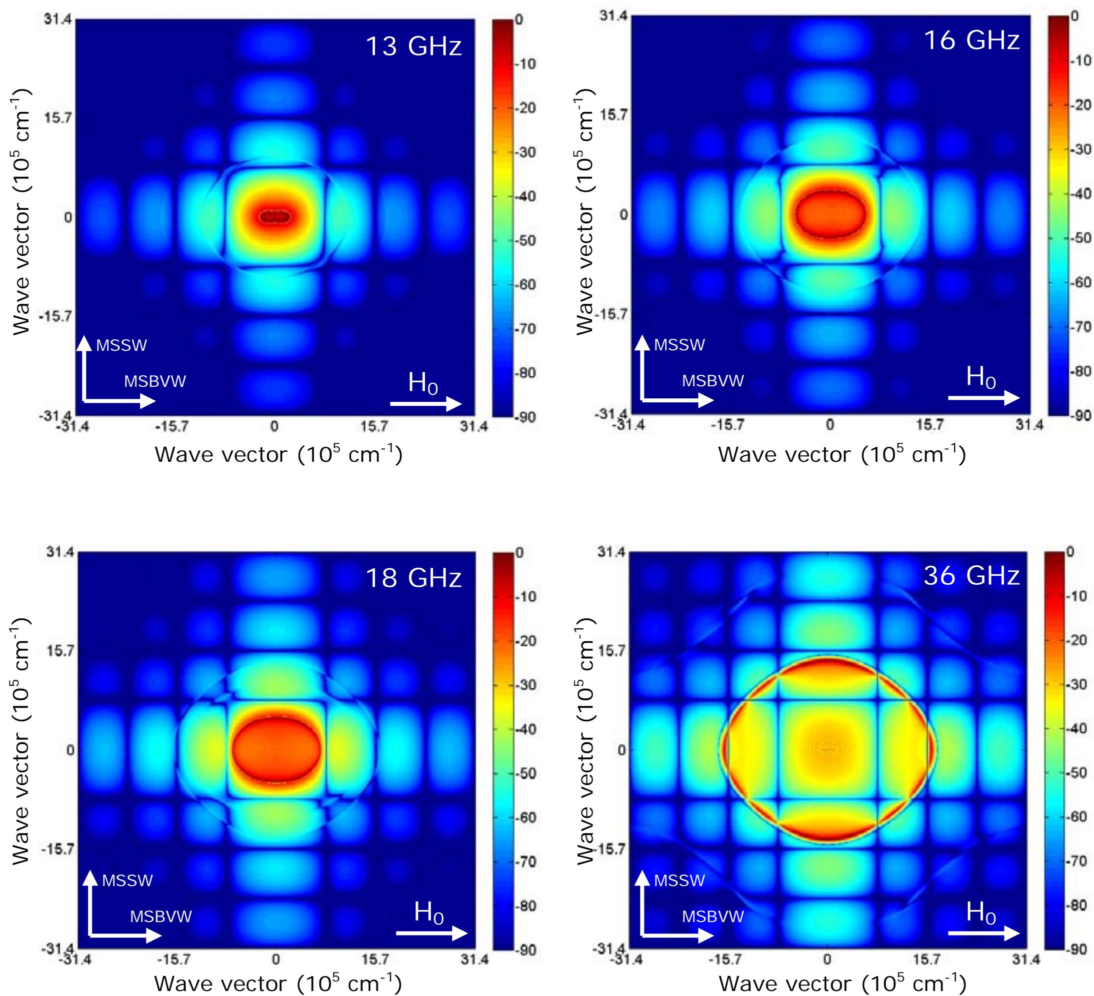

Figure 6-16: Two-dimensional spatial power spectra for the magnetization dynamics resulting from the 13, 16, 18 and 36 GHz excitation of a 80x80 nm^2 area at the center of a two-dimensional film. Apart from the artifacts discussed in the text, anisotropic wave vector contours are visible as dark red ovals, which grow with excitation frequency.

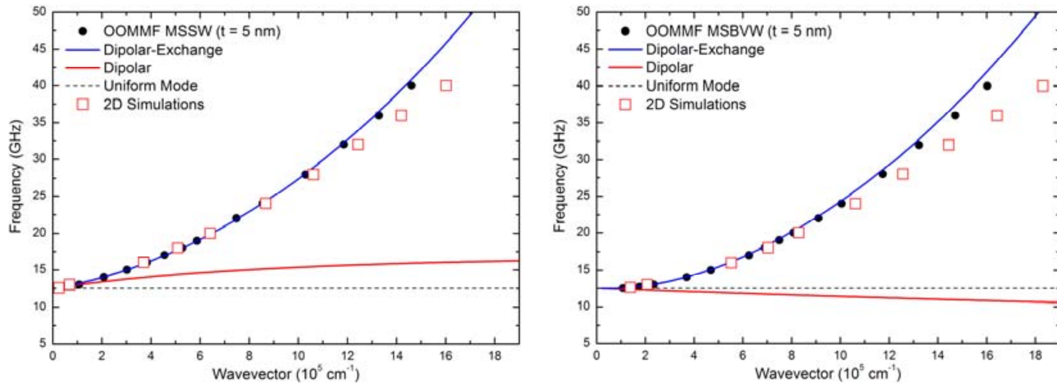

Figure 6-17: Comparison of the wave vectors obtained from the two-dimensional simulations (red squares) with those of the one-dimensional case (black dots). As in the one-dimensional case, the offsets from the calculated dispersion curves are thought to be due to insufficient mesh resolution to resolve short wavelength dynamics.

Consider the two-dimensional power radiation profiles for the various excitation frequencies in Figure 6-18, where the external field (indicated by H_0) is applied along the horizontal x-axis. A few interesting features can be observed in the power emission behavior. For example, for frequencies just above the uniform mode frequency (12.6 and 13 GHz), long wavelength magnetization ripples are observed in the x-direction, which seem to disappear for higher frequencies. The shown spatial (rms) power maps were averaged over only sixteen instantaneous magnetization states, which may have induced the observed ripple. Secondly, an interesting feature develops between the 16 GHz and 18 GHz frequency power maps. Especially in the 18 GHz case, a clear directionality in the power emission is observed along the y-direction. This directionality is also noted for the 36 GHz excitation. This observation can directly be linked to the results of the one-dimensional simulations, which showed reduced power emission for one of the pure MSSW or MSBVW modes when the frequency was chosen appropriately to produce a standing wave pattern in the excited area. Apparently, due to the dispersive nature of the dynamics, a square two-dimensional geometry allows one of the two modes to be actively suppressed, so that power is mainly emitted in the other discrete direction. This is a very important statement, since it seems that, through this effect, unidirectional emission from a point source may be attained.

From the wave vector spectra for these frequencies, the wavelengths of the magnetization dynamics associated with the 18 and 36 GHz excitations are calculated as 90 nm and 38.3 nm, which very nearly match the n = 1 and n = 4 MSVBW modes that enable a standing wave pattern in the 80x80 nm^2 excitation area. The exact frequencies for which the standing wave pattern would perfectly fit the excitation area are estimated from Figure 6-17 as 19.4 and 34.7 Ghz, which are again close to the

frequencies considered above. At the time that the two-dimensional simulations were started, the appearance of the dissipation spikes in the one-dimensional setting was not yet observed. For example, 19.4 and 34.7 GHz frequency two-dimensional simulation should be performed to give a more obvious proof of the existence of MSBVW mode suppression.

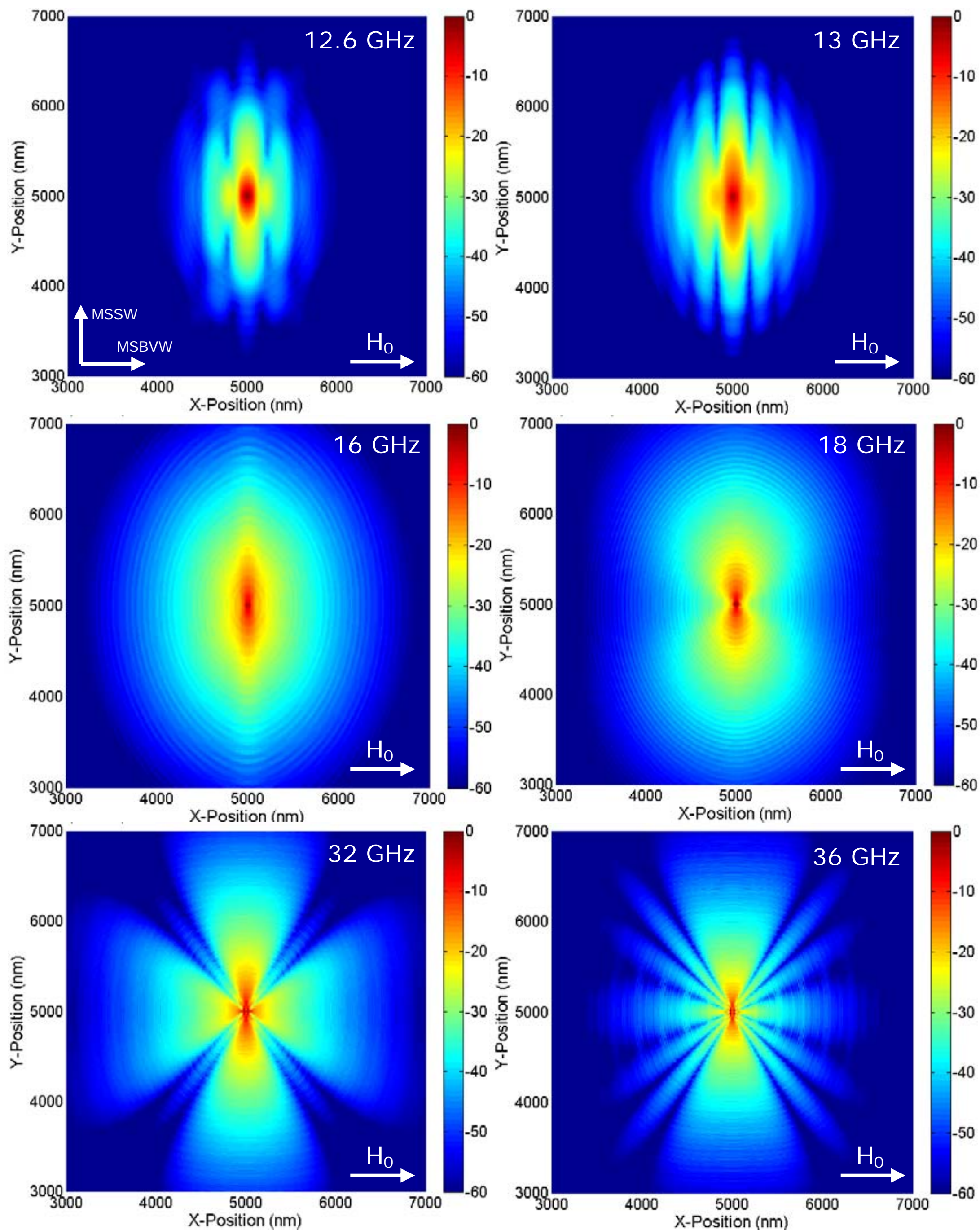

Figure 6-18: Two-dimensional power radiation profiles for various excitation frequencies. The external saturation field is applied in the horizontal x–direction.

Finally, for higher frequencies (32 GHz and 36 Ghz) the radiation maps become more complicated, with radiation concentration in various directions, likely caused by interference effects. Notably, besides the main lobes, the 36 GHz, n = 4 emission also displays the characteristic additional lines observed in [54]. Continued simulations should also consider a circular excitation area, since this may lift the observed anisotropy in the power radiation maps, which may be strongly linked to the use of a square excitation area.

6.4. Conclusions

The results of both one- and two-dimensional simulations of spin wave emission from the application of a harmonically varying, localized magnetic field were presented in the previous sections. After validation by comparison with analytical magnetostatic mode theory, the one-dimensional simulations revealed some interesting observations, such as the existence of power dissipation spikes whose frequencies of occurrence were related to the geometry of the excitation area. By combining the dispersive nature of the spin wave emission with a standing wave argument, the frequencies of occurrence of the dissipation spikes could be predicted successfully. Also, the physical relevance of the phenomenon is thought to be established through the observation of very similar effects in experimental studies of spin wave excitation in thin permalloy elements. The technological relevance for application of the effect in devices through the directional coupling of spin wave energy was discussed. Additionally, the one-dimensional simulations revealed that the spin waves can propagate far into a thin film for excitation frequencies near the uniform mode frequency, especially when the film thickness is increased. Therefore, for spin torque devices that can be made to oscillate near their uniform mode frequency, coupling of multiple oscillators through magnetostatic spin wave emission will be most effective for larger thickness of the free magnetic layer. Of course, this effect is counterbalanced by the inverse scaling of the spin torque effect with film thickness. Following the one-dimensional simulations, two-dimensional simulations were performed to further verify the observations made in the one-dimensional case. A slightly higher decay rate was observed in the two-dimensional case, due to the fact that spin waves can now radiate and lose power in all in-plane directions. The dispersion of the modes in the two-dimensional simulations agrees qualitatively with that of the one-dimensional case for small wave vectors, but deviates for larger wave vectors. Both for the one- and two-dimensional simulations, the offsets from the analytically calculated dispersion curves are thought to be due to insufficient resolution of the applied meshing to successfully resolve the short wavelength dynamics for wave vectors beyond $10 \cdot 10^5$ cm^{-1}. In continued simulations, the effect of spin torque on the induced oscillation should be investigated, including the Oersted

contribution to the effective field resulting from the current distribution, since the propagation behavior may be altered.

7. Conclusions and Outlook

7.1. Conclusions

This work succeeded in the development of a process workflow for the fabrication of magnetic point contact nano-oscillators, featuring optical access to the magnetic layer in the close vicinity of the point contact. The mask design and fabrication process optimization for the simultaneous realization of four different device structures that enable consistent point contact nano-oscillator characterization using both electrical and optical techniques required a substantial amount of effort and time.

The observed anomalous behavior of point contact resistance and magnetoresistance figures as a function of point contact size was considered. Supported by finite element simulations, this behavior was explained by the presence of intricate current distributions in the device electrodes that lead to the observation of a parasitic, partly magnetoresistive series resistance. Based on these observations, a model was constructed that provides a close fit with experimental data, considering both CIP and CPP contributions to the magnetoresistance. Moreover, the physical values of the CIP and CPP magnetoresistance values associated with the electrode and intrinsic point contact resistances could be estimated. Concerning the device optimization process, the observations also provided some guidelines to improve device performance and measurement accuracy, among which the most important is the further downscaling of the point contact size through improvement of the lithographic definition and etching process.

A similar conclusion follows from the microwave measurements that were performed on the point contact devices. These measurements showed that upon the application of a direct current and out-of-plane fields, low frequency oscillations were preferably induced which are assumed to be due to the gyrotropic motion of a vortex core under the point contact area. Only further downscaling of the point contact will reduce the Oersted field associated with the direct current which acts as a restoring force for the vortex state and enable the observation of high frequency dynamics. Furthermore, the downscaling of point contact size in both cases also reduces the current necessary to obtain the required high current density which facilitates the observation of spin torque oscillations.

One of the primary goals of this thesis was to provide point contact nano-oscillator devices featuring optical access to the extended magnetic layer around the active point contact area, enabling the study of spin wave emission with the optical Brillouin light scattering technique, which uses a focused laser spot to probe the free magnetic layer

around the point contact. It has been shown that these devices have been successfully fabricated and that spin wave emission was indeed observed in a limited number of BLS experiments so far. Although further device optimization is required to enable the study of direct current spin torque induced spin wave emission, the observation of RF excited spin waves in the vicinity of the point contact revealed a number of interesting phenomena, some of which require substantial further analysis to enable definitive conclusions. However, the direct observation of spin wave emission around a point contact does indicate the feasibility of these spin waves as a coupling mechanism for nano-oscillator synchronization.

Finally, micro-magnetic simulations were performed to gain more insight into the magnetization dynamics associated with spin wave emission in a common magnetic layer. The dispersion relations of the magnetostatic modes for an in-plane field were successfully simulated in a reduced one-dimensional simulation geometry. It was also shown that the interplay between the point contact size and the magnetostatic modes can generate strong localization of the dynamics inside the point contact area, with minimal emission into the extended thin film. This is explained by the formation of standing wave patterns in the point contact area, for specific frequencies which are not harmonically related due to the dispersive nature of the magnetostatic modes. Moreover, since thicker films were observed to facilitate the long range propagation of magnetostatic modes, increasing the free layer film thickness in fabricated devices may relax the dimension constraints on the BLS tips. Comparison of the one-dimensional simulations with a more realistic two-dimensional setting revealed good wave vector matching with the one-dimensional and analytical case for small to intermediate wave vectors. This indicates the validity of the one-dimensional simplification in this range, at least concerning the obtained wave vectors. Similar to the one-dimensional case, mode localization can occur in a square point contact in the two-dimensional case. However, due to the different dispersion relations for the modes that propagate along and perpendicularly to the external in-plane field, the associated frequencies leading to confinement differ for these modes. Consequently, confinement generally occurs in only one direction and the spatial spin wave radiation pattern becomes largely anisotropic. Interestingly, the direction of radiation inside the device may be tuned by an externally applied field and the frequency of excitation of an RF source. An interesting experiment would be to verify this behavior in square elements. Additionally, anisotropic power emission may have applications in the minimization of power losses in one-dimensional arrays of coupled, phase-synchronized oscillators.

7.2. Outlook

Although this work has provided spin torque nano-oscillator devices which have been shown to meet the compatibility requirement with optical BLS measurements, the generation of direct spin current induced high frequency dynamics could not yet be obtained. However, some important conclusions can be drawn from the measurements that address the further optimization of the device fabrication process. Therefore, further device optimization is mainly concerned with the downscaling of the present point contact sizes. Not only will this help in avoiding the low frequency vortex mode oscillations in favor of high frequency dynamics, it will also improve current confinement and thus reduce the absolute current required to induce these high frequency dynamics, while at the same relaxing any further design constraints on the BLS tips. In order to obtain smaller point contact sizes, either the current BHF wet etching method should be re(de)fined, e.g. through the use of a thinner resist layer, or alternative definition and etching methods should be considered, which use different resist systems or even completely different etching methods, such as chemically assisted plasma etching. Furthermore, because the BLS tips seem to break down for relatively low currents, the next design iteration could consider making these tips considerably wider. However, much information is contained in the rich magnetization dynamics very close to the point contact, so the downscaling of the point contact itself rather than upscaling the tips seems favorable if the possibility of probing the magnetization dynamics in the close vicinity of the point contact is to be retained. It is hoped that after these further optimizations, high frequency dynamics will become accessible in both the RF and BLS experiments and this for reduced currents. As stated in the BLS results section, the generation of spin waves due to an RF AC current (or in the future: a DC spin current) is an extremely complicated process involving many device and measurement setup parameters. For example, the masked roles of the DC generated Oersted field and the spin torque action should be unraveled. These actions should also be fully incorporated in continued simulations which move from the rather artificial local field generation of the magnetization dynamics towards a setting that incorporates the spin torque effect as well as the Oersted field associated with the DC spin current (and maybe, in a later stadium, even temperature). Additionally, these simulations should eventually be quantitatively validated with experiment. In a larger context, it is hoped that further progress will be made towards the complete understanding of the phenomenon of point contact oscillator mode locking through spin wave coupling, which could eventually find applications in novel devices containing arrays of nonlinear coupled point contact spin torque oscillators.

8. Acknowledgements

This thesis would not have been what it is without the continued support of a few particular persons that I would like to direct a special thank you to. First of all, I would like to thank Liesbet Lagae for offering me the chance to participate in the interesting research on spin torque driven magnetic oscillators which is currently an active area in the spintronics group of IMEC. Furthermore, enormous appreciation goes to Maarten van Kampen for his continued support, supervision and advice in gaining insight in both the hands-on experimental intricacies of microstructure fabrication as in the physics associated with magnetic point contact oscillator devices. Maarten, as well as Liesbet and also Wim van Roy have continuously tried to push my thinking and actions a step further and helped me to see the real points of interest in the research of point contact nano-oscillators and spintronics in general. Although these were the persons I had the most interaction with, there are many others that in some way contributed to this work. Generally speaking, I have found the atmosphere at IMEC being one characterized by both strong collegial empathy and a collective feeling for progress. Not a single time a question remained unanswered or someone neglected to give a helping hand, even if not asked for, in the fabrication, characterization and discussion of the results associated with this research. For example, regarding the clean room work, the assistance of Erwin Vandenplas and Stijn De Jonge (training and ellipsometry), helpful tips of Peter Hooylaerts, and e-beam exposures by Jos Moonens (e-beam) were greatly appreciated. Moreover, both inside and outside the clean room, my days were filled with many interesting, sometimes inspiring and often amusing conversations with numerous group members including my office-between-cupboard colleagues Reinier Vanheertum and Pieter Neutens, but also Sven Cornelissen, Koen Weerts, Pol Van Dorpe, Iwijn De Vlaminck, Koen Cox, Koen Vervaeke, Celso Cavaco, Zhen Li, Kristof Lodewijks, Jan Mol, Martin Jouk, Chengxun Liu, Swaroop Ganguly, Willem van de Graaf and some non group members I have learned to know, including Gert Claes, Peter Vicca, Robert Muller, John Viaene, Antoine Pacco and many others who I would like to direct a non-research thank you to. I would also especially like to thank Helmut Schultheiß from the University of Kaiserslautern for his cooperation concerning the optical Brillouin light scattering experiments of which some results were presented in this thesis. Both Helmut and Bert Koopmans helped me to better understand the concept of spin waves in microstructure devices. Last but not least I would like to thank Henk Swagten of the Physics of Nanostructures Group of the Eindhoven University of Technology for his supervision and follow-up of my progress during this thesis. After all, if it was not for him, my interest in spintronics might never even have been triggered. A final thank you goes to my parents, who have been supporting me on many fields throughout the duration of my entire study, including this thesis.

9. References

[1] Thomson, W. 1857. “On the electrodynamic qualities of metals: effects on the electric conductivity of nickel and of iron” *Proc. Roy. Soc. London A* **8**, 546–550.

[2] Baibich, M.N., Broto, J.M., Fert, A., Nguyen Van Dau, F., Petroff, F., Eitenne, P., Creuzet, G., Friederich, A., Chazelas, J. 1988 “Giant Magnetoresistance of (001)Fe/(001)Cr Magnetic Superlattices” *Phys. Rev. Lett.* **61**, 2472–2475.

[3] Binasch, G., Grünberg, P., Saurenbach, F., Zinn, W. 1989. "Enhanced magnetoresistance in layered magnetic structures with antiferromagnetic interlayer exchange" *Phys. Rev. B* **39**, 4828–4830.

[4] Grünberg, P., Schreiber, R., Pang, Y., Brodsky, M.B., Sowers, H. 1986. “Layered Magnetic Structures: Evidence for Antiferromagnetic Coupling of Fe Layers across Cr Interlayers” *Phys. Rev. Lett.* **57**, 2442–2445.

[5] Moodera, J.S., Kinder, L.R., Wong, T.M., Meservey, R. 1995. "Large Magnetoresistance at Room Temperature in Ferromagnetic Thin Film Tunnel Junctions" *Phys. Rev. Lett.* **74**, 3273–3276.

[6] Juliere, M. 1975. “Tunneling between ferromagnetic films” *Phys. Lett.* **54**A, 225.

[7] Slonczewski, J.C. 1996. “Current driven excitation of magnetic multilayers” *Journal of Magnetism and Magnetic Materials* **159**, L1–L7.

[8] Berger, L. 1996. “Emission of spin waves by a magnetic multilayer traversed by a current” *Phys. Rev. B* **54**(13), 9353–9358.

[9] Katine, J.A., Albert, F.J., Buhrman, R.A., Myers, E.B., Ralph, D.C. 2000. “Current-Driven Magnetization Reversal and Spin-Wave Excitations in Co /Cu /Co Pillars” *Phys. Rev. Lett.* **84**(14): 3149–3152.

[10] Myers, E.B., Ralph, D.C., Katine, J.A., Louie, R.N., Buhrman, R.A. 1999. “Current-Induced Switching of Domains in Magnetic Multilayer Devices” *Science* **6**, 867.

[11] Grollier, J., Cros, V., Hamzic, A., George, J., M., Jaffrès, H., Fert, A., Faini, G., Ben Youssef, J., Legall, H. 2001. “Spin-polarized current induced switching in Co/Cu/Co pillars” *Appl. Phys. Lett.* **78**, 3663.

[12] Rippard, W.H., Pufall, M.R., Kaka, S., Russek, S.E., Silva, T.J. 2004. “Direct-Current Induced Dynamics in Co90Fe10/Ni80Fe20 Point Contacts.” *Phys. Rev. Lett.* **92**(2) 027201.

[13] Chen, T.Y., Ji, Y., Chien, C.L. 2004. “Switching by point-contact spin injection in a continuous film” *Appl. Phys. Lett.* **84**(3), pp. 380–382.

[14] Kiselev, S.I., Sankey, J.C., Krivorotov, I.N., Emley, N.C., Schoelkopf, R.J., Buhrman, R.A., Ralph, D.C. 2003. “Microwave oscillations of a nanomagnet driven by a spin-polarized current” *Nature* **425**, 380–383.

[15] Kiselev, S.I., Sankey, J.C., Krivorotov, I.N., Emley, N.C., Rinkoski, M., Perez, C., Buhrman, R.A., Ralph, D.C. 2004. “Current-Induced Nanomagnet Dynamics for Magnetic Fields Perpendicular to the Sample Plane” *Phys. Rev. Lett.* **93**, 036601.

[16] Grollier, J., Cros, V., Fert, A. 2006. “Synchronization of spin-transfer oscillators driven by stimulated microwave currents” *Phys. Rev. B* **73**, 060409.

[17] Mancoff, F.B., Rizzo, N.D., Engel, B.N., Tehrani, S. 2005. “Phase-locking in double-point-contact spin-transfer devices.” *Nature* **437**, 393–395.

[18] Kaka, S., Pufall, M.R., Rippard, W.H., Silva, T.J., Russek, S.E., Katine, J.A. 2005. “Mutual phase-locking of microwave spin torque nano-oscillators” *Nature* **437**, 389–392.

[19] Pufall, M.R., Rippard, W.H., Russek, S.E., Kaka, S., Katine, J.A. 2006. “Electrical Measurement of Spin-Wave Interactions of Proximate Spin Transfer Nanooscillators” *Phys. Rev. Lett.* **97**, 087206.

[20] Demokritov, S.O., Hillebrands, B., Slavin, A.N. 2001. “Brillouin light scattering studies of confined spin waves: linear and nonlinear confinement” *Physics Reports* **348**, 441–489.

[21] Smith, N., Jeffers, F., Freeman, J. 1991. “A high-sensitivity magnetoresistive magnetometer” *J. Appl. Phys.* **69**(8), 5082–5084.

[22] Cullity, B.D. 1972. *Introduction to magnetic materials.* Addison-Wesley Publishing Company.

[23] Hiroto, E., Sakakima, H., Inomata, K. 2002. *Giant Magneto-Resistance Devices.* Springer–Verlag.

[24] Mott, N.H. 1936. *Proc. Roy. Soc. A* **153**(880), 699–717.

[25] Yang, Q., Holody, P., Lee, S.-F., Henry, L.L., Loloee, R., Schroeder, P.A., Pratt, Jr., W.P., Bass, J. 1994. “Spin flip diffusion length and giant magnetoresistance at low temperatures” *Phys. Rev. Lett.* **72**, 3274–3277.

[26] Stiles, M.D., Miltat J. 2006. “Spin transfer torque and dynamics” *Spin Dynamics in Confined Magnetic Structures III.* Springer.

[27] Stiles, M.D., Zangwill, A. 2002. “Anatomy of spin transfer torque”

Physical Review B **66**, 014407.

[28] Tserkovnyak, Y., Brataas, A., Bauer, G.E.W., Halperin, B.I. 2005. "Nonlocal magnetization dynamics in ferromagnetic heterostructures" *Reviews of Modern Physics* **77**(4), 1375–1421.

[29] Berger, L. 2002. "Interaction of electrons with spin waves in the bulk and in multilayers" *J. Appl. Phys.* **91**(10), 6795–6800.

[30] Landau, L.D., Lifshitz, E.M. 1935. "On the theory of the dispersion of magnetic permeability in ferromagnetic bodies" *Physikalische Zeitschrift der Sowjetunion* **8**.

[31] Gilbert, T.L. 2004. "A phenomenological theory of damping in ferromagnetic materials" *IEEE Transactions on Magnetism* **40**, 3443.

[32] Sun, J.Z. 2006. "Spin angular momentum transfer in current-perpendicular nanomagnetic junctions" *IBM Journal of Research and Development* **50**(1).

[33] Kittel, C. 2005. *Introduction to Solid State Physics*, Eight Edition, John Wiley & Sons, Inc.

[34] Bloch, F. 1930. "Zur Theorie des Ferromagnetismus" *Zeitschrift für Physik A* **61**, 206–219.

[35] Hurben, M.R., Patton, C.E. 1995. "Theory of magnetostatic waves for in-plane magnetized isotropic films" *Journal of Magnetism and Magnetic Materials* **139**, 263–291.

[36] Morrish, A.H. 2001. *The Physical Principles of Magnetism* IEEE Press Classic Reissue, 297, eq. (6-6.17).

[37] Damon, R.W., Eshbach, J.R. 1961. *J. Phys. Chem. Solids* **19**, 308.

[38] Demokritov, S.O., Hillebrands, B., Slavin, A.N. 2001. *Phys. Rep.* **348**, 441–489.

[39] Stancil, D. 1993. *Theory of Magnetostatic Waves*, Springer, New York, Berlin, 2nd Edition.

[40] Herring, C., Kittel, C. 1951. "On the Theory of Spin Waves in Ferromagnetic Media" *Phys. Rev.* **81**, 869–880

[41] Kittel, C. 2005. Chapter 13, Magnetic Resonance, equation (43) in *Introduction to Solid State Physics*, Eight Edition, John Wiley & Sons, Inc.

[42] Damon, R.W., Eshbach, J.R. 1961. *J. Phys. Chem. Solids* **19**, 308.

[43] Sandercock, J.R. 1982. "Trends in Brillouin scattering: studies of opaque materials, supported films, and central modes" *Topics in Applied Physics* **5**(1), 173–206.

[44] Giovanni Carlotti and Gianluca Gubbiotti. 1999. “Brillouin scattering and magnetic excitations in layered structures” *La Revista del Nuovo Cimento.*

[45] Schultheiß, H. 2005. “Brillouin-Lichtstreu-Mikroskopie an magnetischen Mikrostrukturen” *Master Thesis.* Kaiserslautern University of Technology.

[46] Williams, Kirt R., Gupta, Kishan and Wasilik, Matthew. 2003. “Etch Rates for Micromachining Processing—Part II” *Journal of Microelectromechanical Systems* **12**(6), 761–778.

[47] Pufall, M.R., Rippard, W.H., Schneider, M.L., Russek, S.E. 2007. “Low-field current-hysteretic oscillations in spin-transfer nanocontacts” *Phys. Rev. B* **75**, 140404.

[48] Guslienko, K. Yu., Ivanov, B.A., Novosad, V., Otani, Y., Shima, H., Fukamichi, K. 2002. “Eigenfrequencies of vortex state excitations in magnetic submicron-size disks” *J. Appl. Phys.* **91**(10), 8037–8039.

[49] Park, J.P., Eames, P., Engebretson, D.M., Berezovsky, J., Crowell, P.A. 2003. “Imaging of spin dynamics in closure domain and vortex structures” *Phys. Rev. B* **67**, 020403.

[50] Novosad,V., Fradin, F.Y., Roy, P.E., Buchanan, K.S., Guslienko, K. Yu., Bader, S.D. 2005. “Magnetic vortex resonance in patterned ferromagnetic dots” *Phys. Rev. B* **72**, 024455.

[51] Kasai, S., Nakatani, Y., Kobayashi, K., Kohno, H.. Ono, T. 2006. “Current-Driven Resonant Excitation of Magnetic Vortices” *Phys. Rev. Lett.* **97**, 107204.

[52] http://math.nist.gov/oommf/

[53] Tamaru, S., Bain, J.A., van de Veerdonk, R.J.M., Crawford, T.M., Covington, M., Kryder, M.H. 2004. “Measurement of magnetostatic mode excitation and relaxation in permalloy films using scanning Kerr imaging” *Phys. Rev. B* **70**, 104416.

[54] Demidov, V.E., Hillebrands, B., Demokritov, S.O., Laufenberg, M., Freitas, Paulo P. 2005. “Two-dimensional patterns of spin-wave radiation by rectangular spin-valve elements” *J. Appl. Phys.* **97**, 10A717.

[55] Choi, S., Kim, S.K., Demidov, V.E., Demokritov, S.O. 2007. “Double-contact spin-torque nano-oscillator with optimized spin-wave coupling: Micromagnetic modeling” *Appl. Phys. Lett.* **90**, 083114.

[56] Berkov, D.V., Gorn, N.L. 2007. “Magnetization oscillations induced by a spin-polarized current in a point-contact geometry: Mode hopping and nonlinear damping effects” *Phys. Rev. B* **76**, 144414.

List of Abbreviations

A	area
AC	alternating current
AFM	atomic force microscopy
AMR	anisotropic magnetoresistance
BHF	buffered hydrofluoric acid
BLS	Brillouin light scattering
BT	bias tee
CIP	current in plane
CMOS	complementary metal–oxide–semiconductor
CPP	current perpendicular to plane
CPW	coplanar waveguide
DC	direct current
DRAM	dynamic random access memory
DUT	device under test
EBL	electron beam lithography
FLASH	non-volatile computer memory technology
FOX	flowable oxide
GMR	giant magnetoresistance
GPIB	general purpose interface bus
IPA	iso-propyl-alcohol
LLG	Landau-Lifshitz-Gilbert
LLGS	Landau-Lifshitz-Gilbert-Slonzcewski
MIBK	methyl isobutyl ketone
MR	magnetoresistance
MRAM	magnetoresistive random access memory
MSBVW	magnetostatic backward volume wave
MSFVW	magnetostatic forward volume wave
MSSW	magnetostatic surface wave
MTJ	magnetic tunnel junction
NIST	National Institute of Standards and Technology
OOMMF	object-oriented micro-magnetic framework
PCS	programmable current source
PMMA	polymethyl methacrylate
Py	Permalloy ($Ni_{80}Fe_{20}$)
R	resistance
ρ	resistivity
RF	radio frequency
RMS	Root-Mean-Square

RxA	resistance times area product
SDRAM	synchronous dynamic random access memory
SEM	scanning electron microscopy
ST	spin torque
SW	spin wave
TMR	tunnel magnetoresistance